Resonant enhancement of magneto-optical effects using 1-D planar micro-structuration

Bobin Varghese

▶ **To cite this version:**

Bobin Varghese. Resonant enhancement of magneto-optical effects using 1-D planar micro-structuration. Optics / Photonic. Université de Lyon, 2017. English. NNT : 2017LYSES057 . tel-02111775

HAL Id: tel-02111775
https://theses.hal.science/tel-02111775

Submitted on 26 Apr 2019

HAL is a multi-disciplinary open access archive for the deposit and dissemination of scientific research documents, whether they are published or not. The documents may come from teaching and research institutions in France or abroad, or from public or private research centers.

L'archive ouverte pluridisciplinaire **HAL**, est destinée au dépôt et à la diffusion de documents scientifiques de niveau recherche, publiés ou non, émanant des établissements d'enseignement et de recherche français ou étrangers, des laboratoires publics ou privés.

N° d'ordre NNT : 2017LYSES057

THÈSE de DOCTORAT DE L'UNIVERSITÉ DE LYON

opérée au sein de

Laboratoire Hubert Curien

Ecole Doctorale ED SIS 488

(**Ecole Doctorale Science, Ingénierie et Santé**)

Spécialité de doctorat: Optique Photonique Hyperfréquence

Discipline: Physique

Soutenue publiquement le 14/12/2017, par

Bobin VARGHESE

Resonant enhancement of Magneto-Optical effects using 1-D planar micro-structuration

---

Devant le jury composé de :

Mme. YAM, Vy Navy	MCF-HDR	Université Paris Sud	Rapporteuse
M. BENYATTOU, Taha	DR CNRS	INL Lyon	Rapporteur
M. BERLING, Dominique	PU	IS2M Mulhouse	Examinateur
M. JOURLIN, Yves	PU	UJM St. Etienne	Examinateur
Mme. GAMET, Emilie	MCF	UJM St. Etienne	Co-encadrante
M. ROYER, François	PU	UJM St. Etienne	Directeur de thèse

CONTENTS

GENERAL INTRODUCTION

Magneto-optics is the study of polarization-dependent interaction of light with matter, either containing an internal magnetization or subject to an external magnetic field. Such magnetic order induces a non-reciprocal coupling between the different components of electromagnetic waves and results as antisymmetric off-diagonal elements in the material's permittivity tensor [1]. This gives rise to first-order Magneto-Optical (MO) effects which have been studied in this work. They include Faraday effect in transmission and polar-, longitudinal-, transverse- Kerr effects in reflection [1] configurations. Over the years, magneto-optics have found varied applications ranging from sensing [2], optical isolation [3] and modulation [4] to even data storage [5].

In order to improve the performance of associated devices, strategies have been led since approximately 20 years. One of the most common approaches is to use a periodic micro-structuration to provide a resonant optical effect which induces an enhancement of the MO effects [6]. As the best performing MO materials are iron garnets and their derivatives which are still challenging to micro- or nano-structure [7], a majority of the articles in literature are theoretical and simulation papers [8–11]. The few experimental achievements generally bypass the structuration of the MO material by using a metallic grating on top of a MO thin film [12].

The aim of this thesis is to demonstrate an experimental enhancement of MO effects using 1-D resonant gratings. This can be achieved as the MO material, deve-

loped in our research team since more than 15 years, can be more easily processed into photonic devices [13, 14]. Indeed, this is a silica composite with embedded NPs of cobalt ferrite, obtained through a soft temperature sol-gel process. The sol-gel route allows filling of the grating slits, leading to MO devices.

The thesis is organized as follows:

Chapter-1 starts with an introduction to magneto-optics in detail with sections on its physical origin and its effect in transmission and reflection configurations. It is followed by sections that describe the physics of guided magneto-optics, resonant structures and surface plasmons. This is important to understand the final section of this chapter which focuses on the works reported in literature regarding a resonant enhancement of magneto-optical effects using different means. According to this bibliographic study, the ways of attaining exaltation in magneto-plasmonic as well as in all-dielectric 1-D structures are identified and will lead to the experimental work and associated results described in chapter 3.

Chapter-2 first presents the methods used in this work to achieve the aims set. Firstly, the characteristics of cobalt ferrites NPs, synthesized in Phenix Laboratory (Paris) by Dr. Sophie Neveu, are presented. Their crystal structure and magnetic properties are discussed as well as the spectral behavior and magnetic field dependence of the resulting Faraday effect. The next section deals with the MO composite elaborated by the sol-gel technique and coated as thin-films using the dip-coating method. Optical properties of this composite and its ability to impregnate templates gives a complement of its properties. The optical and MO measurement setups are then detailed. The focus is on the explanation about the spectral magneto-optical bench that permits to measure polarization rotation until 10^{-3° in the visible and near IR range. Examples of magneto-optic thin-film measurements are then given in transmission or reflection configurations. The chapter ends with some explanation about the simulation tools used to design the devices.

The *final chapter* details the optical and MO responses of MO gratings realized with gold, photoresist, titanium dioxide and silicon nitride. The design of each type of structure is developed. The experimental measures are then compared to the respective simulated curves. The simulation results obtained for the Si_3N_4 based 1-D resonant gratings are more detailed and show the possibility to enhance different MO effects. The associated results are the first experimental demonstration of an enhancement of Faraday effect via an all-dielectric structure. Moreover, en-

hancements of Longitudinal Magneto-Optical Kerr Effect (LMOKE) and Transverse Magneto-Optical Kerr Effect (TMOKE) on the same diffraction grating have been measured, confirming our theoretical work.

CHAPTER

1

MAGNETO-OPTICAL EFFECTS AND ENHANCEMENT PROCESSES

The objective of this chapter is to give the general information required to fix the main issues of this study. As the subject of this work is to use a planar periodic structuration to enhance MO effects, it will be devoted to the physical background of this phenomenon. The first section deals with magneto-optics and the second with resonant structures. In the third section, mechanisms of enhancement of MO effects are reviewed before giving the objectives of this thesis.

1.1 Magneto-Optics: An introduction

The study of MO effects commenced in the 19^{th} century after the discovery of light polarization rotation by glass in a longitudinal magnetic field by M. Faraday in 1845 [15]. It was the first experimental evidence of a coupling between light and magnetism. Since their discovery, they have played an important role in the development of electromagnetism by providing experimental support to the electromagnetic theory and also the quantum theory of spin-orbit coupling [16]. Practically,

they have found applications in sensing [2], optical modulation [4], optical isolation [3] [17], data storage [5] [18] to name a few. Magneto-optical effects can be linear or non-linear in nature. The aim of this section is to give the main features of the various linear magneto optic effects i.e. effects that are characterized by a linear dependence of material properties on the magnetic stimulation.

1.1.1 Physical origin

In nature, there are materials whose constituent atoms/ions do not contain any intrinsic magnetic dipole moments. Such materials are termed as *diamagnetic* materials or diamagnets. On the contrary, there are materials which do have intrinsic magnetic moments, but randomly oriented in thermal equilibrium above a certain characteristic temperature. Such materials are known as *paramagnetic* materials or paramagnets. When such materials are in the presence of an external magnetic field their dipoles orient themselves along the direction of the external field, resulting in a net magnetization of the material. Furthermore, there are certain paramagnets whose intrinsic magnetic moments can become orderly oriented even in the absence of a external magnetic field below a certain critical value. Such materials are called magnetically ordered materials. A magnetically ordered material whose intrinsic magnetic moments all point in the same direction possesses a spontaneous magnetization and is called a *ferromagnetic* material or ferromagnet. Examples include Fe, Co, Ni etc. For materials whose intrinsic moments are magnetically ordered but point in alternate directions in unequal numbers, this results in a net spontaneous magnetization of the material. They are termed as *ferrimagnetic* materials or ferrimagnets. Examples include rare-earth garnets and iron oxides: cobalt ferrite ($CoFe_2O_4$), Fe_3O_4, $\gamma - Fe_2O_3$. If the anti-parallel alignment of the alternating moments completely cancel each other, there is no spontaneous magnetization in the material. Such a material is called an *anti-ferromagnetic* material or antiferromagnet. Examples include Cr, FeO, CoO, NiO [19].

Magneto-Optics is the branch of optics dealing with the interaction of light and matter, either in the presence of an internal magnetization $\mathbf{M}$ in the matter or, an externally applied magnetic field, $\boldsymbol{H_0}$. MO effects can be described by the interaction of incident photons with the electron spins through spin-orbit coupling [20] but, these effects can be completely explained by the classical magnetic properties of the material [19] [21]. For instance, MO effects in an anisotropic material can be

conveniently expressed in terms of its relative dielectric permittivity, ϵ which is a 3x3 tensor as follows:

$$\epsilon = \begin{bmatrix} \epsilon_{xx} & \epsilon_{xy} & \epsilon_{xz} \\ \epsilon_{yx} & \epsilon_{yy} & \epsilon_{yz} \\ \epsilon_{zx} & \epsilon_{zy} & \epsilon_{zz} \end{bmatrix} \tag{1.1}$$

Here, the subscripts x, y, z represent the three Cartesian coordinate axis. For a linear anisotropic material, it is further reduced to just a diagonal tensor as follows:

$$\epsilon = \begin{bmatrix} \epsilon_{xx} & 0 & 0 \\ 0 & \epsilon_{yy} & 0 \\ 0 & 0 & \epsilon_{zz} \end{bmatrix} \tag{1.2}$$

However, in the presence of an internal magnetization $\mathbf{M}$ pointing, for instance, in the z-direction i.e. $\mathbf{M}$=M$\hat{\boldsymbol{z}}$, the off-diagonal elements of the permittivity tensor in the x- and y- direction become coupled. Microscopically, this can be explained using the classical electron theory. When an incident EM field illuminates a material, a Lorentz force acts on the material's electrons and consequently, an oscillation in one direction, tends to create another oscillation in its transverse direction manifesting itself as non-zero off-diagonal elements. The material's permittivity gets modified as:

$$\epsilon = \begin{bmatrix} \epsilon_{xx} & i\epsilon_{MO} & 0 \\ -i\epsilon_{MO} & \epsilon_{yy} & 0 \\ 0 & 0 & \epsilon_{zz} \end{bmatrix} \tag{1.3}$$

where the off-diagonal elements represent the magnetically-induced part and are directly proportional to $\mathbf{M}$. ϵ_{MO} is referred to as the magneto-optical constant of a material. Its value varies from material-to-material and is a function of the incident wavelength i.e.

$$\epsilon_{MO} = \epsilon_{MO}(\lambda, \mathbf{M})$$

The tensor elements of the permittivity tensor are complex in general. For an isotropic material at room temperature, the diagonal elements can be expressed as a square of the complex refractive index of the material i.e.

$$\epsilon_{xx} = \epsilon_{yy} = \epsilon_{zz} = N^2$$

where

$$N = n + ik \tag{1.4}$$

In the above relation, n represents the dispersion and k represents the extinction coefficient of the material. It will be explained in the next section how an internal magnetization makes a medium circularly birefringent resulting in some interesting optical behavior.

1.1.2 Magneto-Optical effects in transmission mode

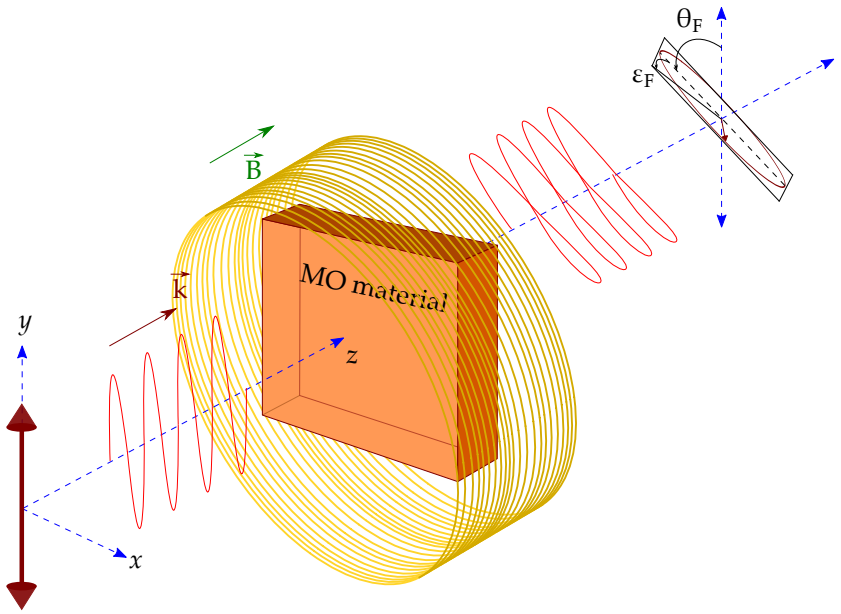

Figure 1.1: Schematic depiction of the magneto-optical (MO) Faraday effect.

Figure 1.1 schematically depicts the MO effect of polarization rotation and polarization ellipticity when a linearly polarized light wave propagates through a medium with a longitudinal internal magnetization, **M**. The light exiting from the medium gets its polarization plane rotated by a certain angle, θ_F with the appearance of an ellipticity, ϵ_F. This is known as the MO Faraday effect. For a given material of length l, the magnitude of Faraday effect depends on the longitudinal component of **M**. For diamagnetic materials, which do not possess any spontaneous magnetization, the Faraday rotation (FR) angle for an incident light wave propagating in the z-direction through a medium subjected to an external magnetic field $\boldsymbol{H_0}$, is expressed as:

$$\theta_F = VlH_{0z} \tag{1.5}$$

where V is a constant of proportionality, called the Verdet constant, and is defined in terms of the rotation per unit length per unit magnetic field strength. The Verdet

constant of a given material is a function of both the incident wavelength, λ_0 and the ambient temperature T.

$$V = V(\lambda_0, T)$$

Figure 1.2 shows the dependence of Verdet constant of a microscopic glass slide as a function of incident wavelength (400-900 nm).

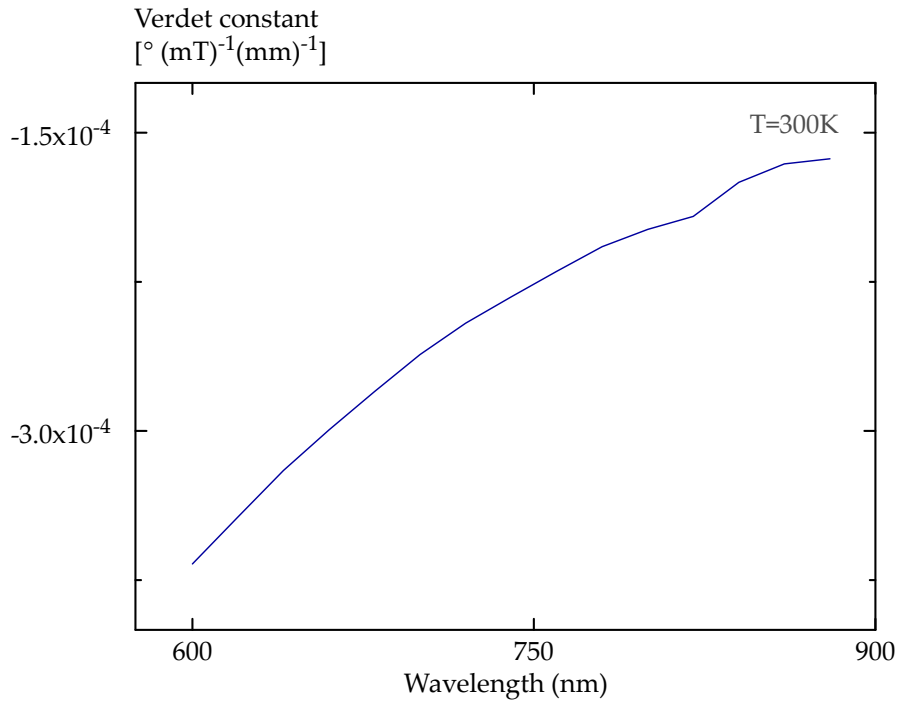

Figure 1.2: Experimentally measured Verdet constant of glass at 300K as a function of incident wavelength.

Now, let us have a look on the physical origin of the Faraday effect. Consider a medium with a magnetically-induced optical anisotropy due to the presence of an internal magnetization, **M** pointing in the z-direction. As mentioned in the previous section, this is manifested as non-zero off-diagonal elements of the permittivity tensor 1.3. If a linearly polarized light wave, also propagating in the z-direction, is incident on the medium, it can be represented as follows:

$$\vec{E} = \vec{E_0}\, e^{i(kz-\omega t)} \qquad \text{with } E_0 \in \mathbb{R} \tag{1.6}$$

where k denotes the propagation constant of the wave and is expressed as follows:

$$k = Nk_0$$

where k_0 is the incident wavevector $= 2\pi/\lambda_0$ and N is the complex refractive index of the medium, represented as in equation 1.4. Solving Maxwell's equations with equation 1.6, permittivity tensor 1.3 and assuming $\epsilon_{xx} = \epsilon_{yy}$ results in two eigen waves having different indices of refraction, N. One solution is a Right-Circularly Polarized (RCP) wave with an index of refraction N_+, while the other is a Left-Circularly Polarized (LCP) wave with an index of refraction N_-. These two refractive indices are linked to the permittivity tensor by the following relation:

$$N_\pm = n_\pm + i\kappa = \sqrt{\epsilon_{xx} \pm \epsilon_{MO}} \tag{1.7}$$

Thus, an incident linear polarization has to be decomposed on these two circular eigenstates. Precisely, a linearly polarized light can be resolved into two oppositely polarized circular light waves and in turn, two circularly polarized light waves of opposite orientation can be vectorially added to result in a linearly polarized light [22]. Within the medium, the RCP wave travels with a velocity c/n_+ while, the LCP wave travels with a velocity c/n_-. If $n_+ \neq n_-$ and $\kappa_+ \neq \kappa_-$, each circular component of the incident wave travels through the medium of length l with different velocities and different absorption giving rise to a complex phase difference, ϕ. It is expressed as follows:

$$\phi = \frac{2\pi}{\lambda}(N_+ - N_-)l \tag{1.8}$$

This complex phase-difference results in the output wave exiting this medium to have its polarization plane rotated by a certain angle. This is known as the Faraday effect. The Faraday angle is expressed as:

$$\theta_F = \mathrm{Re}\left\{\left(\frac{\phi}{2}\right)\right\} = \mathrm{Re}\left\{\left[\frac{\pi}{\lambda}(N_+ - N_-)l\right]\right\} \tag{1.9}$$

and the Faraday ellipticity is expressed as:

$$\varepsilon_F = -\tanh \mathrm{Im}\left\{\left(\frac{\phi}{2}\right)\right\} = -\tanh \mathrm{Im}\left\{\left[\frac{\pi}{\lambda}(N_+ - N_-)l\right]\right\} \tag{1.10}$$

Replacing $N_\pm$ by the permittivity tensor elements using equation 1.7, we get the following expressions for Faraday effect:

$$\theta_F = \mathrm{Re}\left\{\left[\frac{\pi}{\lambda}(\sqrt{\epsilon_{xx} + \epsilon_{MO}} - \sqrt{\epsilon_{xx} - \epsilon_{MO}})l\right]\right\} \approx \boxed{\left(\frac{\pi}{\lambda}\right) \mathrm{Re}\left[\frac{\epsilon_{MO}}{\sqrt{\epsilon_{xx}}}\right] l} \tag{1.11}$$

and,

$$\varepsilon_F = -\tanh \mathrm{Im}\left\{\left[\frac{\pi}{\lambda}(\sqrt{\epsilon_{xx} + \epsilon_{MO}} - \sqrt{\epsilon_{xx} - \epsilon_{MO}})l\right]\right\} \approx \boxed{\left(\frac{\pi}{\lambda}\right) \mathrm{Im}\left[\frac{\epsilon_{MO}}{\sqrt{\epsilon_{xx}}}\right] l} \tag{1.12}$$

Here, the assumption $\epsilon_{MO} << \epsilon_{xx}$ is used which is true for many MO materials used for practical applications. For instance, for Bismuth substituted Yttrium Iron Garnet (Bi:YIG), one of the highly preferred MO materials, $\epsilon_{MO} = 0.005$ and $\epsilon_{xx} = 4.84$ [23]. An interesting property of Faraday effect is that it is non-reciprocal. This means that the sense of the FR does not depend on the direction of wave propagation but only on the direction of magnetization, **M**. Thus, if a light wave passes through a medium with a longitudinal magnetization, and somehow retraces its original path in the opposite direction, the amount of Faraday effect is doubled, rather than canceled. Figure 1.3 schematically depicts this behavior.

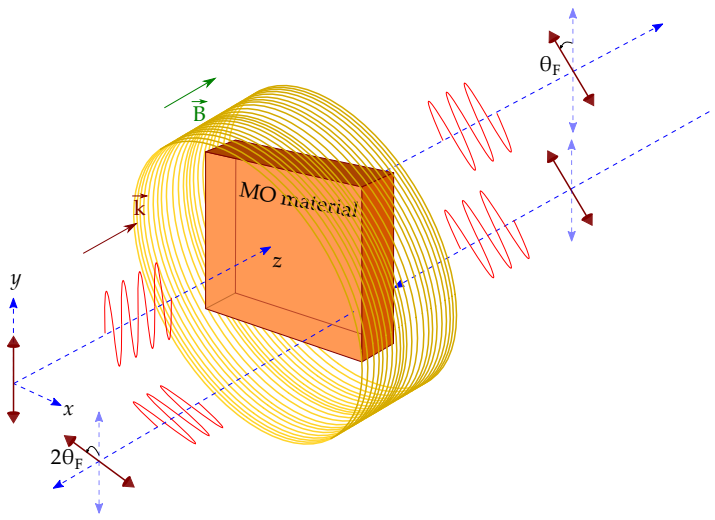

Figure 1.3: Schematic diagram of a MO medium exhibiting non-reciprocal behavior of FR. Similar non-reciprocity occurs for Faraday ellipticity, but is avoided here for clarity.

Applications of this effect are used in optical isolators (devices that transmit light only in one direction) that serve to prevent back-reflections in lasers and circulators (multiple-port devices that transmit light from one port to another) in telecommunication systems [24].

FR is measured in degrees, however to quantify the intrinsic MO activity of a material, it is convenient to define a new parameter called **specific FR**, expressed in ($^\circ$cm^{-1}) as:

$$\theta_F^{sp} = \frac{\text{FR } (^\circ)}{\text{thickness of the medium (cm)}} \tag{1.13}$$

Analyzing equation 1.11, it is evident that the Faraday angle is a function of the magneto-optical parameter, ϵ_{MO} which, in turn is a function of the magnetization, $\vec{M}$ and the incident wavelength, λ_0 for a given material at a given temperature. The inset of figure 1.4 demonstrates this dependence with an experimentally measured

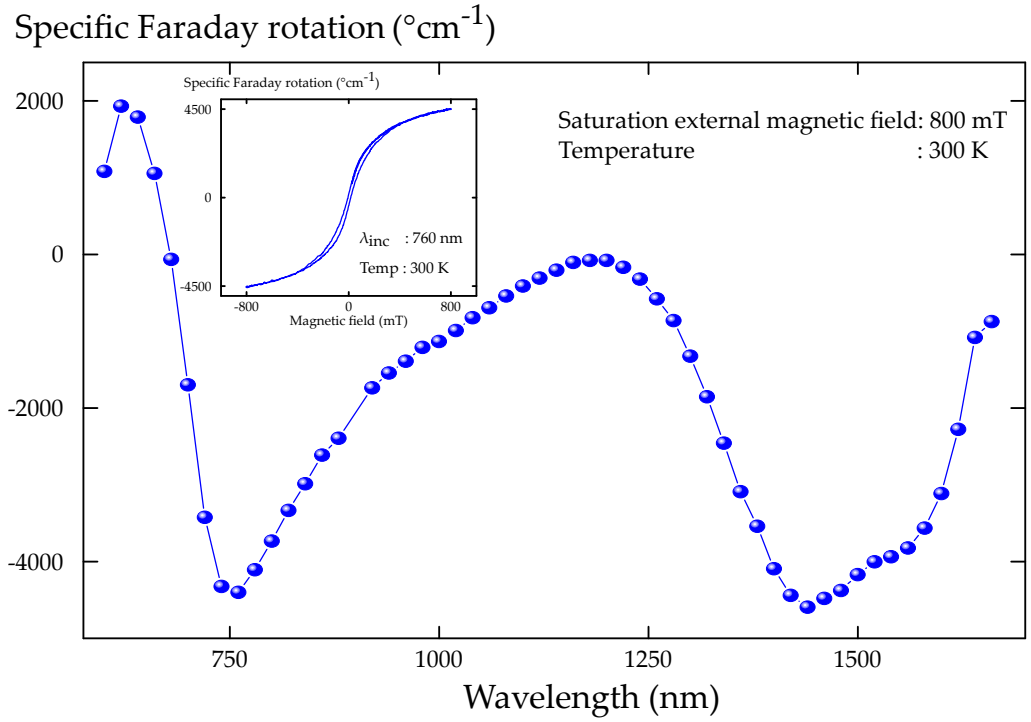

Figure 1.4: Experimentally measured values of specific FR, θ_F^{sp} as a function of the incident wavelength (600-1700 nm) at a saturation external magnetic field of 800 mT at 300 K. The sample is a thin-film of cobalt ferrite nanoparticles embedded in a silica matrix. The inset gives the behavior as a function of the applied field at 760 nm.

result of the FR as a function of the applied magnetic field through a thin film sample of Cobalt ferrite NPs (volume fraction of 22%) embedded in a silica matrix at an incident wavelength of 760 nm at room temperature. At low-fields, the behavior is linear with a small hysteresis, and a saturation appears at high field. This is the behavior of the magnetization of the sample illustrating that the FR effect is proportional to the magnetization through ϵ_{MO}. Figure 1.4 shows the measured spectral dependence of specific FR ($^\circ cm^{-1}$) at an applied external magnetic field of 800 mT for the same sample, demonstrating regions of high FR near 750 nm and near 1550 nm [25].

1.1.3 Magneto-Optical effects in reflection mode

MO effects in reflection mode are called MO Kerr effects and have the same physical origin as MO Faraday effect. They result in a change of the polarization properties and/or of the light intensity when a linearly polarized light gets reflected from a magnetized medium. When a linearly polarized optical wave travels through or is

reflected by an isotropic, non-magnetic medium; it could be in either of its two eigenmodes (waves that preserve their polarization while propagating through a medium):

- Transverse Electric (TE) polarization, where the direction of the incident $\vec{E}$ lies perpendicular to the incidence plane (XOZ in the schematic of table 2.1) or,
- Transverse Magnetic (TM) polarization, where $\vec{E}$ of the incident light is parallel to the incidence plane.

However, when it is incident on a magnetized medium, the off-diagonal elements of the permittivity tensor of this medium induce a coupling between the two polarizations or modify the reflectivity depending on the magnetization orientation. There are three configurations of the MO Kerr effect based on the direction of $\vec{M}$:

- Polar Magneto-Optical Kerr Effect (PMOKE): the magnetization, $\vec{M}$ is normal to the medium surface from which the incident light is reflected.
- LMOKE: the magnetization, $\vec{M}$ is contained in the plane of incidence and is parallel to the medium surface from which the incident light is reflected.
- TMOKE: the magnetization, $\vec{M}$ is perpendicular to the plane of incidence.

Table 2.1 summarizes the MO Kerr effect configurations with a schematic depiction of each effect.

MOKE	Schematic diagram	Polarization	Permittivity tensor, ϵ	Effects
PMOKE	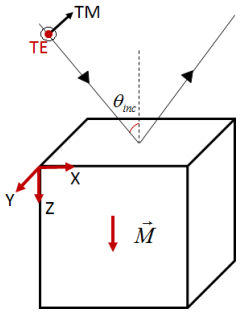	TE, TM	$\begin{bmatrix} \epsilon_{xx} & -i\epsilon_{MO} & 0 \\ i\epsilon_{MO} & \epsilon_{yy} & 0 \\ 0 & 0 & \epsilon_{zz} \end{bmatrix}$	Rotation, Ellipticity
LMOKE	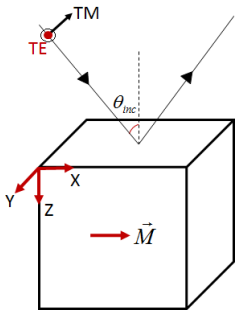	TE, TM	$\begin{bmatrix} \epsilon_{xx} & 0 & 0 \\ 0 & \epsilon_{yy} & -i\epsilon_{MO} \\ 0 & i\epsilon_{MO} & \epsilon_{zz} \end{bmatrix}$	Rotation, Ellipticity
TMOKE	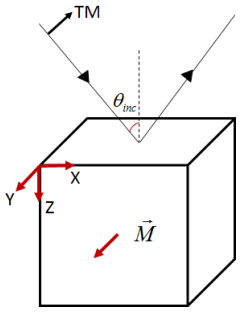	TM	$\begin{bmatrix} \epsilon_{xx} & 0 & -i\epsilon_{MO} \\ 0 & \epsilon_{yy} & 0 \\ i\epsilon_{MO} & 0 & \epsilon_{zz} \end{bmatrix}$	Change of intensity

Table 1.1: Table summarizing the different configurations of MO Kerr effect.

For the polar and longitudinal cases, both TE and TM polarized incident waves have non-zero components of $\vec{E}$ perpendicular to the direction of $\vec{M}$, which, as explained in the previous section, results in circular birefringence when the incident light hits the medium's surface. Consequently, for these two configurations, the magnetic material induces a coupling between the TE and TM polarizations. The net result is a reflected light wave having its polarization plane rotated by an angle, called Kerr rotation angle, θ_K and the introduction of a ellipticity, called Kerr ellipticity, ε_K. Their magnitudes depend on the incidence angle, θ_{inc} and on the magnitude of ϵ_{MO}.

For **PMOKE**, the mathematical expressions for **Kerr rotation** and **ellipticity** (considering the incident medium to be air) are given as [1]:

$$\theta_K = \mathrm{Im}\left\{ \frac{N^2\left[[N^2 - \sin^2(\theta_{inc})]^{1/2} \mp \sin(\theta_{inc})\tan(\theta_{inc})\right]}{(N^2-1)(N^2-\tan^2(\theta_{inc}))} \left(\frac{\epsilon_{MO}}{\epsilon_{xx}}\right) \right\} \tag{1.14}$$

and,

$$\varepsilon_K = \mathrm{Re}\left\{ \frac{N^2[N^2 - \sin^2(\theta_{inc})]^{1/2} \mp \sin(\theta_{inc})\tan(\theta_{inc})}{(N^2-1)(N^2-\tan^2(\theta_{inc}))} \left(\frac{\epsilon_{MO}}{\epsilon_{xx}}\right) \right\} \tag{1.15}$$

Similarly, for **LMOKE**, **Kerr rotation** and **ellipticity** are given as:

$$\theta_K = \mathrm{Im}\left\{ \frac{\sin(\theta_{inc})N^2\left[\sin(\theta_{inc})\tan(\theta_{inc}) \pm \sqrt{N^2 - \sin^2(\theta_{inc})}\right]}{[N^2-1][N^2-\tan^2(\theta_{inc})][N^2-\sin^2(\theta_{inc})]^{1/2}} \left(\frac{\epsilon_{MO}}{\epsilon_{xx}}\right) \right\} \tag{1.16}$$

and,

$$\varepsilon_K = \mathrm{Re}\left\{ \frac{\sin(\theta_{inc})N^2\left[\sin(\theta_{inc})\tan(\theta_{inc}) \pm \sqrt{N^2 - \sin^2(\theta_{inc})}\right]}{[N^2-1][N^2-\tan^2(\theta_{inc})][N^2-\sin^2(\theta_{inc})]^{1/2}} \left(\frac{\epsilon_{MO}}{\epsilon_{xx}}\right) \right\} \tag{1.17}$$

where N is the complex index of refraction of the magnetized medium. In case of an incident medium other than air, N should be replaced by η, the ratio of refractive index of the superstrate to that of the magnetized medium ($N/n_{superstrate}$). The upper sign corresponds to TE-polarization of light, and the lower sign corresponds to TM-polarization of light. A simplified expression for polar Kerr rotation and ellipticity in the case of normal incidence is expressed as follows:

$$\theta_K = \mathrm{Im}\left\{ \frac{\epsilon_{MO}}{N(N^2-1)} \right\} \tag{1.18}$$

and the Kerr ellipticity, ε_K as:

$$\varepsilon_K = \mathrm{Re}\left\{ \frac{\epsilon_{MO}}{N(N^2-1)} \right\} \tag{1.19}$$

The **Transverse Magneto-Optic Kerr effect** (**TMOKE**) is slightly different from the other two Kerr effects. According to its configuration, it is only the TM polarized incident wave, not the TE polarized wave that can interact with the internal magnetization, **M**. Consequently, there is no coupling possible between the two polarizations and hence, no change in the polarization properties of the reflected light is observed. However, there is a modification of the intensity of reflected wave due to an *odd* dependence on the magnetization. It is represented by the parameter δ expressed as follows:

$$\delta(M) = \left(\frac{I_+ - I_-}{I_0} \right) \tag{1.20}$$

where I_+ and I_- denote the output light intensity at saturated values of internal magnetization in the opposite directions. The mathematical expression linking δ to the incidence angle and magneto-optical parameter is given as follows [1]:

$$\delta = -\,\mathrm{Im}\left\{ \frac{4\tan(\theta_{inc})N^2}{(N^2-1)(N^2-\tan^2(\theta_{inc}))} \left(\frac{\epsilon_{MO}}{\epsilon_{xx}} \right) \right\} \tag{1.21}$$

It is evident from the above equations that at normal incidence, LMOKE and TMOKE vanishes whereas, PMOKE reaches its maximum value. Figure 1.5 shows a simulation of Polar and Longitudinal Kerr rotations for a bulk material of Bi:YIG as a function of the incident angle of light with $\epsilon_{xx}^{Bi:YIG} = 4.98 + i0.005$ and $\epsilon_{MO}^{Bi:YIG} = 0.005$ [23].

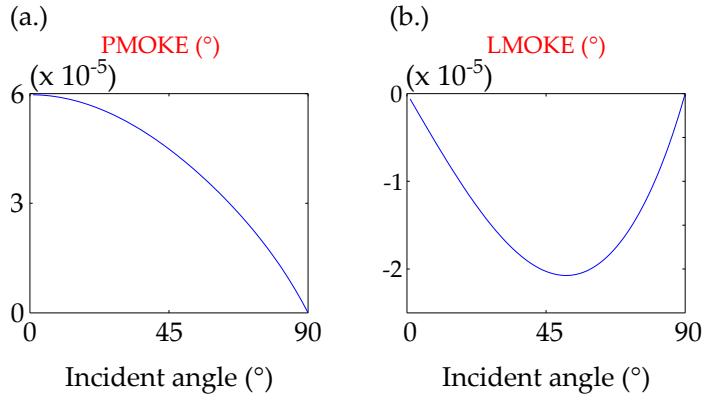

Figure 1.5: PMOKE (a.) and LMOKE (b.) rotations as a function of incident angle for a bulk material of Bi:YIG with TE-polarized incidence at 1550 nm.

1.1.4 Magneto-Optic materials

MO devices have many technological applications ranging from light polarization control to data storage to even magnetic domain research [26]. Properties such as circular birefringence and non-reciprocity offer functions very difficult to achieve with other photonic devices. A quantity frequently used to characterize magneto-optic materials, in addition to the FR angle, is known as the material's **Figure-of-Merit** (FoM), defined as the ratio of the FR to the absorption loss incurred in the material. It is represented as follows:

$$FoM = \frac{\text{Specific FR angle } (^\circ\text{cm}^{-1})}{\text{absorption loss (dB cm}^{-1})} \tag{1.22}$$

Table 1.2 shows the specific FR and FoM with corresponding wavelengths for different kinds of materials at room temperature reported in literature. Iron garnets such as Yttrium Iron Garnet (YIG) or Cerium-substituted Yttrium Iron Garnet (Ce-YIG) are currently the most preferred MO materials since they are transparent in the near IR region and possess high values of specific FR. For instance, Onbasli *et al.* [7] demonstrated specific FR as high as 5800°cm^{-1} at 1500 nm for epitaxial films of Ce:YIG 80 nm thick grown on Gadolinium Gallium Garnet (GGG) substrates. The FoM reaches 943°dB^{-1}. Mino *et al.* [27] demonstrated a specific FR value for a Bismuth Iron garnet (BIG) film equal to 3440°cm^{-1} at 1550 nm. However, magnetic garnets have some drawbacks preventing their incorporation in optoelectronic devices and integrated photonic circuits. First, due to a lattice parameter mismatch and thermal expansion mismatch, they cannot be grown easily on common photonic substrates [28] such as glass, silicon, GaAs and require garnets as their substrates [29]. Good quality iron garnet films require fabrication methods such as pulsed laser deposition [30] [31], sputtering [27], liquid phase epitaxy [32] [33] etc. Second, they have a high crystallization temperature ($> 700^\circ$C). To circumvent this problem, progress is being made on the hybrid integration of iron garnet films on glass or semiconductor substrates by direct bonding [34] [35]. Alternatively, the search and development of other MO materials compatible with classical technologies also constitutes an active area of research today. Zayets *et al.* [36] [37] reported a MO semiconductor material of CdMnTe on GaAs substrate capable of demonstrating a very high value of FoM [38] at optical frequency.

MO material	Wavelength (nm)	FR angle ($^\circ/cm$)	MO Figure of Merit ($^\circ$dB^{-1})	Ref.
Fe	546	3.5×10^5	0.11	[39]
Co	546	3.6×10^5	0.10	[39]
Ni	400	7.2×10^5	0.79	[39]
$Y_{2.82}Ce_{0.18}Fe_5O_{12}$ (no substrate, bulk crystal)	1550	740	1420	[40]
Single crystalline epitaxial Ce:YIG on GGG substrate	1550	5800	943	[7]
$Bi_{0.55}Yb_{0.92}Fe_5O_{12}$ on YIG substrate	1550	558	30.2	[41]
$Bi_{0.55}Yb_{0.92}Fe_5O_{12}$ on YIG substrate	1300	800	21.5	[41]
Fe:InGaAsP	1550	100	23	[42]
Polycrystalline Ce:YIG on Silica	1550	2700	56	[43]
Fe doped SrTiO3	1550	780	1.11	[44]
$Cd_{1-x}Mn_xTe$ on GaAs substrate	730	≈ 620	200 per kGauss	[38]
Bismuth Iron Garnet (BIG) on NGG substrate	1550	3.44×10^3	160	[27]

Table 1.2: Comparison of MO specific FR, figure of merit for different wavelengths for some MO materials at 1550 nm at room temperature.

Another approach developed by Laboratoire Hubert Curien (LabHC) employs a composite material made of metallic oxide (SiO_2/ZrO_2) matrix doped with fully crystallized magnetic nano-particles of cobalt ferrite, $CoFe_2O_4$ [45]. The sol-gel technique is used to synthesize the magnetic composite. This provides the advantage of a lower thermal treatment of 90°C making its integration with classical technologies easier. Another advantage of this composite is its operational wavelength of 1550 nm making it useful for telecom applications (refer to figure 1.4). The average nano-particle diameter in the composite is measured to be 9 nm and the specific FR from this composite is a function of the volume fraction of the magnetic cobalt ferrite particles.

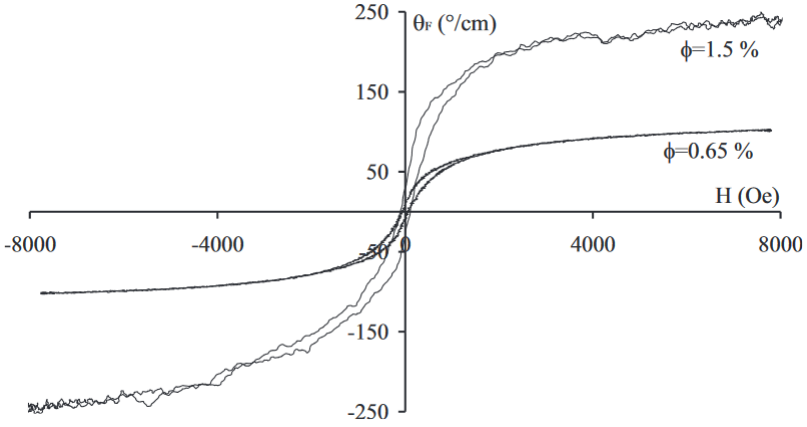

Figure 1.6: Experimental specific FR of silica/zirconia matrix doped with cobalt ferrite nanoparticles at 820 nm for two different volume fraction of the nano-particles, 0.65% and 1.5%. The figure is adapted from [45].

Figure 1.6 shows the specific FR of 0.65% and 1.5% volume fraction of cobalt ferrite nano-particles which reaches a maximum value of $250°cm^{-1}$ at 820nm (and $310°cm^{-1}$ at 1550 nm, not shown here). These values are very promising when compared to those of YIG ($200°cm^{-1}$ at 1550nm [41]). However, in terms of FoM, the silica/zirconia composite doped with cobalt ferrite nano-particles yield a FoM = $2.3°dB^{-1}$ at 1550 nm which is quite lower than that of iron garnets (see table 1.2) but still is higher than other alternative MO materials. But a major advantage of this material is its ability to impregnate 3-D nanostructures [46] [47] which gives a good opportunity to realize 1-D MO periodic devices. The material used in this work is cobalt ferrite NPs embedded in a silica matrix.

1.1.5 Guided Magneto-Optics

Guided-wave optics is the physics of transmitting optical power from one position to another using optical confinement in a material medium rather than in free space. Such a medium is called an optical waveguide. The basic principle of optical confinement is total internal reflection i.e. a light ray traveling from a denser medium to a rarer medium gets totally reflected back to the denser medium if its incidence angle (measured from the interface) is less than a critical angle. This section focuses solely on the physics of planar dielectric waveguides consisting of a dielectric slab of refractive index, n_f sandwiched between a substrate and cover material with lower refractive indices n_s and n_c, respectively (see figure 1.7).

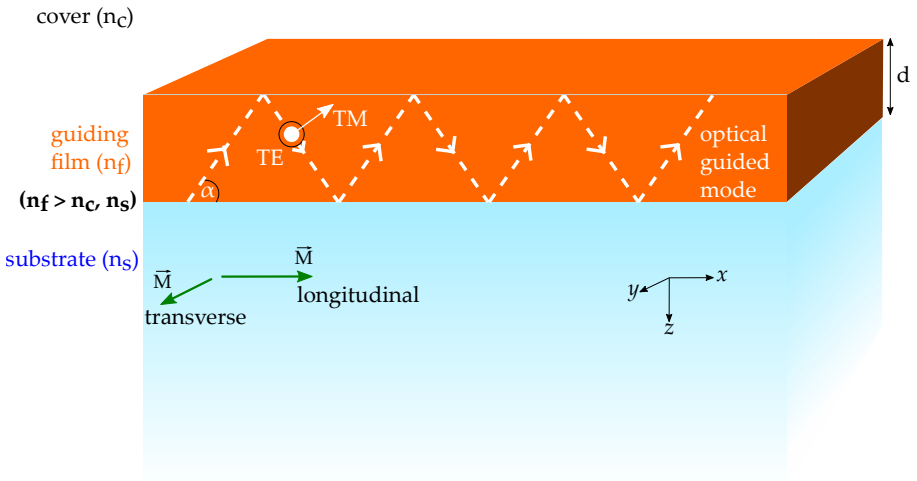

Figure 1.7: Schematic of an asymmetric planar dielectric waveguide showing the propagation of guided-modes as total-internal-reflection of light rays.

The confined light ray is called a "guided-mode" of the waveguide. If it makes an angle α with the interface as it propagates, one can define its propagation constant β and its effective refractive index N_{eff} as follows:

$$\beta = k_0 n_f \cos(\alpha) = k_0 N_{eff} \tag{1.23}$$

Also, this light ray accumulates a phase-shift in each reflection at the dielectric interface. For a light wave with its electric field vector, $\boldsymbol{E}$ parallel to the interface, called TE light wave, the phase shift at total-internal reflection can be expressed as:

$$\phi_{TE} = -2 \arctan\left(\sqrt{\frac{N_{eff}^2 - n_j^2}{n_f^2 - N_{eff}^2}}\right) \tag{1.24}$$

and, for a light wave with its magnetic field vector, $\boldsymbol{H}$ parallel to the interface, called TM light wave, the phase shift at total-internal reflection can be expressed as:

$$\phi_{TM} = -2\arctan\left(\left(\frac{n_f^2}{n_j^2}\right)\sqrt{\frac{N_{eff}^2 - n_j^2}{n_f^2 - N_{eff}^2}}\right) \tag{1.25}$$

In equations 1.24 and 1.25, n_j represents the refractive index of either the cover or the substrate depending on which interface the total-internal-reflection is taking place. Now, when the light ray (TE or TM) travels from one film boundary to the opposite film boundary, in addition to the phase change accumulated in traveling that distance, there are two other phase shifts introduced due to total internal reflection at the two boundaries, ϕ_s and ϕ_c. To obtain constructive interference, the following condition holds true:

$$2n_f k_0 \sin(\alpha) d + \phi_c + \phi_s = 2\pi m$$

or

$$2k_0 d\sqrt{n_f^2 - N_{eff}} + \phi_c + \phi_s = 2\pi m \tag{1.26}$$

where m is an integer and represents the mode number of the wave being guided in the medium n_f. Equation 1.26 is a transcendental eigen-value equation and physically signifies that for every value of mode number m, there exists a unique effective index N_{eff} corresponding to it. Since the phase shifts ϕ_c and ϕ_s are different for TE and TM polarizations, one obtains two different eigenvalue equations for each polarization. Using equation 1.24, 1.25 and 1.26, one gets:
For TE waves:

$$k_0 d\sqrt{n_f^2 - N_{eff}^2} - \arctan\left(\sqrt{\frac{\beta^2 - n_c^2 k_0^2}{n_f^2 k_0^2 - \beta^2}}\right) - \arctan\left(\sqrt{\frac{\beta^2 - n_s^2 k_0^2}{n_f^2 k_0^2 - \beta^2}}\right) = m\pi \tag{1.27}$$

Figure 1.8 graphically shows the TE-mode dispersion characteristics of a dielectric waveguide for different values of guided-mode number m. Guided-modes exist only in the region bounded by the lower bound $(c/n_f)k_0$ and upper bound $(c/n_s)k_0$ in discrete values. As ω increases, more and more guided-modes can exist. The first three guided modes $(m = 0, 1, 2)$ are shown.

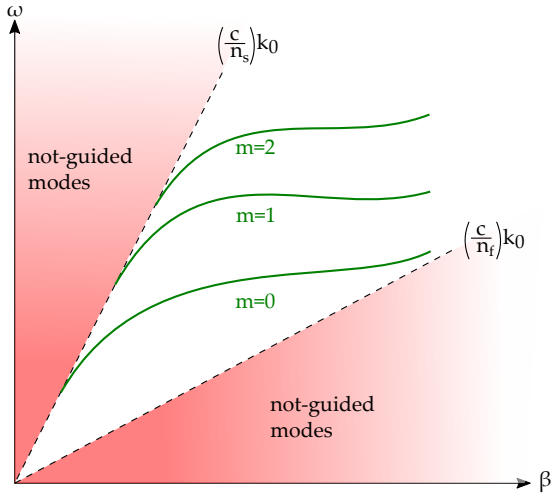

Figure 1.8: Dispersion relation (β Vs. ω) for a dielectric waveguide.

Similarly, for TM waves:

$$k_0 d\sqrt{n_f^2 - N_{eff}^2} - \arctan\left(\frac{n_f^2}{n_c^2}\sqrt{\frac{\beta^2 - n_c^2 k_0^2}{n_f^2 k_0^2 - \beta^2}}\right) - \arctan\left(\frac{n_f^2}{n_s^2}\sqrt{\frac{\beta^2 - n_s^2 k_0^2}{n_f^2 k_0^2 - \beta^2}}\right) = m\pi \tag{1.28}$$

It is evident from this figure and from the dispersion relations 1.27 and 1.28 that for a fixed set of physical parameters n_c, n_s, n_f and d, the effective indices are not equal for the two types of modes i.e.

$$N_{eff}^{TE} \neq N_{eff}^{TM} \tag{1.29}$$

To illustrate such a difference figure 1.9 gives a graphical representation of the TE and TM effective indices deduced from equations 1.27 and 1.28 as a function of the thickness, d of the waveguide.

We now consider a guided-mode propagating in the x-direction in a magnetic material. When a longitudinal magnetization is present (refer to figure 1.7), there is a coupling between the TE- and TM-polarization due to the off-diagonal element, ϵ_{MO}. The origin of this coupling is identical to that of the Faraday effect. But as the two modes do not have the same propagation constants (phase-mismatch), the coupling efficiency η, is limited to a maximum value expressed as follows:

$$\eta = \frac{|\kappa|^2}{|\kappa|^2 + (\Delta\beta/2)^2} \tag{1.30}$$

where

$$\Delta\beta = \beta_{TE} - \beta_{TM} = \left(\frac{2\pi}{\lambda_0}\right)\left(N_{eff}^{TE} - N_{eff}^{TM}\right)$$

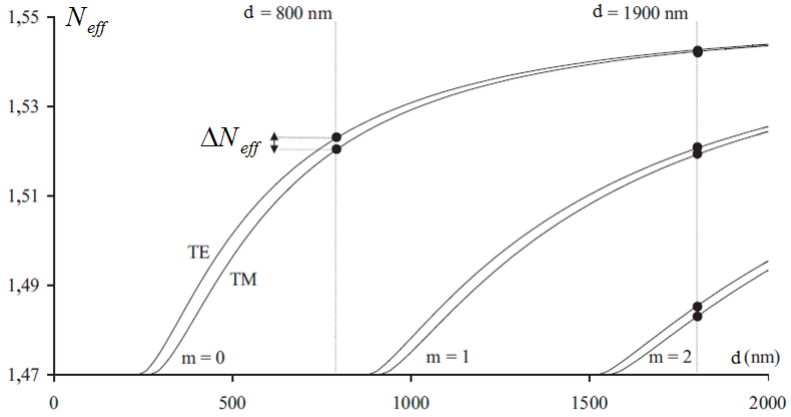

Figure 1.9: Graphical representation of the TE 1.27 and TM 1.28 eigen-value equations for $\lambda_{inc} = 633nm$ as a function of the waveguide height d. The indices of refraction for the cover, film, and substrate as 1, 1.55, and 1.47 respectively. The figure is adapted from [48].

and, κ is the coupling strength of TE-TM polarization of the medium which is proportional to the off-diagonal tensor elements of the dielectric permittivity tensor and to the "quantity" of field contained in the MO film. In first approximation, one can consider that κ is equal to the specific FR ($^\circ cm^{-1}$). Equation 1.30 signifies that for $\eta \to 1$, $\Delta\beta$ must tend to 0. Thus, to obtain an efficient MO conversion, special efforts have to be made to reduce this value as much as possible. In the case of a transverse magnetization (refer to figure 1.7), the TE mode does not interact with the magnetization but only the TM mode. In such a situation, the dielectric permittivity tensor can be expressed as (refer equation 1.3):

$$\epsilon = \begin{bmatrix} \epsilon_{xx} & 0 & i\epsilon_{MO} \\ 0 & \epsilon_{yy} & 0 \\ -i\epsilon_{MO} & 0 & \epsilon_{zz} \end{bmatrix} \tag{1.31}$$

The eigen value equation for the TM_0 polarized mode gets modified to as follows:

$$d\sqrt{k_0^2\epsilon_{eff} - \beta} = \arctan\left(\frac{\epsilon_{eff}}{\sqrt{k_0^2\epsilon_{eff} - \beta^2}}\left(\frac{\sqrt{\beta^2 - k_0^2\epsilon_c}}{\epsilon_c} - \frac{\beta\epsilon_{MO}}{\epsilon_{xx}\epsilon_{eff}}\right)\right) + \arctan\left(\frac{\epsilon_{eff}}{\sqrt{k_0^2\epsilon_{eff} - \beta^2}}\left(\frac{\sqrt{\beta^2 - k_0^2\epsilon_s}}{\epsilon_s} + \frac{\beta\epsilon_{MO}}{\epsilon_{xx}\epsilon_{eff}}\right)\right) \tag{1.32}$$

where

$$\epsilon_{eff} = \epsilon_{xx} - \frac{\epsilon_{MO}^2}{\epsilon_{xx}}$$

It is evident that when ϵ_{MO} is zero i.e. when there is no magnetization, equation 1.32 collapses to equation 1.28. Because of the addition of terms containing the

magneto optical constant, ϵ_{MO} which is an odd function of the magnetization, the propagation constant β is different for two counter-propagating waves. This signifies that the phase accumulated in traveling a finite distance in the guiding medium in two opposite directions is not the same, hence resulting in a non-reciprocal behavior. This property can be used to realize integrated photonic applications such as an integrated optical isolator.

Enhancing the MO properties of a nano-/micro-scale material can permit the realization of miniaturized devices with higher sensibility compared to that of bulk materials. This can be done by altering the mechanism in which light interacts with matter which is the focus of the next section.

1.2 Resonant structures

1.2.1 Photonic crystals

Photonic crystals (PhCs) are materials with a periodic spatial variation in their dielectric constant which can resonantly interact with incoming radiation having a wavelength comparable to the characteristic period of the material [49] [50]. Depending on the dimensionality of periodicity, they can be classified as 1-D, 2-D and 3-D PhCs.

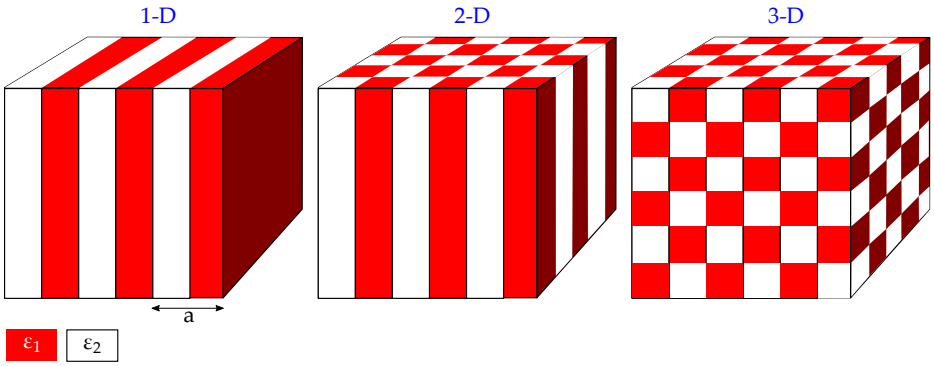

Figure 1.10: Schematic illustration of the types of photonic crystals (PhCs): 1-D, 2-D and 3-D. *'a'* is the periodicity.

They are important because they can demonstrate a photonic band gap (PBG), similar to the energy band gap in semiconductors, wherein those wavelengths are prohibited to propagate through the crystal. To calculate the optical modes in a PhC one needs to solve Maxwell's equations in a periodic dielectric medium. For the

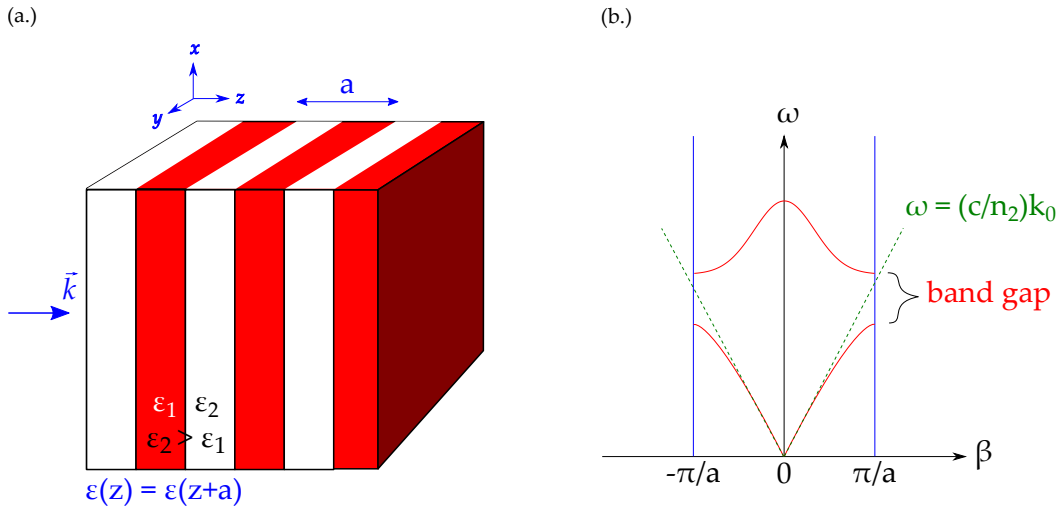

Figure 1.11: (a.) Schematic illustration of a 1-D PhC periodic in the z-direction with periodicity 'a' (b.) Corresponding dispersion relation in the first Brillouin zone (unit cell in the reciprocal lattice space) (marked by two vertical solid lines). Dashed lines represent the light line.

simplest case of a 1-D PhC of period a, figure 1.11 represents the dispersion relation for a 1D photonic crystal. Referring to figure 1.11(b.), it can be seen that for certain angular frequencies ω, there is no corresponding propagation constant β. These regions correspond to the Photonic Band Gap. Light cannot propagate through the crystal when its frequency lies in the PBG. It can also be seen that near the photonic band gap edge, the curve "flattens" representing that the group velocity of the wave $(d\omega/d\beta)$ tends to zero thereby increasing the interaction of light with the PhC. Physically, for wavelengths lying in the PBG, the waves that are reflected from each layer of the crystal are in-phase and so, constructively interfere with one another, meanwhile forming a standing wave in the material that does not propagate through the crystal. Photonic crystals provide new ways of controlling light. They have many practical applications such as in lasing [51] [52], sensing [53] [54], LEDs [55] [56], telecommunications, slow light [57] [58] and quantum optics [59] [60].

1.2.2 Guided-Mode Resonance

Guided-Mode Resonance (GMR) is the phenomenon wherein incident light is resonantly reflected from a system due to excitation of "leaky" optical guided-modes. For light which is incident at an angle θ_{inc} from free-space onto a planar system, the condition for it to couple with a guided-mode of the system requires the axial

component of the incident light, i.e. $n_c k_0 sin\theta_{inc}$ to be equal to the propagation constant β of the excited guided-mode. This constraint is called the phase-matching condition for excitation of an optical guided-mode. Since $\beta > n_c k_0$, it is not possible to fulfill the phase-matching condition (see figure 1.12(a.)). However, with the help of a diffraction grating it is possible to modify the wavevector of incident light such that the phase-matching condition is fulfilled. By using a grating with period Λ, the axial component of the incident wavevector is modified by factors $q2\pi/\Lambda$, where $q = \pm 1, \pm 2, \pm 3...$(see figure 1.12(b.)) In such a case, satisfaction of the phase matching condition can be achieved by a suitable choice of the grating period Λ. The phase-matching condition for a waveguide-grating structure can be expressed as follows:

$$\boxed{n_c k_0 sin\theta_{inc} + q\left(\frac{2\pi}{\Lambda}\right) = \beta_m = N_{eff}^m k_0} \qquad \text{Phase-matching condition} \qquad (1.33)$$

where n_c is the refractive index of the cover medium, k_0 is the incident wavevector and β_m is the propagation constant of m^{th} guided-mode excited in the waveguide. These excited modes are termed "leaky" or "quasi-" guided modes as they get attenuated over distance because of the periodicity which also induces an out-coupling. The observed resonance in reflected light intensity can be attributed to a 180° phase-difference between the transmitted light waves resulting in destructive interference and consequently, a constructive interference in reflection (refer figure

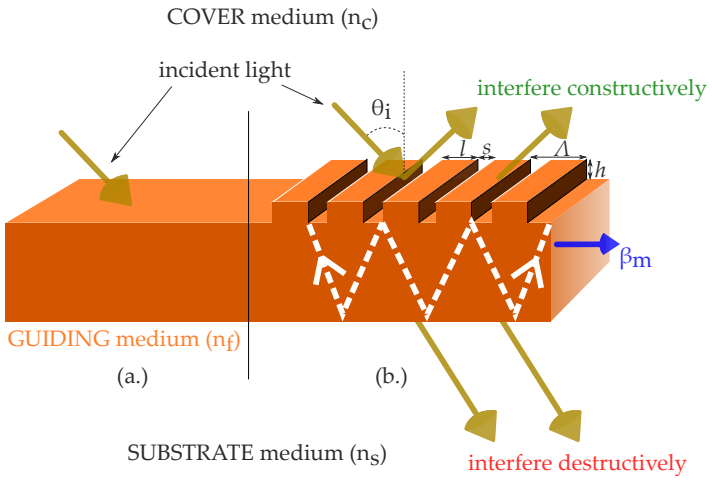

Figure 1.12: Schematic illustration showing an incident light not being able to fulfill the phase-matching condition to excite optical guided-modes in the underlying planar system (a.) and, a waveguide-grating structure able to satisfy the phase-matching condition (b.).

1.12(b.)) [61], [62]. Thus, one observes a minimum in transmittance and consequently a peak in reflectance, illustrated in figure 1.13. The phenomenon of GMR has found many practical applications such as in narrow-band reflection filters and modulators.

A proper choice of the structural and orientation parameters can aid in modifying the resonance profile of such resonant guided-mode structures. For instance, figure 1.13 shows how the resonance can be varied spectrally upon modification of the grating parameters using rigorous coupled wave analysis [63]. The height of the guiding medium is fixed at 500 nm with a refractive index of 1.6 (same refractive index for the grating material as well) on a silica substrate of refractive index $1.45 + i0$. Figure 1.13(b.) and (d.) are consistent with the phase-matching condition according to which changing the grating period and incident angle will shift the resonance in wavelength. Figure 1.13(c.) shows the dependence on the grating fill-factor f (defined as line-width l, divided by the period). Figure 1.13(e.) shows the spectral reflectance curves for TE and TM polarized incidence.

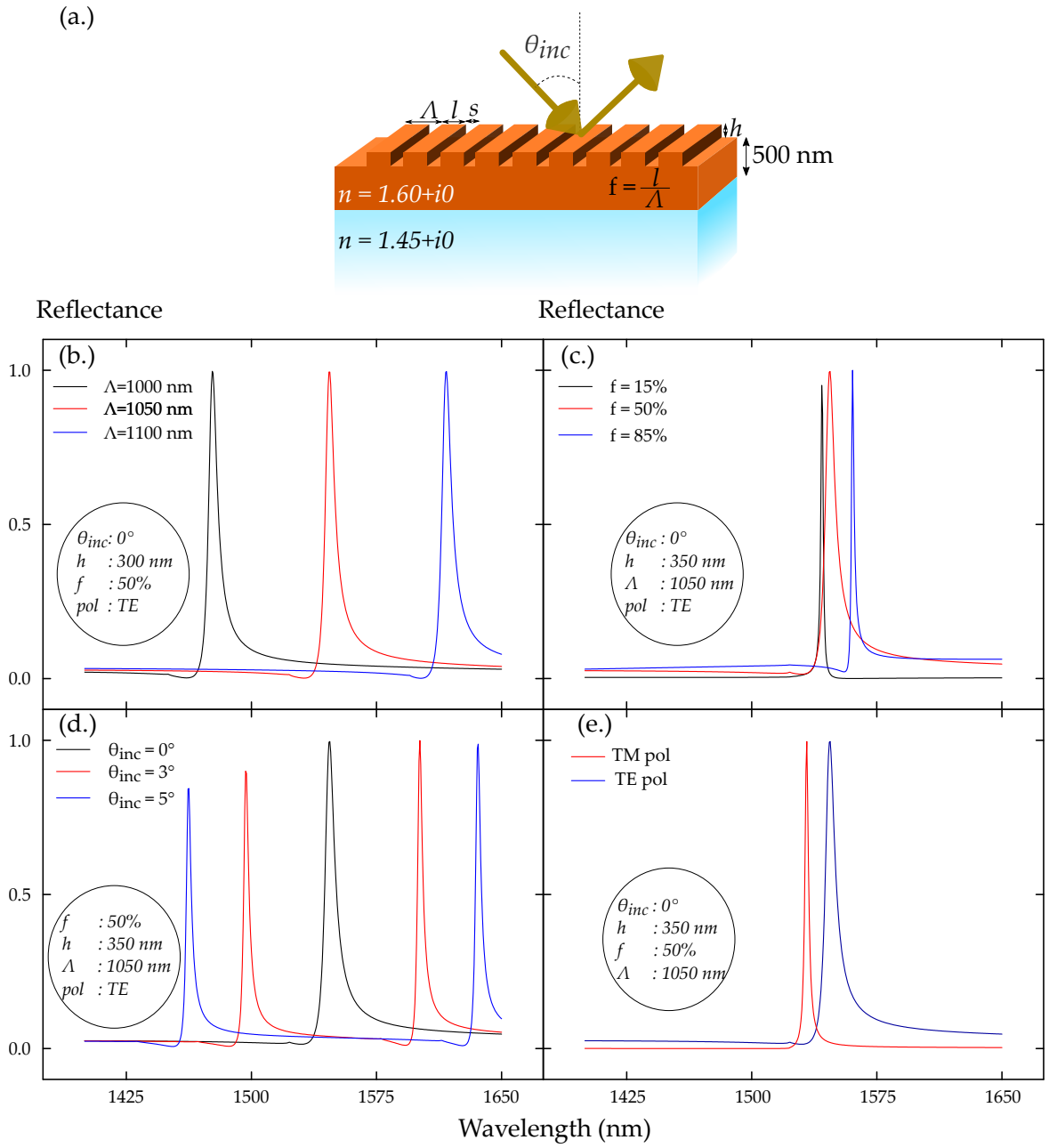

Figure 1.13: Effect of variation of physical and orientation parameters on the reflectance of a waveguide grating structure. (a.) Schematic diagram of simulated waveguide grating. (b.) Variation of grating period, Λ. (c.) Variation of fill-factor, f. (d.) Variation of incident angle, θ_{inc}. (e.) Variation of incident polarization.

It is important to note that resonant WGSs are, in general, polarization-dependent i.e. the spectral position of TE polarized resonance, in general does not coincide with that of a TM polarized resonance for a given set of structural parameters. This is due to the fact that for a dielectric waveguide, $\beta_{TE} \neq \beta_{TM}$ and thus, the phase matching condition 1.33 can not be satisfied for the same waveguide. However, illuminating the structure in conical mounting (when the incident plane makes an angle with the grating vector) makes the incident light (let's say TE light) possess a finite TM component as well, resulting in simultaneous TE and TM spectral. Also, by using 2-D perforation on the planar system makes it indifferent to the incident polarization at normal incidence enabling simultaneous phase-matching of TE and TM modes in the guiding medium. Nevertheless, even for a 1-D case, it has been experimentally demonstrated [64] that by modifying the fill factor and grating height, it is possible to have a resonant excitation of both TE and TM polarization at the same structural and orientation parameters. Alasaarela *et al.* [64] demonstrated this with a periodically modulated (1-D) thin-film waveguide using TiO_2 on fused silica substrate (refer to figure 1.14 (a.)). A resonance in reflection was demonstrated as a function of incident wavelength (figure 1.14 (c.)) for numerically calculated parameters for which the propagation constants of the TE and TM modes are equal (figure 1.14 (b.)). In such a structure, it is the grating that also serves as a guiding medium for the excited optical mode.

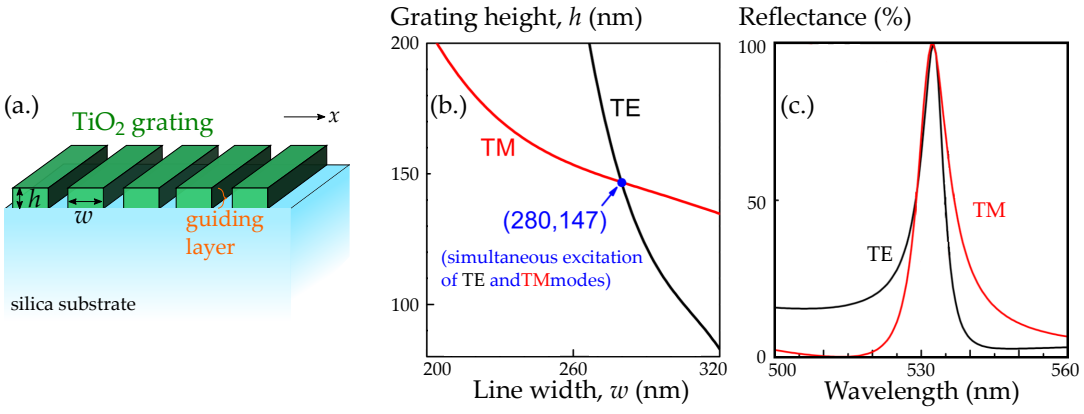

Figure 1.14: (a.) Schematic of a thin-film waveguide periodically perforated in 1-D (b.) Numerical simulation of the relation between its line width, w and grating height, h. The point of intersection represents the parametric position at which the TE and TM modes have the same propagation constant, β. (c.) Numerical simulation of the TE and TM reflectance using the intersection parameters. The figure is adapted from [64].

Equal values of propagation constant for the two modes are important in the context of TE-TM polarization conversion efficiency. Referring to equation 1.30 when $\Delta\beta \rightarrow 0$, the efficiency of polarization conversion from one mode to another tends to 100%. It will be seen in the next section how such a situation can aid in unique MO effects. Another way of achieving TE-TM polarization independent resonance is by fabricating a diffraction grating with a metal and consequently, exciting simultaneously TM surface plasmons polaritons and TE dielectric modes. Let us focus first on Surface Plasmon Resonance.

1.2.3 Surface Plasmon Resonance

Surface plasmon polaritons (SPPs) are coupled oscillations of the EM field and the electron plasma in a metal propagating at the interface between the metal and a dielectric, evanescently confined in the perpendicular direction [65]. They exist only for TM polarization. The dispersion relation of SPPs propagating at the interface between two semi-infinite metal/dielectric media can be expressed as follows:

$$\beta_{SPP} = k_0 \sqrt{\frac{\epsilon_m \times \epsilon_d}{\epsilon_m + \epsilon_d}} \tag{1.34}$$

where ϵ_m and ϵ_d are the relative permittivity of metal and dielectric respectively. If the planar dielectric medium has an internal magnetization in the transverse direction, the dispersion relation gets modified as:

$$\beta_{SPP} = k_0 \sqrt{\frac{\epsilon_m \times \epsilon_d}{\epsilon_m + \epsilon_d}} (1 + \alpha \epsilon_{MO}) \tag{1.35}$$

where

$$\alpha = \frac{1}{(\sqrt{-\epsilon_m \epsilon_d})(1 - (\epsilon_d^2/\epsilon_m^2))}$$

and ϵ_{MO} is the MO anisotropy previously defined as the MO constant. As in the case of a dielectric waveguide, a transverse magnetization induces a non-reciprocal modification of the propagation constant of the TM mode. Due to the absorption losses in metals, usage of plasmons in optoelectronic applications is a concern. However, it can be overcome with the phenomenon of Extra-ordinary Optical transmission (EOT) wherein an abnormally large transmission is observed in perforated metal films such that, at the resonant frequency the structure is more transparent than the smooth metal film [66]. Figure 1.15 shows an EOT calculated for a metal grating for different grating heights. For structures with a metal diffraction grating on top

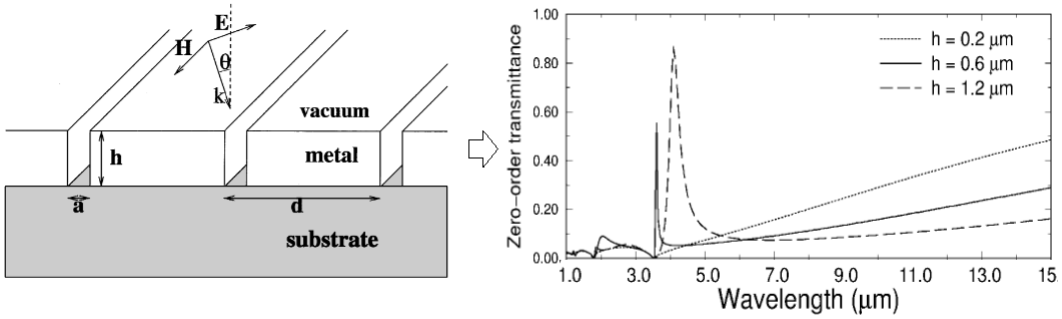

Figure 1.15: 1-D metal grating demonstrating enhanced optical transmission (EOT) for TM polarized light for different grating heights. The figure is adapted from [67].

of a planar dielectric waveguide, excitation of surface plasmon polaritons can result in a TM polarization resonance whereas the excitation of a TE guided-mode in the planar dielectric waveguide can cause a TE polarization resonance.

Using the basic concepts of magneto-optics detailed in section 1.1, and the main configurations to obtain an optically resonant structure detailed in this section, we will now focus on the gathering of these two ideas by studying the enhancement of magneto optical effects using a periodic arrangement.

1.3 Magneto-Optic enhancement

1.3.1 Magneto-Photonic Crystals

When the constitutive materials or even a single defect in a photonic crystal is magnetic, the resultant, known as magneto-photonic crystals can cause resonant magneto-optic behavior. For instance, the presence of a magnetic defect in a PhC has the capability to localize light and thus, enhancing its interaction with the constituents of the PhC. Inoue *et al.* [68] [69] theoretically demonstrated that a large enhancement in FR angle can be obtained in the 1-D magneto-PhCs with micro-cavity structures with a magnetic defect introduced in the periodicity. The theoretical predictions were experimentally confirmed using a multi-layer micro-cavity structure of $(Ta_2O_5)^5/SiO_2/Bi:YIG/(SiO_2/Ta_2O_5)^5$ [70]. Figure 1.16 shows the transmittance and FR angle for the structure.

The PBG of the structure is between 650 nm and 800 nm. However, due to the presence of the magnetic defect (Bi:YIG layer), a localized mode appears at 720 nm resulting in an enhanced transmission and FR angle (10 times compared with that

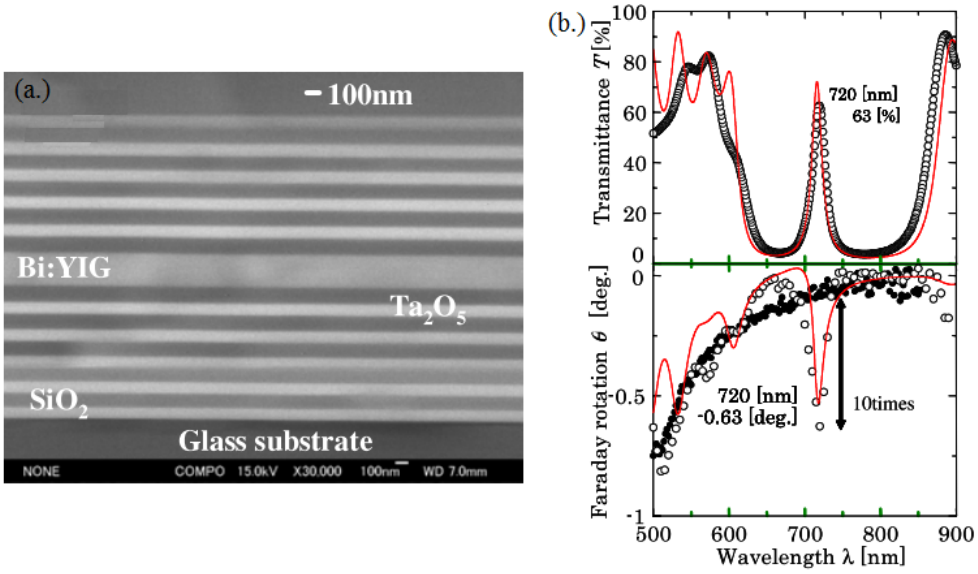

Figure 1.16: (a.) Cross-sectional SEM image of 1-D microcavity structure of $(Ta_2O_5)^5/SiO_2/Bi:YIG/(SiO_2/Ta_2O_5)^5$. (b.) Spectral dependence of the optical transmittance and FR of the structure. The figure is adapted from [70].

of a single Bi:YIG film) due to Fabry-Perot resonance [71]. Yoshimoto *et al.* [72] report a 30 times enhancement of FR with an identical configuration but with a MO defect layer of Ce:YIG to work around 1550 nm. The specific FR of such a magneto-photonic crystal is calculated to be $-6.9°\mu m^{-1}$ which is impressive in this wavelength range compared to other works [73–75].

Figure 1.17 shows the experimental optical and magneto-optical (FR) results for a periodic multi-layer structure of $(SiO_2/Bi:YIG)^5/Bi:YIG$ [76] [77]. In this structure, since there is no magnetic defect in the periodicity, there is no localized state causing a resonance. But enhancements near the PBG edges are present. Optical transmission of the structure clearly shows a region of low transmission corresponding to the PBG between 850 nm and 1100 nm reaching values as low as 0.12 at 965 nm. The same graph shows the FR angle of the structure. At the two edges of the PBG, there is an enhancement of FR with values as high as 8 times (at the longer wavelength edge) when compared to that of a single Bi:YIG film. The reason for enhancement is the "flattened" dispersion curve (see figure 1.11) at the band edge of a PhC causing the group velocity of the light wave to be zero thus increasing the interaction of light with the magnetic material. Similar MO enhancements from periodic magneto-PhC have been reported in [78] [79]. Kekesi *et al.* [46] experimentally fabricated a 3-D inverse opal magneto-PhC of silica composite

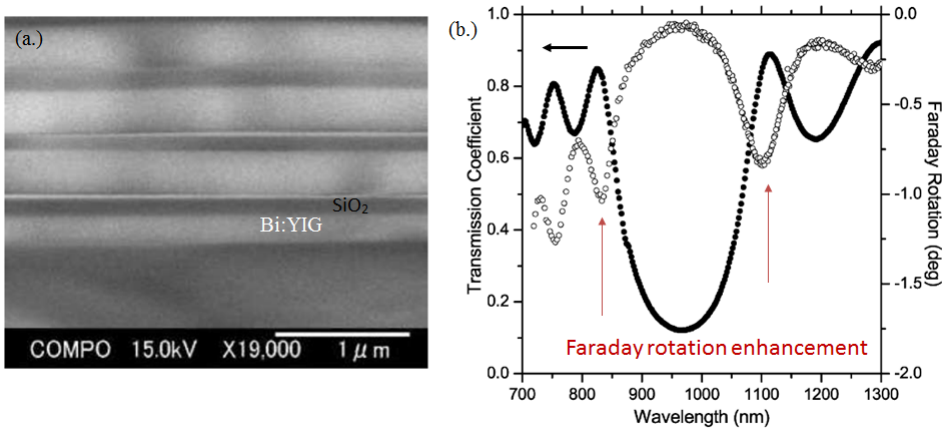

Figure 1.17: (a.) Cross-sectional SEM image of 1-D periodic structure of $(SiO_2/Bi:YIG)^5/Bi:YIG$. (b.) Spectral dependence of the optical transmittance (filled dots) and FR (open dots) of the structure. The figure is adapted from [76].

doped with magnetic cobalt ferrite nanoparticles (volume fraction of 8%) wherein the composite acts as the high-refractive index material and the air voids as the one with low-refractive index. Figure 1.18 shows a Scanning Electron Microscope (SEM) image of the fabricated inverse opal magneto-PhC.

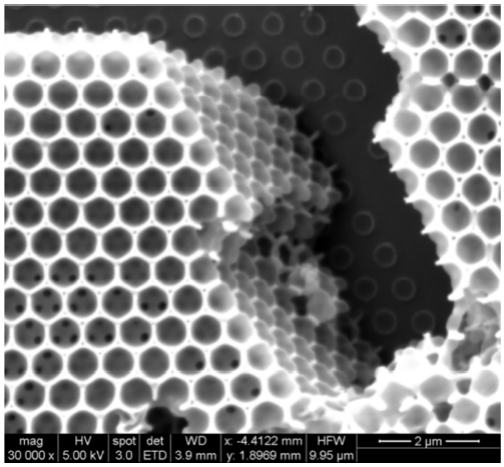

Figure 1.18: (a.) SEM image of a 3D magneto-PhC of inverse opals with silica composite doped with magnetic cobalt ferrite nanoparticles. The figure is adapted from [46].

Figure 1.19 demonstrates the optical and magneto-optical results of the inverse opal. It shows the existence of a PBG of the inverse opal centered around 720 nm. And, its spectral position is reported to vary linearly as a function of the volume fraction of the magnetic nanoparticles and the nanoparticle diameter. It is also clearly evident that a resonant enhancement of FR and ellipticity near the vicinity of

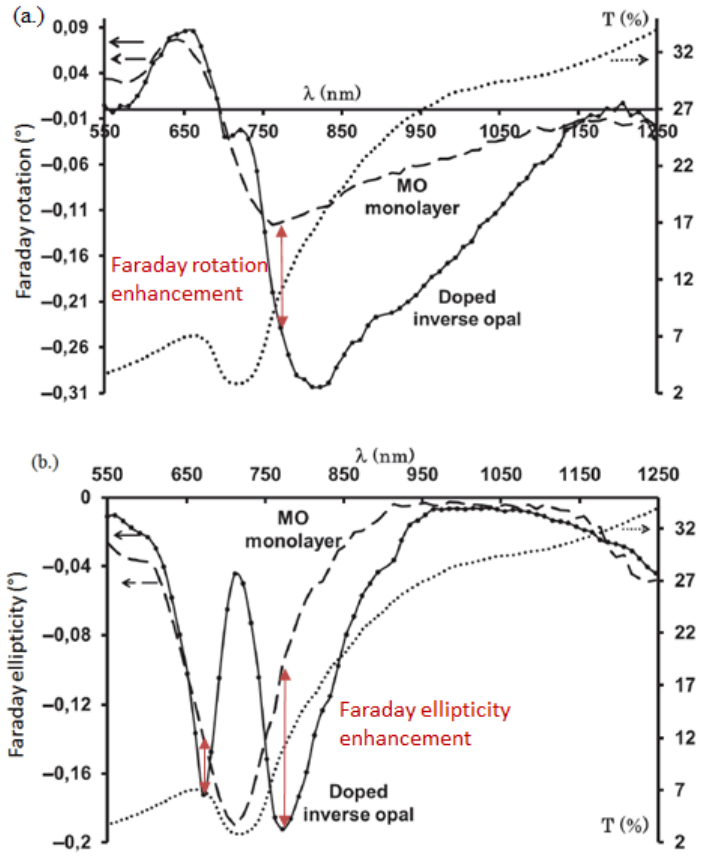

Figure 1.19: (a.) Experimental curves of transmittance (dotted line) and FR (solid line) of the 3-D inverse opal with the FR of a single MO thin film (dashed line). (b.) The same for Faraday ellipticity. The figure is adapted from [47].

the PBG edges is present owing to higher concentration of the electric field intensity in the high-refractive index region i.e. doped silica composite [80]. These results obtained at LabHC prove that an enhancement of Faraday effect can be obtained in a 3-D periodic arrangement of the composite magneto-optical (MO) material. But the use of such material is limited by the low dimension of the arrangement which does not exceed several hundreds of microns to be well-organized. For higher distances, there are cracks or defects in the arrangement which are mainly due to the fact that the elaboration method is based on self-organization.

Based on their ability to resonantly enhance MO effects, magneto-photonic crystals have already found applications in optical isolator devices [81] [82], spatial light modulators [83] and sensing systems [84]. However, PhCs are not the only structures capable of demonstrating a resonance in the MO behavior.

In the next section, resonant enhancement of various MO effects due to planar

micro-structuration of homogeneous thin-film systems are reported.

1.3.2 Planar micro-structuration

By introducing periodic structuration in a planar system containing a magnetic element, it is also possible to modify the spectral MO behavior of the device thanks to guided modes and/or surface plasmon resonances.

1.3.2.a Faraday effect enhancement

In section 1.2.2 it was explained how incident optical power from free-space can be coupled to a guided-mode of a planar system with the help of a diffraction grating. Compared to a free-space optical ray which travels across a film, a guided-mode traverses an increased optical path when guided in the same film. Thus, by using the non-reciprocal nature of magneto-optical effects, an enhancement of these effects might be possible through a coupling to a guided mode. But in the case of polarization conversion like the Faraday effect, the guided configuration requires close values of TE and TM propagation constants; it means $\Delta\beta \approx 0$ (see equation 1.30). Finally, the design of structures dedicated to Faraday effect requires the following conditions:

- A set of physical parameters of the guide and a period of the grating which ensure a resonance effect at the desired wavelength,
- A configuration which allows to simultaneously obtain TE and TM resonance. Ideally, such resonance should be combined with a transmitted light intensity as large as possible in order to maximize the figure of merit.

Several strategies have been led by researchers to fulfill such requirements. The first is to employ a 2-D periodic arrangement which, at normal incidence, gives a full degeneracy of TE- and TM-polarization configuration. Following this concept, Belotelov *et al.* [85] numerically demonstrated a resonant enhancement of FR by a factor of 9 along with a transmission resonance as high as 35% for a 2-D magneto-plasmonic structure containing a perforated metal film on a MO substrate (see figure 1.20). The reference structure was a plain MO material without any structuration. For a dedicated wavelength, the grating diffracts the incident light on metallic SPPs which give rise to the phenomenon of EOT and ensures a resonant peak in the transmitted light intensity. Due to SPPs, the output light has an increased optical

path length as compared to that of a plain MO thin film of the same material and polarization modes being phase-matched, the Faraday effect is enhanced.

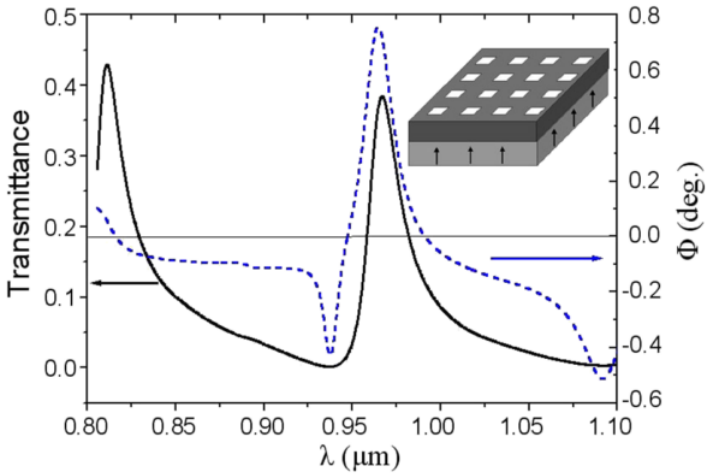

Figure 1.20: (inset) 2-D magneto-plasmonic bilayer system of perforated Au-film of thickness 68 nm and uniform Bi:YIG film of thickness 118 nm with a period of 750 nm and a hole size of 395 nm. Transmittance (left) and FR (right) spectra. The figure is adapted from [85].

Dmitriev *et al.* [86] showed that the use of an intermediate low-index dielectric layer between the metallic grating and the Bi:YIG layer is a way to further increase the FR by a proper choice of the thickness of this layer. Khanikaev *et al.* [6] similarly demonstrated through simulations in a perfect conductor perforated with 2D square-shaped holes filled with MO Bi:YIG, a resonant enhancement of FR as high as 18 times when compared to that of a homogeneous Bi:YIG thin film. Figure 1.21 shows the studied 2-D structure with a theoretical calculation of its Figure of Merit (FoM), defined here as $(\sqrt{T} \times |\theta_F|)$. The reported FoM value for a plain MO Bi:YIG thin-film is upto two orders of magnitude smaller than that for the perforated structure.

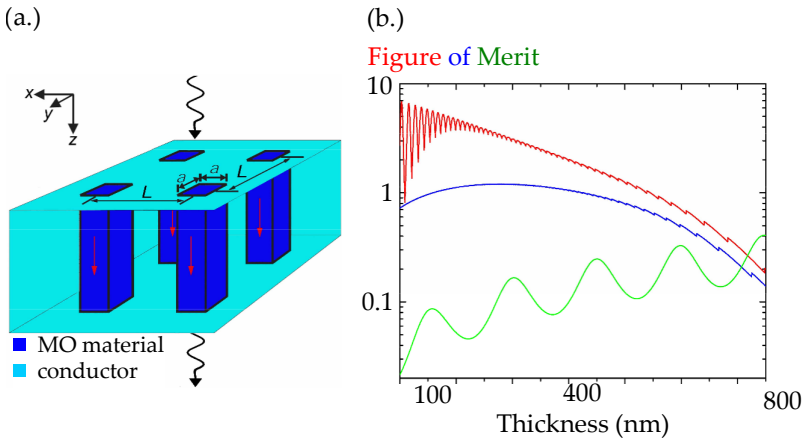

Figure 1.21: Schematic of a metal conductor perforated with square shaped holes filled with magneto-optically active material (Bi:YIG). (b.) Figure of Merit (FoM) as a function of thickness at spectral positions of optical transmission resonance: 703 nm (red) and 709 nm (blue) with that of a homogeneous MO film. The figure is adapted from [6].

Similar enhancements in 2-D magneto-plasmonic systems have been reported in [87] [86]. Another example of FR enhancement is demonstrated by Caballero *et al.* [11] with a theoretical magneto-plasmonic structure made of 2-D perforated holes on a stack of Au-Co-Au layers on a glass substrate (see figure 1.22(a.)). The reason for the MO enhancement is attributed to the excitation of two surface plasmon polaritons at the two Au interfaces (*viz.* Au/air and Au/glass) which also results in an EOT at 585 nm and 710 nm.

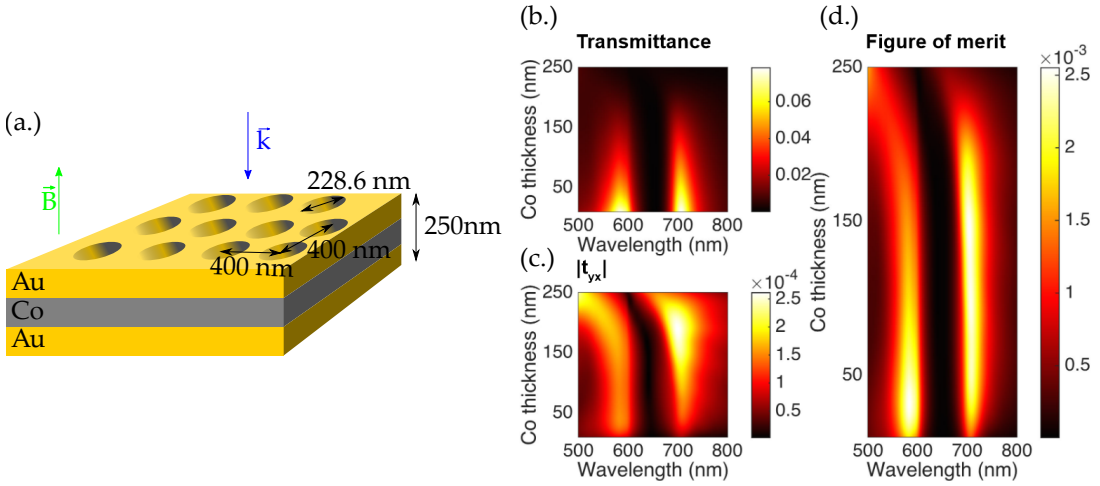

Figure 1.22: (a.) Schematic structure of a Au-Co-Au layer system with 2-D periodicity of holes. Spectral dependence of transmittance (b.), FR (c.) and FoM (d.) on the Co layer thickness. The figure is adapted from [11].

Figure 1.22(b.) and (d.) show the dependence of transmittance and FoM on the Co thickness. A Co layer thickness of 30 nm is more suitable for the smaller wavelength, and 150 nm for the longer one. For both thicknesses, it is reported that the FoM of this structure is more than one order of magnitude larger than in the case of a pure Co layer. Furthermore, an appropriate choice of the surrounding refractive index and thickness of the upper metal layers can increase this FoM. But, the obtained value remains low due to the large absorption of Co and Au materials.

Baryshev *et al.* [88] [89] report an experimental FR enhancement for a Au-Bi:YIG sample consisting of 2-D square lattice of Au disks embedded in a Bi:YIG layer. But, in this system, the resonance manifests itself through the presence of transmission dips due to the excitation of Localized Surface Plasmons (plasmons confined in an area of size comparable to or smaller than the exciting wavelength). Owing to the localization of light at the Au/Bi:YIG interface, resonant Faraday effect is reported at the spectral position of these dips which is less interesting than EOT situations.

However, the condition of using plasmons is not absolutely necessary. Bai *et al.* [90] theoretically demonstrate in an *all-dielectric* structure, that by optimizing the 2-D grating parameters one can effectively excite leaky guided-modes causing localization of the incident field in the system as guided-modes bouncing back-and-forth within the MO material resulting in an enhancement of FR. But this enhancement takes place at the spectral position of transmission dips. Figure 1.23(a.) illustrates the physical parameters of the 2-D structure utilized with corresponding transmittance, FR and Faraday ellipticity (figure 1.23(b.)). For the parameters mentioned, two extremely narrowly spaced, ultra-thin transmission dips are present attributed to the excitation of leaky guided modes in the structure. At each position of these two transmission resonances, asymmetric resonant enhancement of Faraday effect is reported.

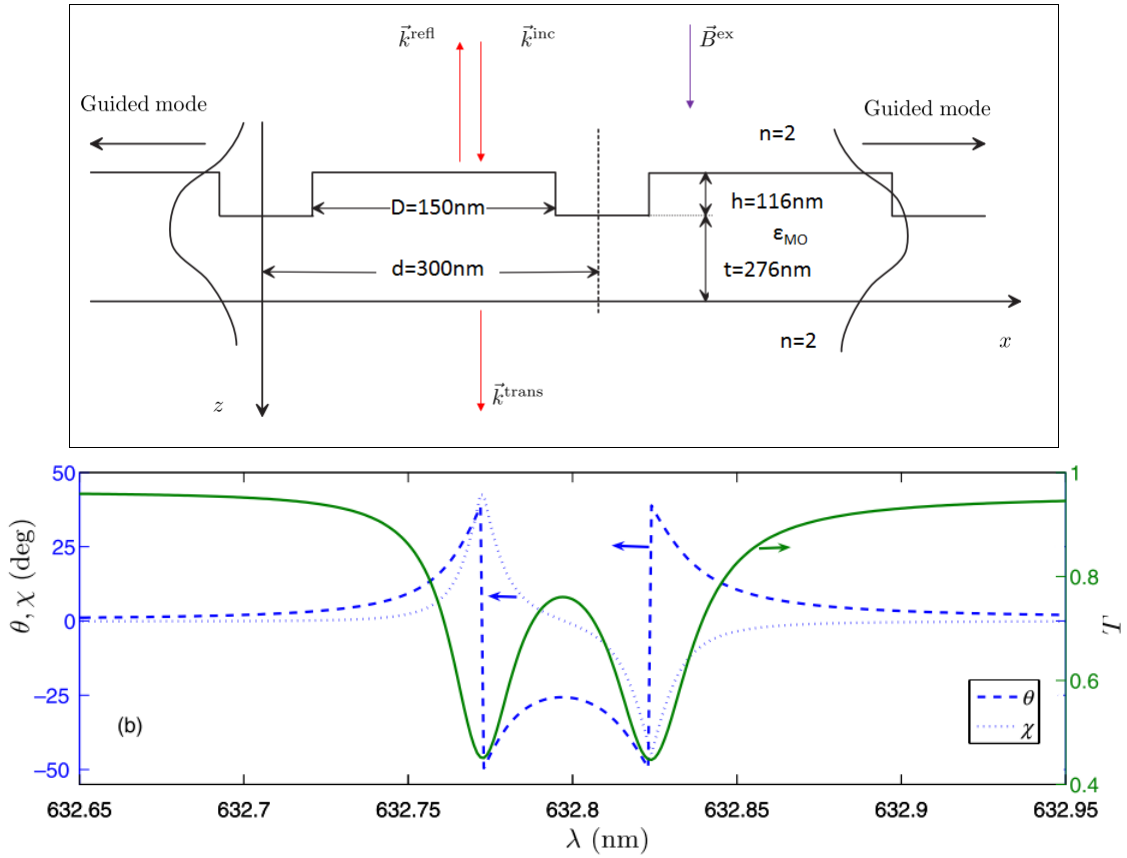

Figure 1.23: (top): Schematic of the cross-section of a 2D magneto-plasmonic structure along with the structural parameters used in [90]. (Bottom): Transmittance (right), FR and Faraday ellipticity (left) calculated by numerical analysis. The figure is adapted from [90].

Another strategy to obtain a phase-matching condition between TE and TM modes is to use 1-D magneto-plasmonic structures which support hybrid dielectric/plasmonic TM-modes. For example, a FR enhancement by 8.9 times compared with that of a continuous MO thin-film along with a transmittance of $\sim 40\%$ is reported by Chin *et al.* [91] on 1D gold-nanowires on top of a thin MO film (figure 1.24(a)). Figure 1.24(b) demonstrates the condition for maximal light polarization rotation which is the point where the dispersion curves for the two fundamental modes, namely TE and TM cross one another. This point of intersection corresponds to the condition $\Delta\beta = 0$ in equation 1.30. The lines in the diagram trace the resonance frequencies of the dielectric TE- and TM-modes in the MO layer for varying grating periods. The two curves remain parallel without any point of intersection. However, because of the metallic grating and owing to the formation of

Waveguide-Plasmon-Polaritons [92], the TM mode is modified to bend over the TE waveguide-mode dispersion curve and an intersection is created.

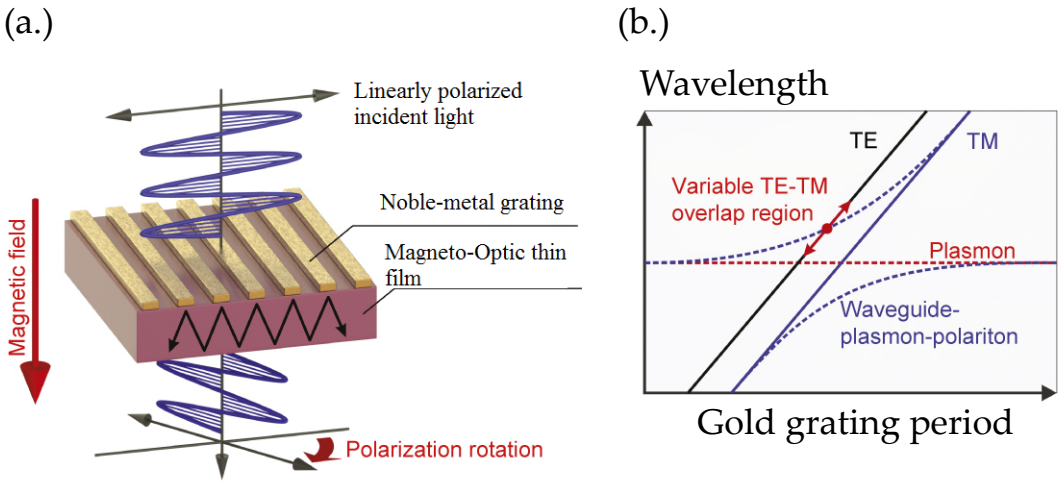

Figure 1.24: (a.) Schematic of a 1-D magneto-plasmonic structure. (b.) Schematic of the dispersion graph of such a magneto-plasmonic structure. The figure is adapted from [93].

Figure 1.25(a.), (b.) and (c.) demonstrate respectively, experimentally measured values of transmittance through a 1-D magneto-plasmonic structure for TE and TM polarized incident radiation and an enhancement in the FR for a range of grating periods near to the intersection of the two dispersion curves for TE and TM modes. Figure 1.25(a.) demonstrates the excitation of a TE-guided-mode in the MO thin film leading to a dip in the transmission spectra which red-shifts as the grating period increases (consistent with the phase-matching equation, 1.33). In figure 1.25(b.) the TM-polarized incident light excites a hybrid mode containing characteristics of a guided-mode and a localized plasmon mode. This excitation manifests itself in two resonances: at the transmission resonance dip at shorter wavelength, the guided-mode resonance is dominant whereas, at the longer wavelength resonance, it is the localized plasmon resonance that dominates. So, as the grating period increases, the plasmon resonance stays put, whereas it is only the guided-mode resonance that shifts. Consequently, the period corresponding to the situation when the two modes are spectrally closest yields the maximum FR enhancement (see figure 1.25(c.)). The FoM reaches a value of 0.48°. Lei *et al.* [9] showed that by using a more complex bilayer structure, it is possible to match an enhanced FR with a transmission peak, reaching a FoM of 0.51.

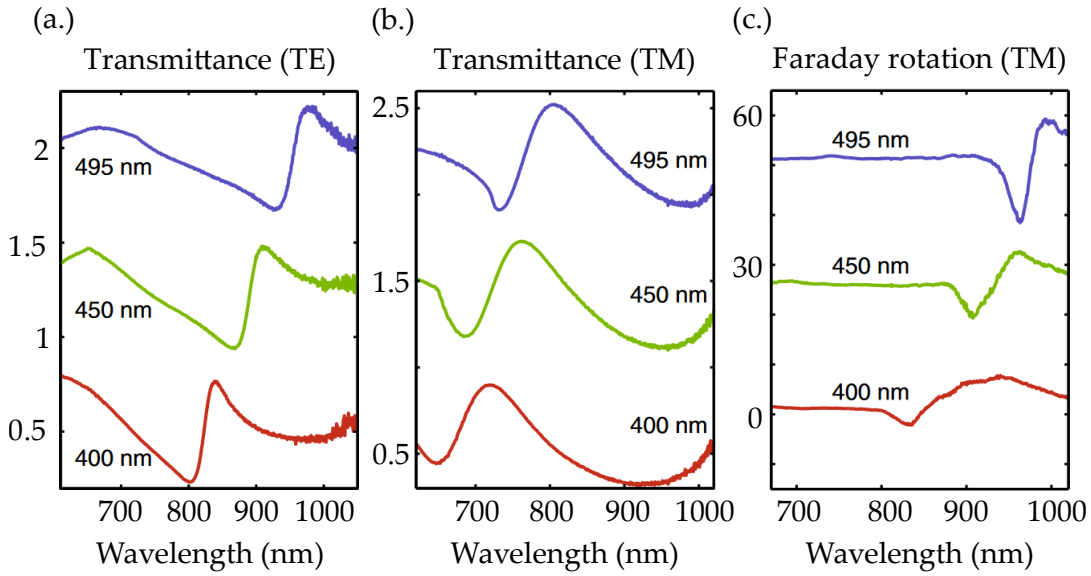

Figure 1.25: (a.)(b.) Experimental transmittance for TE-, TM-polarized incident light, respectively. (c.) Measured values of FR enhancement for different grating periods. The spectra is vertically shifted for clarity. The figure is adapted from [91].

1.3.2.b Polar and Longitudinal Kerr effect enhancement

The geometry of polar and longitudinal Kerr effects is shown in table 2.1. Their effects (obtained in reflection configuration) involve light polarization rotation and ellipticity as well, and as discussed in the previous section, they require an intersection of the TE-and TM-mode dispersion curves for their optimal enhancement. All-dielectric 2-D structures modeled by Bai *et al.* [90] and mentioned in the previous paragraph also demonstrated a theoretical enhancement of PMOKE at the peak of reflectivity of the structure. In a similar sort of structure, Dmitriev *et al.* [86], who used a magneto-optic Bi:YIG substrate with a dielectric thin layer on top of it followed by a 2-D perforated gold thin film at the top, theoretically demonstrated a resonant PMOKE reaching 7.52° with zero ellipticity at an incident wavelength of 1099.6 nm. However, in this case, the PMOKE resonance coincided with the transmission resonance (46%) which meant a dip in reflectance (reflection mode is in which PMOKE is actually measured). Similar behavior of PMOKE and reflectance were reported by Belotelov *et al.* [85] for a 2-D magneto plasmonic structure. Furthermore, for a 1-D system of infinitely long MO nanorods in free-space, Marinchio *et al.* [94] analytically predicted a resonant enhancement of polar and longitudinal Kerr effect. The reason for MO enhancement is explained in terms of induced dipole

moments and their radiation overlap in those MO nanorods.

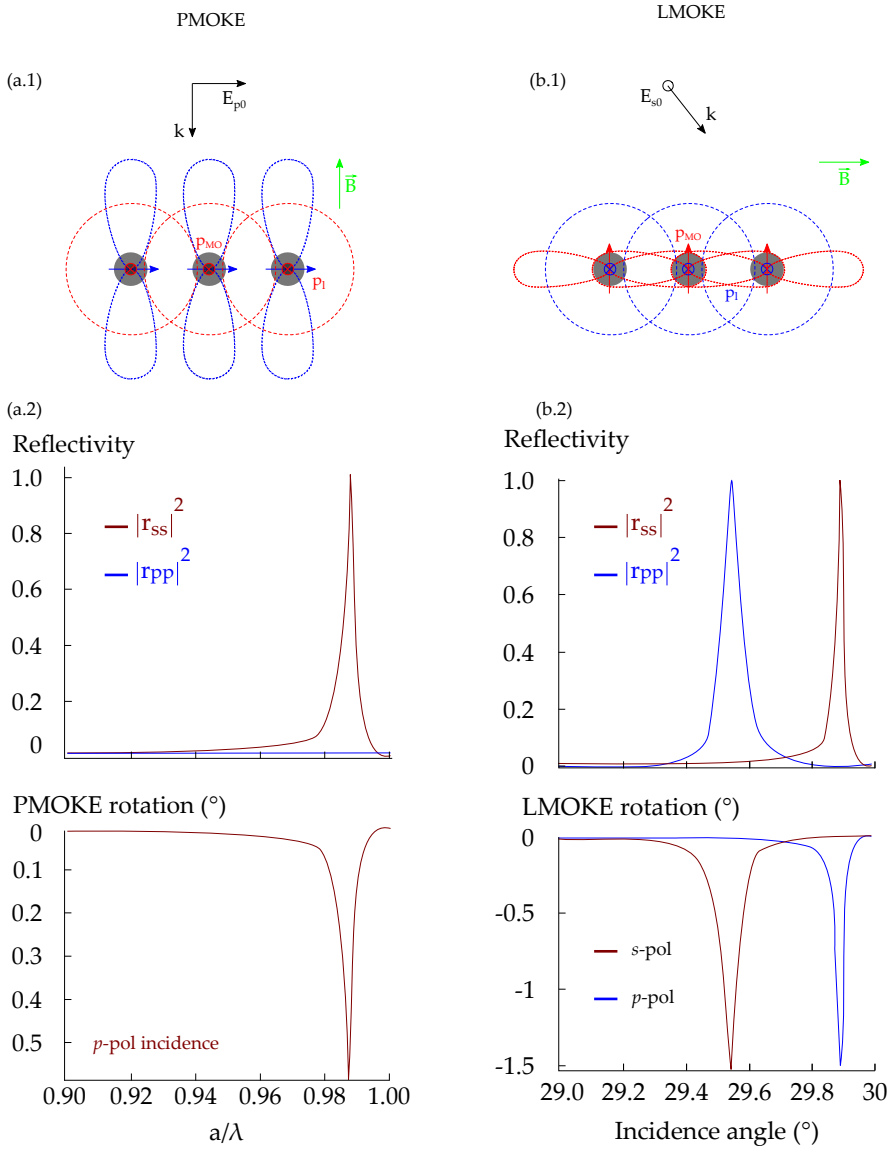

Figure 1.26: (a. and b.) PMOKE and LMOKE configuration: (a.1 and b.1) show the orientation of the isotropic dipole moment (blue) and the MO dipole moment (red) and their scattered-radiation pattern. The figure is adapted from [94].

In the PMOKE configuration (figure 1.26(a.)), the p-polarized (TM) light has weak coupling between the scattered radiations of individual nanorods and so, does not present a resonance. However, for the s-polarized (TE) incident light, due to a possible resonant coupling between the scattered fields, a resonant reflection and Kerr rotation in predicted. In the LMOKE configuration (figure1.26(b.)), both s- and p-polarized light show reflectance and Kerr rotation resonance, again due to

possible resonant coupling between the scattered fields but, for a fixed incidence wavelength the Kerr rotation resonance for one type of polarization lies at the reflectance resonance of the opposite polarization and vice-versa.

Chetvertukhin *et al.* [95] experimentally demonstrated a Kerr rotation angle in LMOKE configuration upto 0.15° at the resonance wavelength coinciding with the dip in the reflectance of a 2-D magneto-plasmonic crystal. Figure 1.27(a.) shows a Scanning Electron Microscope (SEM) image of the 2-D nano-structured Nickel film along with its specular reflectance and longitudinal Kerr rotation (figure 1.27(b.)).

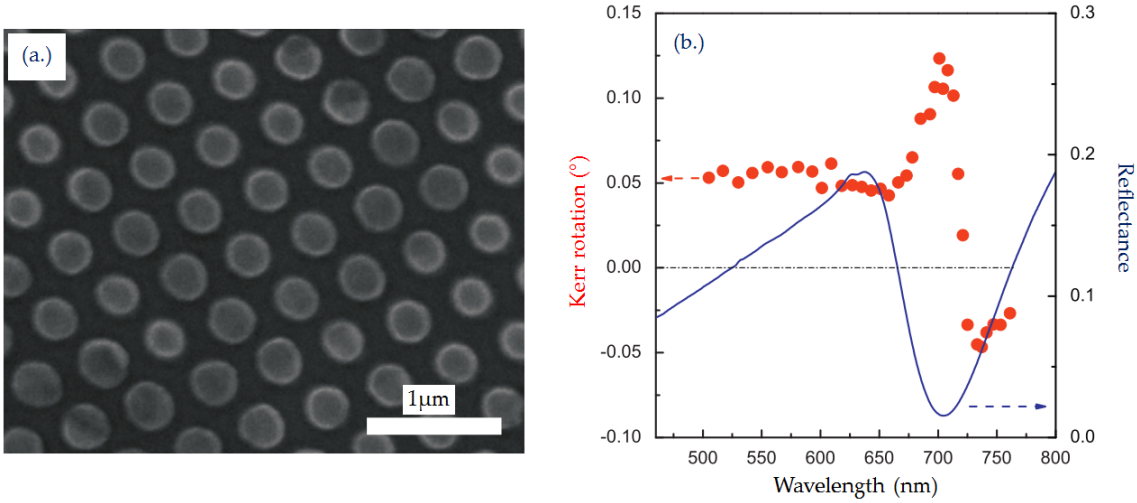

Figure 1.27: (a.) Scanning electron microscope image of a 2-D nanostructured nickel film. (b.) Spectral variation of its reflectance (right) and longitudinal Kerr rotation (left) for p-polarized incident radiation. The figure is adapted from [95].

The dip in specularly reflected light intensity is attributed to the excitation of surface plasmon polaritons (SPPs). This is also confirmed by the fact that no such dip was reported for s-polarized light. These excited SPPs can be expressed as a superposition of two normal modes with right and left circular polarizations [96] whose propagations constants are expressed as follows (refer section 1.2.3):

$$\beta_{SPP}^{\pm} = k_0 \sqrt{\frac{\epsilon_m \times \epsilon_d}{\epsilon_m + \epsilon_d}} (1 \pm \alpha \epsilon_{MO}) \tag{1.36}$$

with α defined as in equation 1.35. The phase-difference between these two components determines the Kerr rotation obtained in specular reflection. The asymmetric lineshape of the LMOKE spectra (figure 1.27(b.)) is due to slightly different phase-match condition for the two SPP modes.

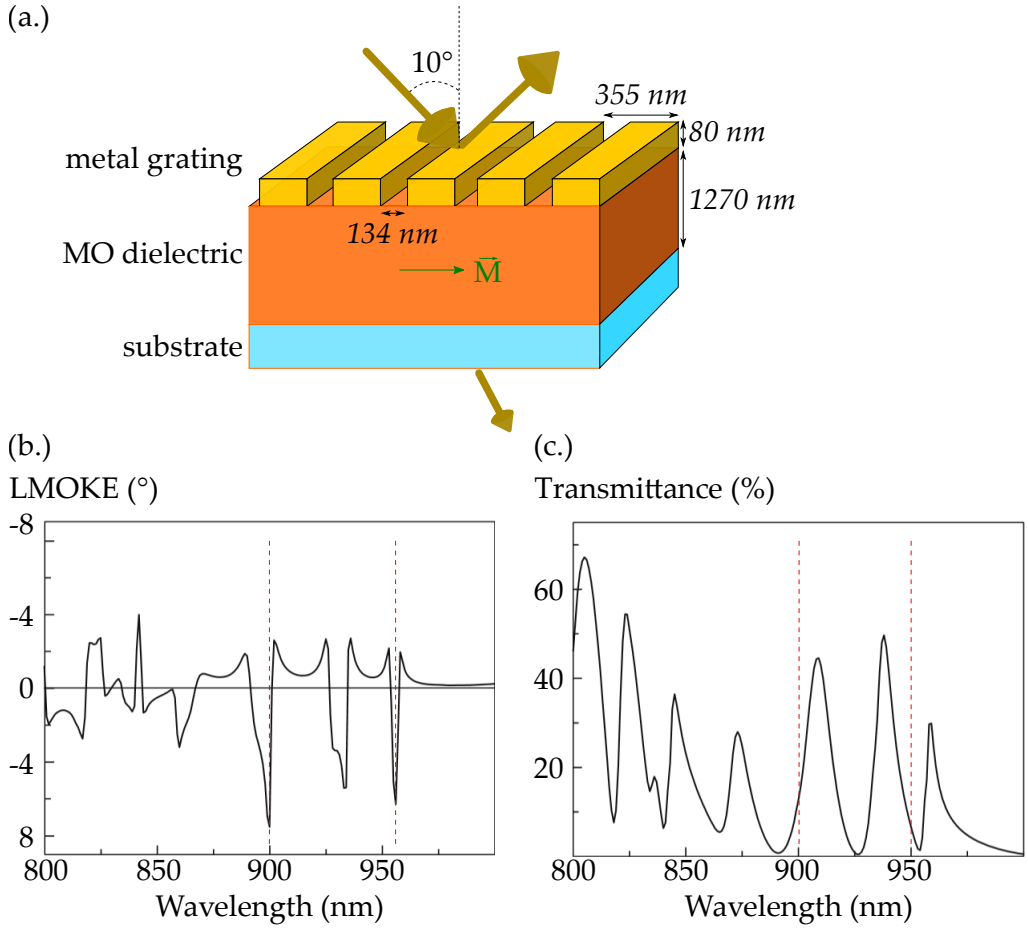

Figure 1.28: (a.) Schematic of 1D magneto-plasmonic structure with longitudinal magnetization. (b.) Corresponding spectra of LMOKE and transmittance (c.). The figure is adapted from [97].

Kalish *et al.* [97] analytically demonstrates a resonant enhancement of LMOKE for a 1-D magneto-plasmonic structure consisting of a MO dielectric magnetized in the plane of incidence with a subwavelength metal grating on top of it, schematically represented in figure 1.28. The calculated LMOKE reaches 8° and 3° for transmitted and reflected light. Excitation of TE waveguide modes in the MO-dielectric is held attributable for the resonant behavior and was found to be absent upon the excitation of plasmon modes. The LMOKE resonances however, do not coincide with the transmission peaks as the excitation of waveguide modes concentrates the EM energy inside the dielectric layer.

1.3.2.c Transverse Magneto-optic effect (TMOKE) enhancement

The TMOKE is an intensity effect observed in TM reflected light when a transverse magnetic field is applied. It is denoted by a parameter δ, which for smooth ferromagnetic materials such as nickel or cobalt is approximatively 10^{-3} and not large enough for device applications [21]. An enhanced TMOKE with high reflectivity can find itself useful in many applications including MO data storage, 3D imaging, magnonics [98] [99]. Its enhancement is usually focused in the light reflected [8] [95] [100] [101] from a magnetized surface but, due to the phenomenon of EOT it can also be enhanced in the light transmitted [12] [102] [92] [23] by a system. Such enhancement is uniquely based on the presence of a TM-spectral resonance. There is no need of phase-matching between TE- and TM-modes. The values of δ close to the TMOKE resonances are proportional to the TM-transmission/reflection derivatives $\left(\frac{dT}{d\lambda}; T = transmission\right)$ [12] [102] [103].

Indeed, the mechanism can be understood by recalling equation 1.35 or 1.32, expressing the propagation constant of a TM-mode in dielectric or plasmonic system. When there is no spontaneous magnetization, a spectrally resonant behavior can be expected in the reflectance (for instance) upon satisfaction of the phase-matching condition. In the presence of a transverse magnetization, the addition of off-diagonal elements in the material's dielectric permittivity tensor induces a modification of the propagation constant, and thus causes a spectral shift of the reflectance curve. Since ϵ_{MO} is an odd function of the magnetization, a reversal in its direction causes a reversal in the propagation constant, which according to the definition of δ results in a resonant enhancement TMOKE as compared to that of a non-resonant system of the same material. Figure 1.29 graphically explains this idea.

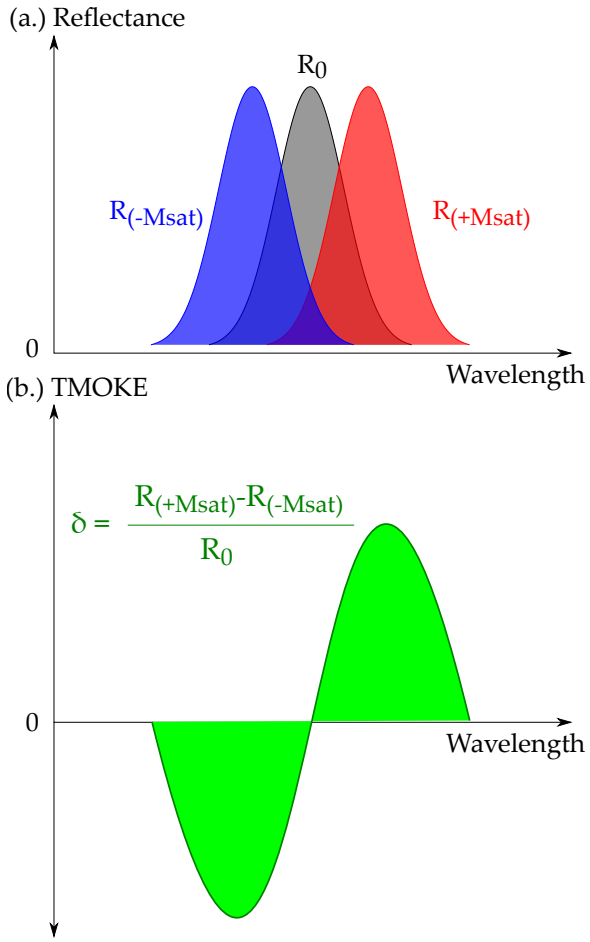

Figure 1.29: (a.) Reflectivity of a resonant system as a function of incident wavelength demonstrating the *odd*-behavior of TMOKE effect. (b.) Spectral dependence of the TMOKE resulting from the reflectivity curves.

Using a 1-D magneto-plasmonic device identical to that given in Figure 1.24, Belotelov *et al.* [12] demonstrated that δ could reach 1.5×10^{-2}. Since Surface Plasmon Polaritons (SPPs) can propagate along both interfaces of a perforated metal film, two SPPs peaks can be observed. However, it is only the metal/MO-dielectric interface that contributes significantly to the TMOKE. It is also demonstrated that in such structures, there is another type of resonance that comes into play namely, *Fabry-Perot cavity resonance* occurring within the slits of the grating which may be potentially responsible for further enhancement of TMOKE [101]. When the two modes i.e. plasmon modes and Fabry-Perot modes couple together, it is the contribution from the SPP modes that give the MO response, while the cavity modes give the dependence on grating parameters such as thickness and air-slit width. It is predicted that by tuning the geometrical parameters of the system,

the coupling efficiency between the two modes can be altered and consequently a geometrical tuning of the TMOKE signal can be achieved. For instance, a sign change of TMOKE (under fixed magnetization) is numerically reported by Halagacka *et al.* [101] by tuning the grating thickness. As illustrated in figure 1.30 which shows

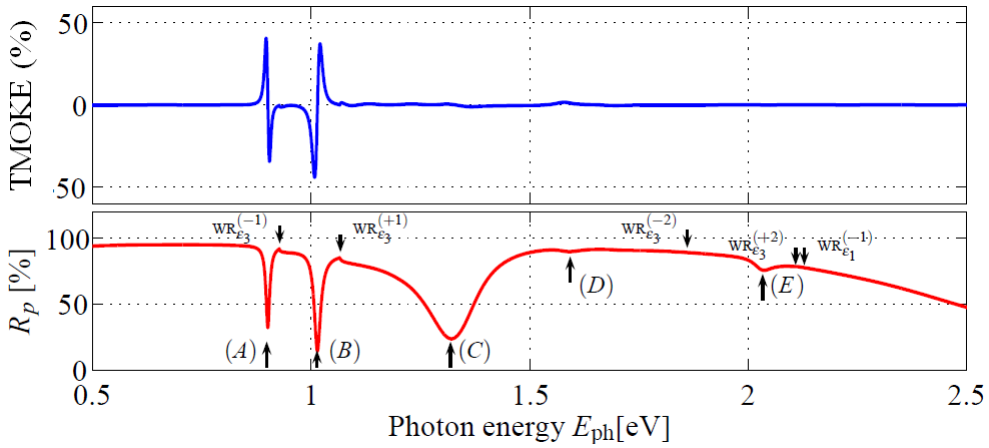

Figure 1.30: TMOKE (top) and reflectivity (bottom) spectrum for a sample consisting of a metal grating on top of a MO substrate illuminated at angle of 10°. The grating parameters are Λ=500 nm, thickness of the grating=150 nm, air-slit width=20 nm. Dips **A** and **B** correspond to the excitation of SPPs whereas, **C**,**D**,**E** correspond to that of Fabry Perot (FP) modes. The figure is adapted from [101].

the specular reflectivity of the grating structure mentioned in [101], one can observe EOT resonances as pronounced dips in the specular reflection close to 1eV and at these positions, giant TMOKE effect is observed ($\delta \approx 0.5$).

Pohl *et al.* [23] experimentally demonstrated an enhancement of TMOKE on a similar magneto-plasmonic structure. It consists of a BIG layer ($5\mu m$ thick) with a 1-D Au grating (100 nm thick with a period of 595 nm and slit width of 85 nm) on it grown on a Gadolinium Galium Garnet (GGG) substrate. They report a TMOKE value as high as 0.085 at 47° incidence for a transmittance of 25% at 885.6 nm. The reason for such a high TMOKE is shown to be at the crossing of the dispersion curves of the SPPs generated on either interface of the metal grating. They explain this coupling in the framework of a coupled oscillator model with each SPP mode at the metal interface (viz. metal/air and metal/MO) being considered as an oscillator with their mutual coupling arising from the finiteness of the grating-thickness and from the grating-slits. Torrado *et al.* [104] [105] experimentally demonstrate in a 2-D structure a resonance in TMOKE at visible wavelengths in oblique incidence of the order of 10^{-4} attributed to the coupling between localized surface plasmons

(plasmons confined in an area of size comparable to or smaller than the exciting wavelength) and propagating surface plasmons (plasmons that propagate along the interface of a metal/dielectric).

However, as for the case of FR enhancement, a "plasmon-less" enhancement of TMOKE is also possible as theoretically demonstrated in [8] [106]. Such an all-dielectric structure was reported to consist of alternating MO and non-magnetic dielectric sections capable of demonstrating a high reflectance and two-orders of magnitude enhancement of the TMOKE response as compared with the continuous film. The schematic structure and the corresponding optical and MO results are presented in figure 1.31. As illustrated, varying the material in the non-MO region

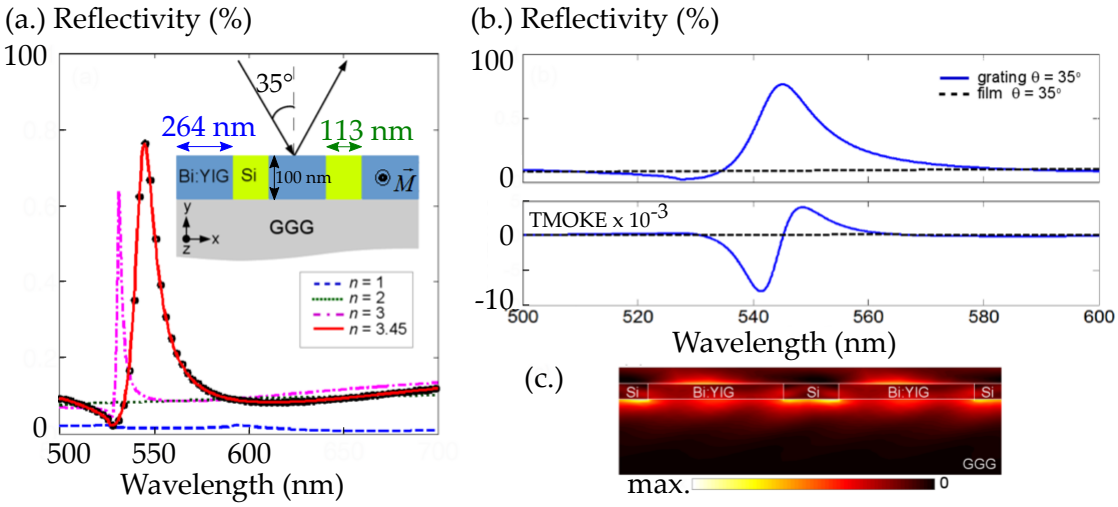

Figure 1.31: (a.)(inset) Schematic of the *all-dielctric* structure reported in [8]. Reflectance as a function of incident wavelength at 35° incidence for different materials in the void. (b.) Optical reflectance with a-Si in the voids and its corresponding TMOKE compared to the non-structured case. (c.) The total intensity profile in the incidence plane corresponding to the maximum intensity. The figure is adapted from [8].

allows the optimization of the reflectance of the structure to as high as 78% and enables a resonant enhancement of TMOKE around the same wavelength. This was possible due to the excitation of guided-modes through phase-matching by the sub-wavelength grating (coupling of the 1^{st} diffraction order in the grating region and its subsequent recoupling back to the incident region). Simulations revealed the existence of a surface wave at the resonant wavelength propagating along the structure (see figure 1.31c). The resonance in such a structure was a function of the incident angle and a further enhancement of TMOKE upto 4×10^{-2} was possible upon decreasing the angle of incidence to 10° compromising on the *Q-factor*. This

TMOKE value is potentially much better than $\delta = 1.5 \times 10^{-2}$ calculated at a transmittance of 3% in [12] and at a transmittance of 45% in [92] using plasmons.

1.3.2.d Longitudinal Magneto-Photonic Intensity Effect (LMPIE) enhancement

Another MO effect involving just the intensity of the transmitted light (TE or TM) is reported by Belotelov *et al.* [107] called Longitudinal Magneto-Photonic Intensity Effect (LMPIE). The structure is shown in figure 1.32.

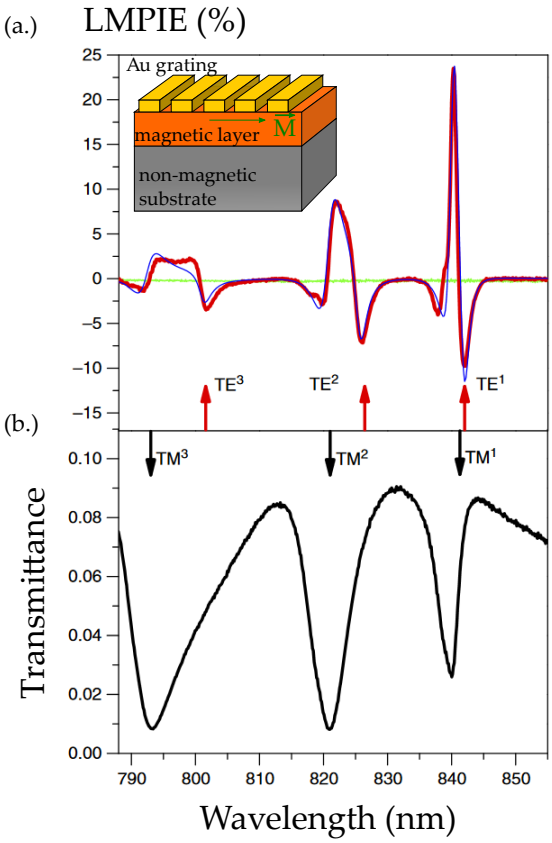

Figure 1.32: (inset) Schematic of the nanostructure consisting a 1.27 μm magnetic layer with a 1-D Au grating of height 67 nm, period 661 nm and space-width of 145 nm. (a.) Measured (red curve) and simulated (blue curve) LMPIE on TM transmittance. The figure is adapted from [107].

When a magnetic field is applied to this structure, the guided-modes in the MO layer transform into "quasi-" guided modes due to its MO nature. This means, for instance, a TM-mode besides having TM-field components also acquires TE components and vice-versa. The excited quasi-mode takes a fraction of the incident

energy by a factor proportional to ϵ_{MO}^2, consequently modifying the transmittance. For the 0^{th} diffraction-order, this effect is described by the relative difference between the transmittance coefficients T_M and T_0 of the magnetized and the demagnetized structure, respectively, and expressed as $\gamma = (T_M - T_0)/T_0$. Figure 1.32(a.) and (b.) show the LMPIE along with 0^{th} order transmitted intensity for the structure, respectively. As expected, no intensity modulation occurs for the bare magnetic film (green). LMPIE for the nanostructure with TM polarized incident light showed longitudinally applied magnetic field resonantly increases the transmittance to 24% at 840 nm (red) in good agreement with simulated results (blue).

1.4 Conclusions and Objectives

The results of the bibliography study focus particularly on the enhancement of various magneto-optical effects using micro-structuration. It is numerically proven and experimentally verified that for an efficient enhancement of polarization rotation, the system should support localization of incident light of both polarizations namely, TE and TM. This could be done by exciting guided-mode resonances using appropriate parameters of the micro-structuration. For Transverse Magneto-Optic Kerr Effect, it is sufficient to excite only TM resonance which is possible either by exciting surface plasmon modes at a metal-dielectric interface or TM- guided-modes of a dielectric waveguide.

The objective of this thesis work is to enhance the magneto-optic response of a magnetic thin film of silica composite containing cobalt ferrite NPs using 1-D periodic structuration. Previously, a photonic-crystal approach had been used to successfully demonstrate a Faraday effect enhancement near the photonic band-gap edge, but the 3-D magneto-photonic crystal of inverse opals was not homogeneous at a macroscopic scale limiting its potential to be integrated with classical circuitry. Consequently, a different approach is required that could lead to a homogeneity on a macro-scale and, simultaneously provides a resonant enhancement of the MO effects.

To achieve this objective, several kinds of 1-D periodic structures containing the MO composite are studied through numerical simulations based on RCWA [108] method. Different materials (dielectric/metal) are tested as templates to be impregnated. For Faraday effect, the idea is to find the optimal parameters to excite simultaneous TE and TM polarized modes in/near the MO material. We saw that

this can be done using plasmons and guided-modes. However, to the best of our knowledge, there is no experimental demonstration of an enhanced Faraday effect by an all-dielectric 1-D device. Having determined the optimal conditions, the structures are then realized using lithography techniques, dip-coated with our MO composite of appropriate NP concentration, characterized optically to determine the excitation of TE/TM resonance at the desired wavelength. Finally, they are magneto-optically characterized to see an enhancement of polarization rotation and TMOKE.

In the next chapter, we will first detail the optical and MO properties of the composite material employed in this work. Furthermore, the equipments used to realize the experimental MO studies will be described.

CHAPTER

2

METHODS: MAGNETO-OPTICAL COMPOSITE MATERIAL, CHARACTERIZATION AND DESIGN TOOLS

The preceding chapter had the focus of explaining the physical processes undertaking in different systems that result in an efficient enhancement of various MO phenomena. Numerous experimental and theoretical studies of MO enhancement were presented in which the material was, in most of the cases, an iron garnet or its derivative. However, there are also various other materials (see table 1.2) that can demonstrate MO behavior with potential applications. One such material is a composite of silica containing magnetic nanoparticles (NPs) of cobalt ferrite. This is the material used for this thesis work. Thus, the first section introduces cobalt ferrite magnetic NPs, with details of its crystal structure, magnetic and magneto-optical properties. It is followed by a section dedicated to the MO composite material. It details the sol-gel process and the way to incorporate NPs in it, the technique of

dip-coating, the optical properties of our composite in terms of refractive index and its ability to impregnate micro-structured templates. The third section deals with a presentation of the experimental setups used for measuring optical and especially, MO properties of the devices. Some MO measurements performed on thin-films of our composite are presented. The last section concerns a short description of the Rigorous Coupled Wave Analysis (RCWA) simulation method employed to study the optical and MO behavior of 1-D gratings.

2.1 Magnetic nanoparticles (NPs) of cobalt ferrite

Nanoparticles (NPs) are materials with at least one dimension typically between 1-100 nm containing from a few hundred to about 10^5 atoms. Magnetic nanoparticles are those materials that respond to a magnetic field. Compared to their bulk counterparts, NPs have an increased surface-to-volume ratio rendering them more complex with unique properties sensitive to their size, shape, and composition of the material. Depending on the intended application, the properties of magnetic NPs can be tuned to suit particular needs. This work being dedicated to cobalt ferrite NPs, we will first focus on the crystal structure of such a material.

2.1.1 Crystal structure

Cobalt ferrite belongs to a class of compounds known as spinel ferrites having the general formula $M^{II}Fe_2^{III}O_4$ [109], where M^{II} represents a divalent metal cation and Fe^{III} a trivalent iron cation. The crystal structure of cobalt ferrite is the same as that of the mineral spinel ($MgAl_2O_4$) [110] [111]. The unit cell of the spinel ferrites is formed by 8 $M^{II}Fe_2^{III}O_4$ molecules with 56 ions; 32 oxygen anions in a face-centered-cubic (fcc) packing and 24 cations occupying 8 of the 64 available tetrahedral sites (A) and 16 of the 32 available octahedral sites (B). Figure 2.1 represents the primitive unit cell of spinel ferrites consisting of two $M^{II}Fe_2^{III}O_4$ units in two octants. However, the ionic positions repeat along the shaded patterns in the other octants.

$CoFe_2O_4$, in particular, has an inverse spinel structure [112] in which 8 Co^{2+} cations predominantly occupy 8 octahedral sites and the 16 Fe^{3+} cations are distributed between 8 tetrahedral and 8 octahedral sites. Its structural formula can be

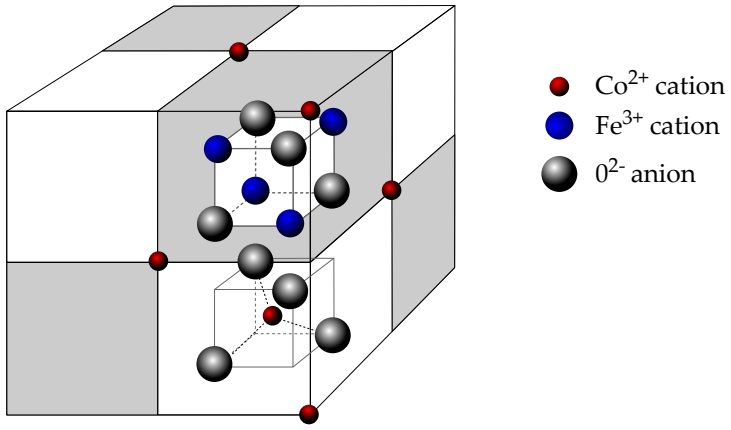

Figure 2.1: Ionic distribution for the primitive unit cell of spinel ferrites.

written as:

$$[\mathrm{Fe}]^{\mathrm{A}}[\mathrm{CoFe}]^{\mathrm{B}}\mathrm{O}_4$$

Cobalt ferrite is a promising candidate for high-density recording media [113] due to large magneto-crystalline anisotropy, good saturation magnetization, chemical stability and hardness. Other uses of cobalt ferrite include catalysis [114], drug delivery and hyperthermia [115].

2.1.2 Magnetic properties

The magnetic properties of cobalt ferrite is due to both Co^{2+} and Fe^{3+} cations which bear individual magnetic moments. Anti-ferromagnetic super-exchange interaction through 0^{2-} anions and ferromagnetic double exchange interaction between magnetic cations result in a ferrimagnetic spontaneous magnetization [116]. Magnetic behavior in such materials can be understood in terms of special regions inside them where the individual magnetic moments of constituent entities all point in the same direction viz. *magnetic domains*. But, when the crystal is small enough it is energetically more favorable to exist as a single-domain particle rather than having multiple domains. Thus, cobalt ferrite NPs are mono-domain and possess a magnetic moment $\vec{\mu}$ whose magnitude depends on its volume by the relation: $|\vec{\mu}| = m_s V$; m_s being the saturated magnetization of cobalt ferrite ($= 4.2 \times 10^5 \mathrm{Am}^{-1}$) [116].

When a magnetic material shows directional dependence of its magnetic moment vector, it is said to be *magnetically anisotropic*. It can be of the following types: magneto-crystalline anisotropy, shape anisotropy, surface anisotropy and strain anisotropy. The net magnetic anisotropy is a complex mix of them, but we shall restrict

ourselves only with magneto-crystalline anisotropy, as it is the dominant one in case of cobalt ferrite NPs used in this work.

Magneto-crystalline anisotropy is that property of a magnetic material which results in certain directions more favorable than the rest. When an electron's orbital motion interacts with its spin motion, it makes the latter prefer to align along certain well-defined crystallographic axes. Consequently, the magnetic material becomes easier to magnetize parallel to these specific directions than others. These directions which are energetically most favorable are called *easy*-directions or *easy*-axis whereas, those least favorable are called *hard*-directions or *hard*-axis.

Considering a uniaxially-anisotropic crystal, with its magnetization vector making an angle θ with the easy-axis, its anisotropy energy is expressed as:

$$E = KVsin^2\theta \tag{2.1}$$

where K is a temperature-dependent anisotropy constant, V is the volume and θ is the angle between the magnetization and the easy-axis. According to equation 2.1, the magneto-crystalline anisotropy for a single-domain NP describes two local energy minima at $\theta = 0$ and $\theta = \pi$ separated by an energy barrier KV (refer figure 2.2).

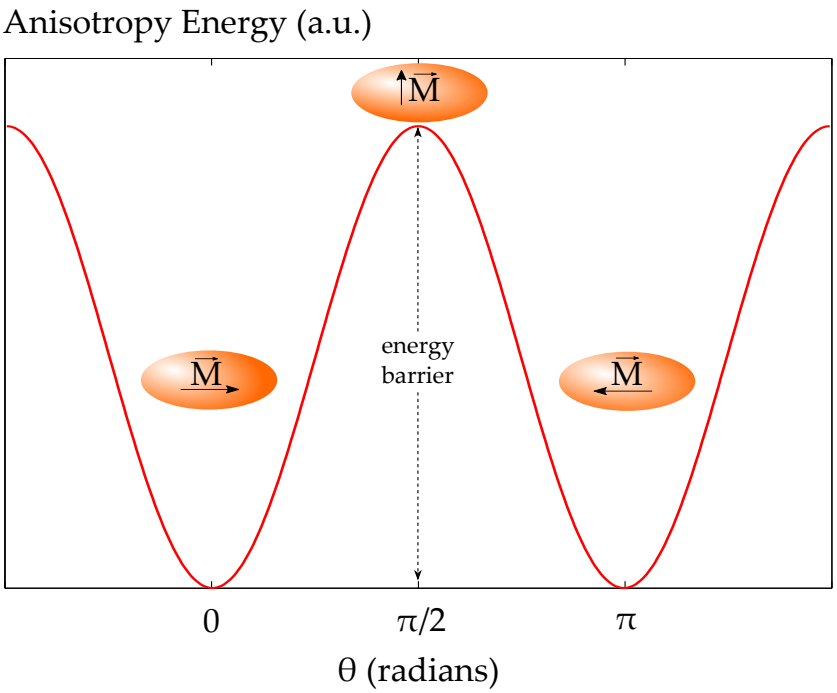

Figure 2.2: Energy of a single-domain NP as a function of the angle θ between its magnetization vector and easy-axis.

For small enough single-domain magnetic NPs, KV can become so small that thermal fluctuations can overcome the energy barrier and spontaneously reverse their magnetization from one easy direction to the other, even in the absence of a magnetic field. This is called *isotropic* superparamagnetism. When the temperature in lowered, the dynamics of the NP change. For $k_BT \approx KV$, (k_B: Boltzmann constant), we obtain *anisotropic* superparamagnetism, wherein the particle still has the thermal energy to overcome the energy barrier but undergoes a hindered rotation due to finite size of the barrier. In such a case, the direction of magnetization fluctuates between the two energy minima with a frequency f or a characteristic relaxation time, $2\pi f^{-1}$. It is expressed as the Néel-Brown expression [117]:

$$\tau = \tau_0 e^{KV/k_BT} \tag{2.2}$$

where τ_0 is the inverse attempt frequency, typically in the range 10^{-12} to 10^{-9} sec [118]. It is evident from the above equations that as the temperature of the system lowers, magnetization fluctuations slow down. Depending on the time scale of experiment τ_m, two following situations are possible:

$\tau_m << \tau$**:** The magnetization appears static as the average time between flips is much larger than the measurement time which puts the system in a well-defined state of magnetization, called the *blocked* state.

$\tau_m >> \tau$**:** The second situation implies that the measurement time is so large that one observes a fluctuating state of un-resolved magnetization direction resulting in a time-average net magnetic moment of zero, called the *super-paramagnetic* state of the system.

For cobalt ferrite at room temperature and assuming a measurement time of 60s, the limit diameter between the two situations is 7.3 nm [119]. The mean diameter of the NP assembly used in this work in 10 nm with a standard deviation of about 0.3. Thus, both behaviors (blocked and super-paramagnetic) exist simultaneously.

2.1.3 Spectral behavior of MO Faraday effect

Energy transitions

Since an electron carries an electrical charge, its motion and rotation results in a net magnetic moment. According to atomic theory, the orbital angular momentum of

electrons is quantized which means that the atomic dipole moments are restricted to certain particular values and orientations with respect to an external field. This has important effects on the magnetic properties of materials. The dynamics of electrons require three quantum numbers n, l, m_l labeled as the principal quantum number, angular momentum quantum number, and magnetic quantum number respectively, to describe the orbitals in which electrons exist. Their values are restricted to:

$$\begin{aligned} n &= 1, 2, 3... \\ l &= 0, 1, 2, 3.....(n-1) \\ m_l &= -l, (-l+1)...(l-1), l \end{aligned} \tag{2.3}$$

The principal quantum number n determines the atomic orbital size and the energy of an electron level. A level with $n = 1$ has the lowest energy, and is called the *ground state*. An electron needs to gain energy for it to reach higher energy levels, called *excited states*. This energy can be imparted, for instance, by an impinging photon. The principal quantum number directly does not determine any material magnetic properties, but it influences the values of l and m_l which can be permitted. The angular momentum quantum number l determines shape of the atomic orbitals and also the magnitude of the orbital angular momentum $|\mathbf{L}|$ of an individual electron which is expressed as:

$$|\mathbf{L}| = \sqrt{l(l+1)}h \tag{2.4}$$

where h is the Planck's constant. Values of $l = 0, 1, 2, 3, ...$ correspond to s, p, d, f atomic orbitals, respectively. It is clear that for s-orbitals ($l = 0$), $|\mathbf{L}| = 0$ and so, electrons in s-orbitals make no contribution to the atomic magnetic moment from their orbital angular momentum. However, for p-orbital electrons ($l = 1$) resulting in an orbital angular momentum of magnitude $\sqrt{2}\hbar$ ($\hbar$: reduced Planck's constant) and m_l values of -1, 0 or +1. Since the magnetic quantum number m_l determines the orientation of atomic orbitals, quantized values of m_l translates to the understanding that p-orbitals can exist with three different orientations relative to an externally applied magnetic field. For an electron revolving around its nucleus in an externally applied magnetic field, it energy can be expressed as:

$$E = \mu_0.\mu_b.m_l.H \tag{2.5}$$

where μ_b is the elementary unit of magnetic moment of an atom called the Bohr magneton. Hence, due to the magnetic field, the energy of an electron in an atomic

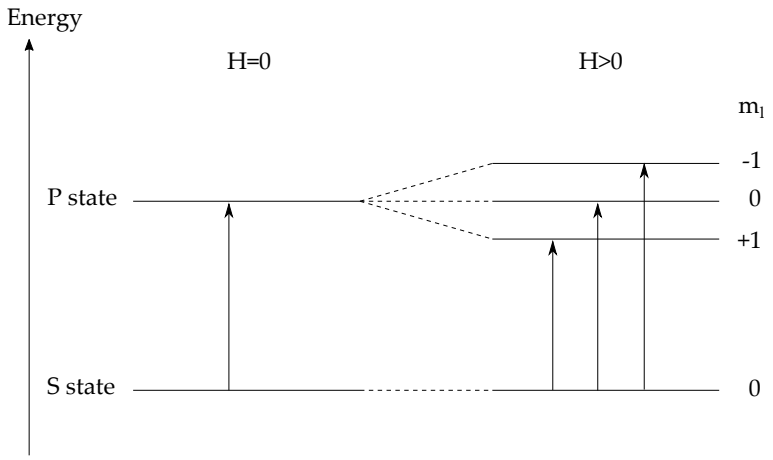

Figure 2.3: Zeeman effect.

orbital with non-zero orbital angular momentum changes by an amount proportional to the orbital angular momentum of the orbital and the applied field. This phenomenon is called the Zeeman effect. Figure 2.3 shows an example of a Zeeman splitting of a transition between an s-orbital and a p-orbital of an atom. In the absence of an external magnetic field, both the orbitals have one energy level each. However, when the magnetic field in non-zero, the energy level of p-orbital electrons splits into three energy levels corresponding to m_l values of -1, 0 and 1. The energy level of s-orbital electrons do not split in this case because, as mentioned above, the s-electrons do not have an orbital angular momentum and therefore no orbital magnetic moment.

In addition to these three quantum numbers, there are two other quantum numbers arising from the spin of an electron about its axis. The first of them is called the spin quantum number, s and has the value 1/2 always. The magnitude of the spin angular momentum of an individual electron is given by:

$$|\mathbf{S}| = \sqrt{s(s+1)}\hbar \tag{2.6}$$

The second quantum number m_s is spin analog of the magnetic quantum number, m_l. Its values are quantized to be $+1/2$ and $-1/2$ with respect to an external magnetic field. The interaction of the magnetic moments due to electron's orbital motion and its spin motion is called spin orbit coupling and is behind the polarization rotation observed in Faraday and Kerr effects. When a linearly polarized light is incident on a magnetic material subject to an external magnetic field, first, the light is decomposed into its two proper modes: RCP and LCP light. Each circular polarization has

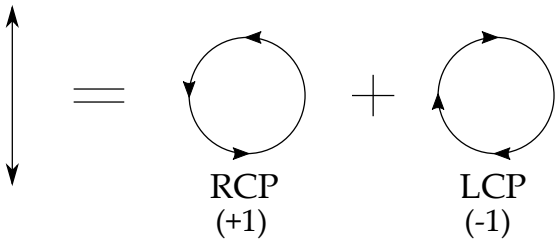

Figure 2.4: Decomposition of a linearly polarized light ray into its circularly polarized components with corresponding values of angular momentum.

photons with the same magnitude of angular momentum but mutually opposite directions i.e. angular momentum of RCP light and LCP light are +1 and -1, respectively.

Second, when an energy level Zeeman-splits in the presence of an external magnetic field, conservation of energy and angular momentum demands that for a photon to excite an electron from a ground state to an excited states, the following selection rule for orbital angular momentum term L and spin angular momentum S be applicable:

$$\begin{aligned} \Delta S &= 0 \\ \Delta L &= \pm 1 \end{aligned} \tag{2.7}$$

Equation 2.7 signifies that first, intrastate transitions are not allowed but only interstate transitions. Second, $\Delta L = \pm 1$ mandates oppositely polarized photons to correspond to different electronic transitions in the atom (see figure 2.7). Consequently, the electron system becomes able to distinguish between the two circular modes now.

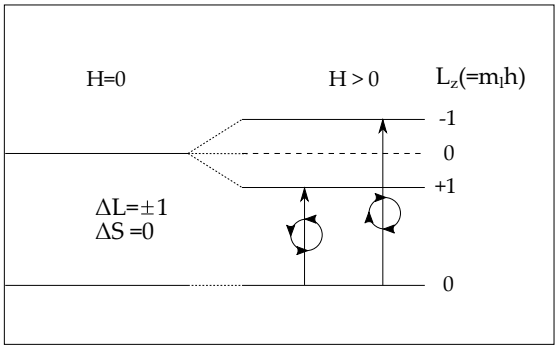

Figure 2.5: Electronic transitions due to incident photons discriminating the two circular modes.

Electric dipole transitions

This lifting of degeneracy of energy states gives rise to the optical circular anisotropy in the form of non-zero off-diagonal elements in the dielectric permittivity tensor which is expressed as:

$$\epsilon_{MO} = \left(\frac{2\pi N e^2}{m}\right) \times \sum_{e,u} \left[\frac{f_{-e(u)} - f_{+e(u)}}{\omega^2 - \omega_{e(u)}^2 - \Gamma_{e(u)}^2 - 2i\omega\Gamma_{e(u)}}\right] \times \left(\frac{\omega - i\Gamma_{e(u)}}{\omega_{e(u)}}\right) \tag{2.8}$$

where $f_{\pm e(u)}$ are the oscillator strengths for transitions caused by the LCP and RCP light, respectively, $\omega_{e(u)}$ is the resonance frequency, and $\Gamma_{e(u)}$ is the half-width at half-maximum of the optical transitions between the ground state $|g\rangle$ and excited state $|e(u)\rangle$ where u indexes the orbital degeneracy.

In the absence of an external field, $\omega_{e(u)}$ and $\Gamma_{e(u)}$ are independent of u, and since the sum over the oscillator strengths, $\sum_v f_{\pm e(u)}$ are identical, we get $\epsilon_{MO} = 0$ from equation 2.8. Two cases are presented below where it is shown how spin-orbit interaction can result in linear MO effects (non-zero values of ϵ_{MO}).

Case 1: Dominance of excited state splitting: In this case, contribution to the off-diagonal terms is dominated by the energy gap between the excited states. As a result, an energy splitting between the transition energies of RCP and LCP arises, while the oscillator strengths for them becomes equal. An extremum in $\mathrm{Re}\{\epsilon_{MO}\}$ and an oscillation in $\mathrm{Im}\{\epsilon_{MO}\}$, corresponding to respectively, dissipative and dispersive behavior is observed. This is called the *diamagnetic* line shape. Figure 2.6(a.) shows the diamagnetic transitions for excitation from a low-energy singlet state to a high-energy multiplet state and figure 2.6(b.) shows the spectral behavior of the complex off-diagonal term (Faraday rotation and ellipticity) of the permittivity tensor due to diamagnetic transitions in cobalt ferrite. Faraday rotation presents two maxima of opposite sign centered at a wavelength where the ellipticity presents a maximum.

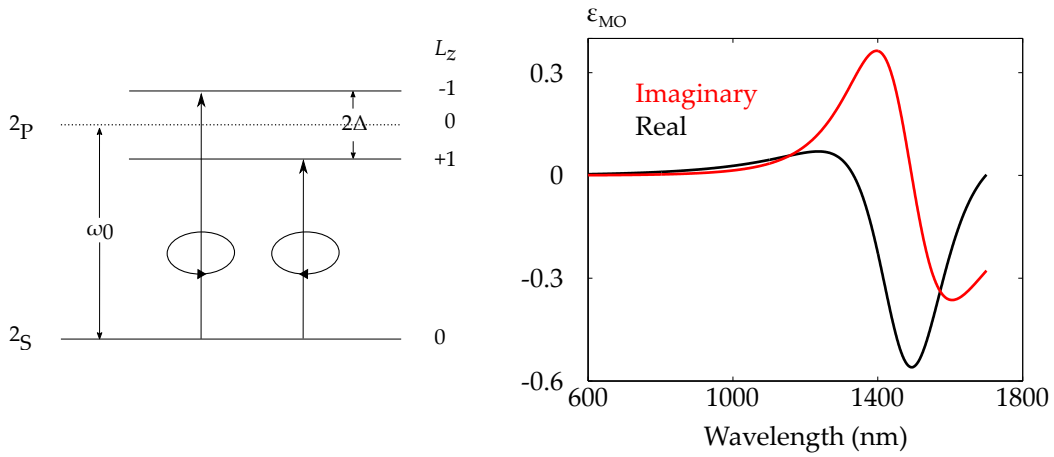

Figure 2.6: Diamagnetic transition.

The transition is described by the following equation:

$$\epsilon_{MO} = -\Gamma_0^2 \big[\,\mathrm{Re}(\epsilon_{MO})\big]_{max} \times \left[\frac{(\omega-\omega_0)^2 - \Gamma_0^2 + 2i\Gamma_0(\omega-\omega_0)}{\big[(\omega-\omega_0)^2 + \Gamma_0^2\big]^2}\right] \tag{2.9}$$

where ω_0 and Γ_0 denote the resonance frequency and half-width-at-half-maximum for the particular transition.

Case 2: Dominance of oscillator strength difference: In the case when contribution to ϵ_{MO} is dominated by a difference between the oscillator strengths, $f_{+e(u)}$ and $f_{-e(u)}$ which can be caused by a difference in ground-state population of the levels of a spin-orbit-split ground state, for example, we observe an oscillation in $\mathrm{Re}\{\epsilon_{MO}\}$ and an extremum in $\mathrm{Im}\{\epsilon_{MO}\}$. This is called the *paramagnetic* line shape.

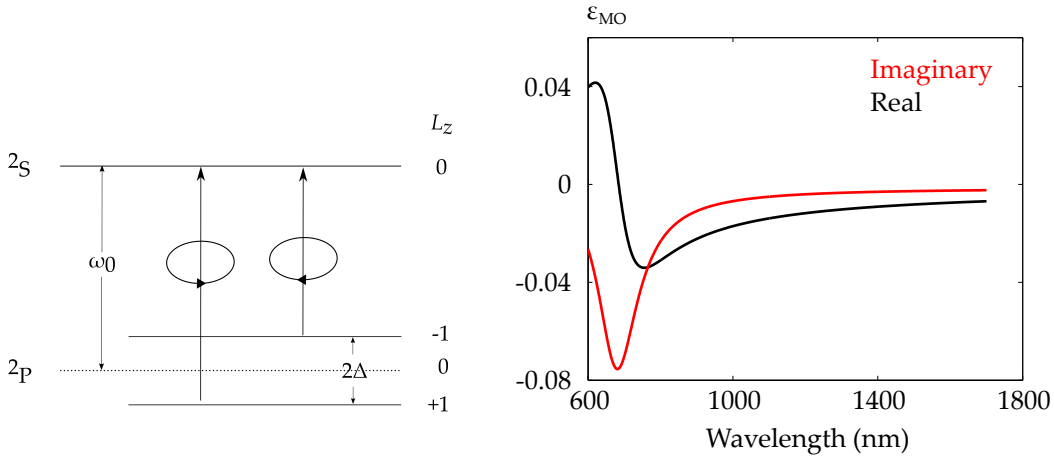

Figure 2.7: Paramagnetic transition.

The transition is described as follows:

$$\epsilon_{MO} = -2\Gamma_0^2 \big[\,\mathrm{Im}(\epsilon_{MO})\big]_{max} \times \left[\frac{\omega(\omega^2 - \omega_0^2 + \Gamma_0^2)^2 - i\Gamma_0(\omega^2 + \omega_0^2 + \Gamma_0^2)}{\big[(\omega^2 - \omega_0^2 + \Gamma_0^2)^2 + 4\Gamma_0^2\omega^2\big]^2}\right] \tag{2.10}$$

Fontijn *et al.* [120] have listed the main MO-active electric-dipole transitions in cobalt ferrite between 0.5 and 5eV. Table 2.1 gather the ones useful for our wavelength range of study.

Transition energy (eV)	0.83	1.82	2.21
Corresponding wavelength (nm)	1494	681	561
$\big[\,\mathrm{Im}(\epsilon_{MO})\big]_{\mathbf{max}}$	-0.056	-0.076	-0.054
Assignment	electron transition in tetrahedrally coordinated Co^{2+}	electron transition in tetrahedrally coordinated Co^{2+}	electron transition between $[Co^{2+}]$ and $[Fe^{3+}]$ at octahedral sites
Line shape	diamag	para	para

Table 2.1: Table listing the main MO-active energy transitions in $CoFe_2O_4$ the wavelength range used in this study. The list is derived from [120].

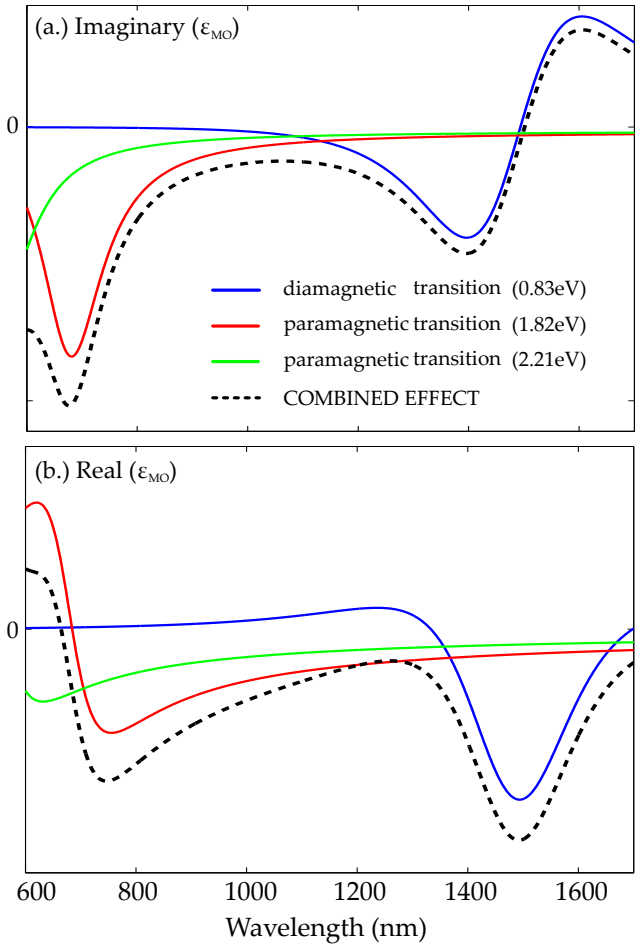

Figure 2.8: Different electronic transitions in cobalt ferrite and its impact on the real (a.) and imaginary (b.) parts of the permittivity tensor.

From these numerical values, the spectral behavior of the whole off-diagonal permittivity element ϵ_{MO} has been plotted in figure 2.8 (a.) and (b.), together with that of each individual transitions. As explained in the previous chapter, the Faraday rotation in linked to the real part of this element (equation 1.11),whereas the Faraday ellipticity is linked to the imaginary part (equation 1.12). Thus, from these graphs, the ellipticity is expected to have a maximum in the visible region and two local maxima of opposite signs in the NIR region. Similarly, from figure (b.) the polarization rotation is expected to have two local maxima of opposite signs in the visible region and a local maxima in the NIR region (around 1550 nm). This is in full accordance with the Faraday rotation spectrum presented previously in figure 1.4. Such spectral behavior is to be modified through the existence of a resonant effect. For analysis of the enhanced effect in the following chapter, this spectrum

will always be used as reference.

2.1.4 Magnetic field dependence of Faraday effect

In the previous section, it has been shown that the lifting of the degeneracy of RCP and LCP electronic transitions, which gives rise to the polarization rotation, is due to the magnetic state of the ions. More precisely, it is the longitudinal magnetization which induces such a circular birefringence between RCP and LCP. It means that the off-diagonal element ϵ_{MO} is proportional to the magnetization of the material. In the previous chapter (refer equation 1.11 and equation 1.12), the Faraday effect has been expressed as:

$$\theta_F = \frac{\pi.l.\epsilon_{MO}}{\lambda.n} \tag{2.11}$$

n being the refractive-index, l and λ representing the length of the material and incident wavelength of light, respectively. Thus, the dependence of Faraday effect is expected directly proportional to the magnetization i.e.

$$\theta_F \propto \epsilon_{MO} \propto M_{int} \tag{2.12}$$

Cobalt ferrite NPs being ferrimagnetic and single-domained, their MO activity depends on the orientation of their magnetic moments. This orientation is achieved through the application of an external magnetic field and results as the magnetization. Two cases have to be considered:

Case 1: NPs in a liquid medium: When magnetic NPs are colloidally suspended in a suitable carrying liquid medium, the system is called a *ferrofluid*. Ferrofluids typically contain particles quasi-spheric in shape with a diameter typically in the range of 5-20 nm [121].

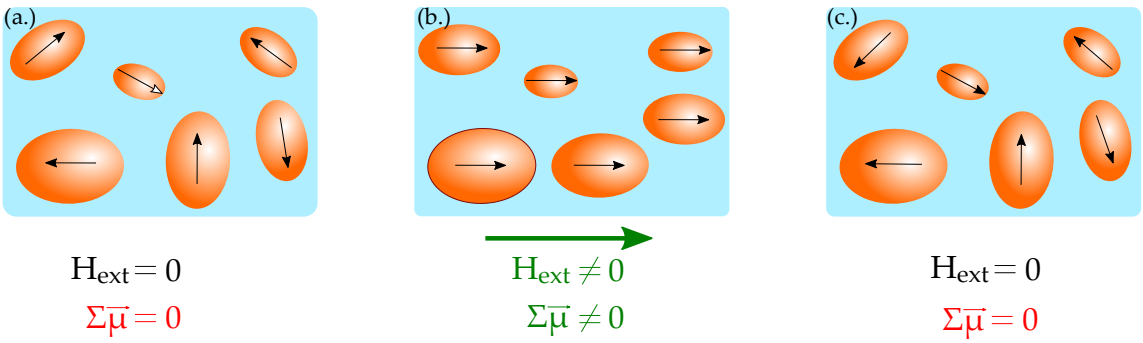

Figure 2.9: Orientation of magnetic moments in single-domain NPs suspended in a liquid with (b.) and without (a. and c.) an external magnetic field.

In the absence of an external magnetic field and at room temperature, the magnetic moments $\vec{\mu_i}$ of the NPs, being randomly oriented, cancel out each other resulting in "zero" net magnetization ($\Sigma\vec{\mu}$) of the ferrofluid (figure 2.9 (a.) and (c.)). However, when it is subjected to an external magnetic field, for instance in the z-direction, each individual moment tends to align, through the rotation of the whole particle, along this field causing a magnetization of the ferrofluid (figure 2.9 (b.)).

For magnetic moments making an angle θ with the external field along z-direction, the magnetization is expressed as:

$$\begin{aligned} M_z &= \frac{\sum \vec{\mu} \cdot \hat{z}}{V} \\ &= \frac{n}{V} \frac{\int_0^\pi \mu \cos(\theta) \exp\left(\frac{-\mu \cos(\theta) H}{k_B T}\right) \sin(\theta) d\theta}{\int_0^\pi \exp\left(\frac{-\mu \cos(\theta) H}{k_B T}\right) \sin(\theta) d\theta} \quad = m_s.\phi.L(x) \end{aligned} \tag{2.13}$$

where, $L(x)$ is the first Langevin's function and expressed as:

$$L(x) = coth(x) - \frac{1}{x}$$

with

$$x = \frac{\mu H}{k_B T} = \frac{m_s V H}{k_B T} = \frac{\pi D^3}{6} \frac{m_s H}{k_B T}$$

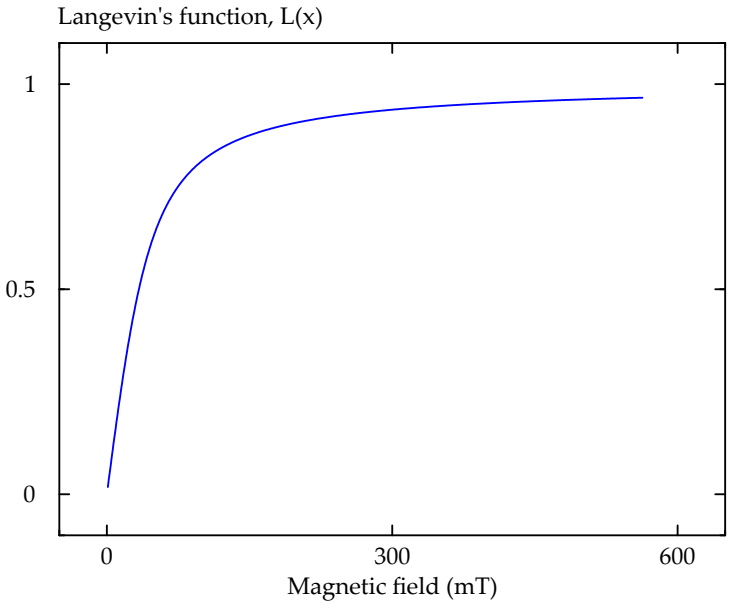

Figure 2.10: Langevin's function.

- For large values of H: $L(x) \to 1$ and,

$$M_z = m_s \phi$$

i.e the magnetization due to the external field asymptotically tends to a saturation (see figure 2.10).

- For small values of H: $L(x) \propto H$,

$$M_z \propto H$$

i.e. the magnetization is linear in nature to the external field.

Figure 2.10 show this dependence for NP diameter D=10 nm, saturation magnetization m_s=422 kAm^{-1}.

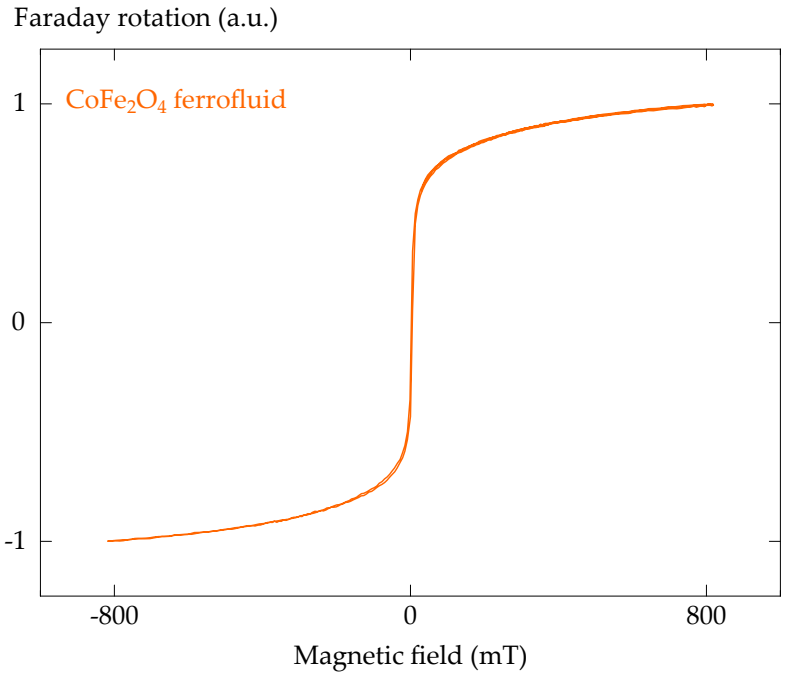

Figure 2.11: Magnetization of cobalt ferrite NPs in a liquid medium showing no remanence and coercivity.

Figure 2.11 experimentally shows this behavior for a ferrofluid. Recalling equation 1.11, the Faraday rotation for a linearly polarized light traveling through an optically anisotropic material is expressed as:

$$\theta_F = \left(\frac{\pi}{\lambda}\right) \mathrm{Re}\left[\frac{\epsilon_{MO}}{\sqrt{\epsilon_{xx}}}\right] l$$

with

$$\epsilon_{MO} \propto \phi L(x)$$

Hence, expression for Faraday rotation is expressed as:

$$\theta_F \propto \left(\frac{\pi}{\lambda}\right)\left[\frac{\phi L(x)}{\sqrt{\epsilon_{xx}}}\right] l \tag{2.14}$$

Case 2: **NPs trapped in a matrix**: In contrast to the above case in which upon removing the external field individual moments return back to their random alignment position due to Brownian movement of the particles, particles trapped in a matrix do not have the freedom to move about. Hence, the magnetization process is a competition between several effects:

- the thermal energy which tends to produce a random orientation,
- the Zeeman energy ($\vec{\mu}.\vec{H}$) which tends to align the moment in the applied field direction and,
- the anisotropy energy(KV) which retains the moment in the direction of the easy-axis.

Thus, there still remains a small net magnetization in the system when the external magnetic field is removed (see figure 2.13(c.)), called remanent magnetization which, in accordance with relation 2.12, leads to a remanent rotation or remanence. To make the magnetization zero an external field in the opposite direction is required, termed as coercive field or coercivity. This phenomenon is known as hysteresis. Figure 2.12 demonstrates this behavior for the system used throughout this thesis viz. $CoFe_2O_4$ NPs trapped embedded in a silica matrix.

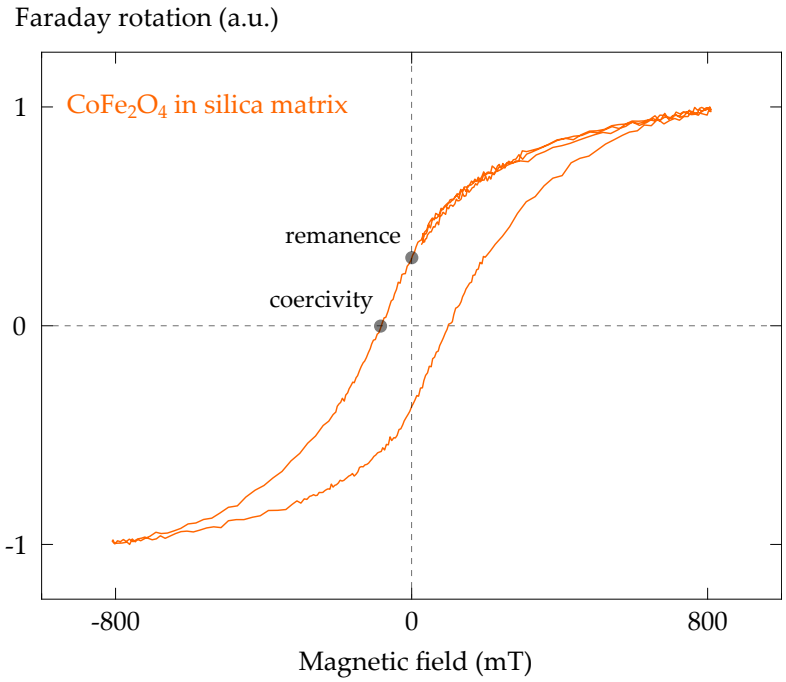

Figure 2.12: Faraday rotation of cobalt ferrite NPs embedded in a silica host matrix showing non-zero values of remanence and coercivity.

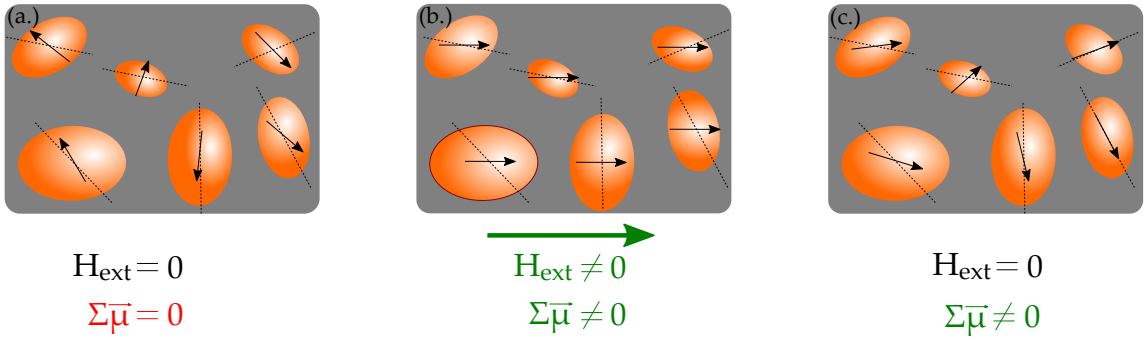

Figure 2.13: Orientation of magnetic moments in single-domain NPs trapped in matrix with (b.) and without (a. and c.) an external magnetic field.

Effect of NP concentration: When the concentration of magnetic NPs increases, the resulting MO effect also increase accordingly. Figure 2.14(a.) and (b.) demonstrates this for MO Faraday effect with varied concentrations (ϕ) of $CoFe_2O_4$ NPs.

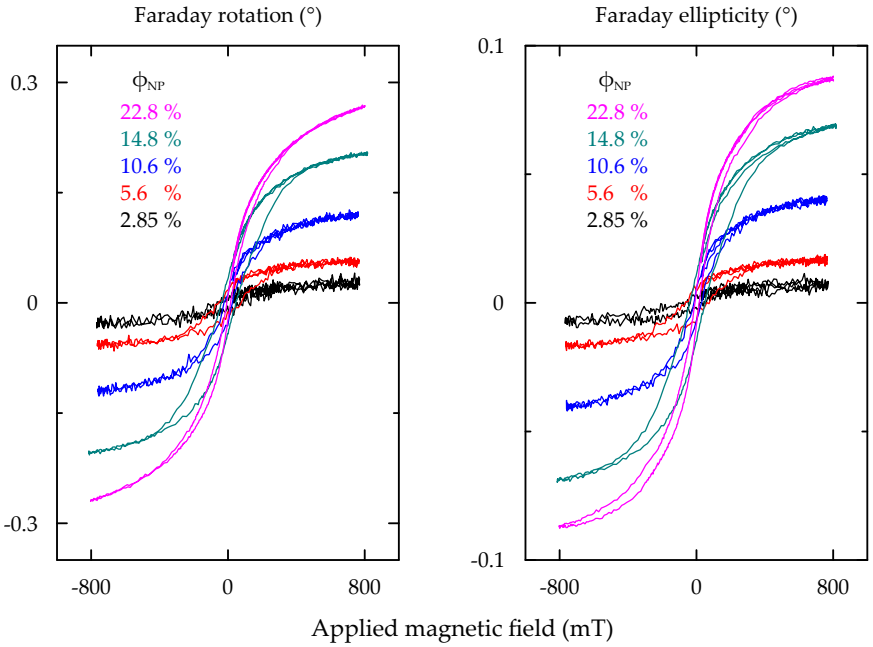

Figure 2.14: Faraday rotation and ellipticity for different concentrations (ϕ) of cobalt ferrite NPs in a silica matrix.

Table 2.2 extracts the values from figure 2.14 and demonstrates how increased concentration of NPs in the system results in an increased MO effect.

Concentration (%)	Faraday rotation (°)	Faraday ellipticity (°)
2.85	0.03	0.008
5.6	0.06	0.02
10.6	0.12	0.04
14.8	0.2	0.07
22	0.27	0.09

Table 2.2: Effect of increased concentration of $CoFe_2O_4$ NPs on Faraday rotation and Faraday ellipticity.

The process of incorporation of the $CoFe_2O_4$ NPs from ferrofluid form into the

silica host matrix and its subsequent fabrication in thin-film form is the focus of the next section.

2.2 Thin-films of MO composite

Figure 2.15 shows the major steps required for the fabrication of thin-films of MO composite:

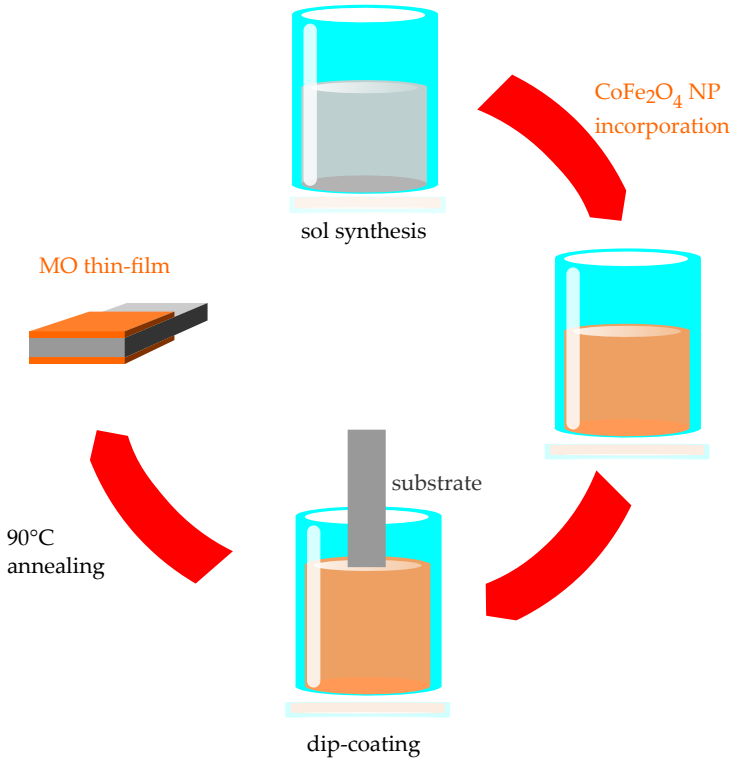

Figure 2.15: Schematic presentation of the series of steps utilized to prepare MO thin films.

The following sub-sections explain these steps one-by-one:

2.2.1 Sol-gel technique

A sol is a suspension of dispersed particles in a liquid and when these particles aggregate together to form a highly cross-linked, rigid and stable network that spans the entire volume of the liquid, the result is called a gel structure (see figure 2.16). It is this formation of a gel from a sol that renders this technique the name "sol-gel" technique [122] [123].

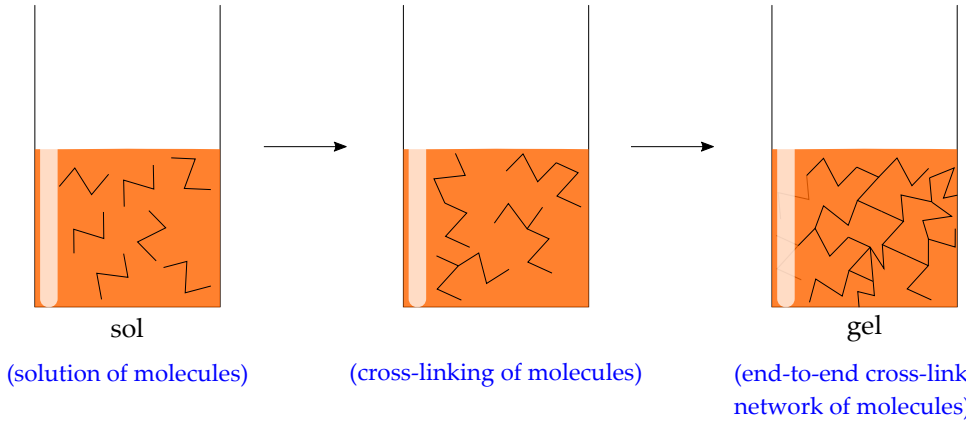

Figure 2.16: Sol to gel transition.

The synthesis of a sol-gel starts with a metal-organic precursor usually a metal alkoxide of the form $M(OC_2H_{2x-1})_n$. The host matrix of the MO composite is a silica sol-gel and so the precursor used is TetraEthylOrthoSilicate (TEOS), $Si(OC_2H_5)_4$ [122] (see figure 2.17). The interest in using TEOS is the siloxane bonds Si-O-Si that form the backbone of the resultant gel structure (breaking temperature of this bond is 1200 $°C$).

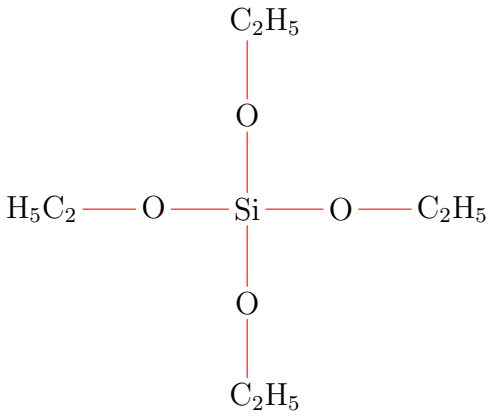

Figure 2.17: Chemical structure of TetraEthylOrthoSilicate (TEOS)

The next step is hydrolysis which involves the replacement of the ethoxy group with a hydroxyl group and release of corresponding alcohol.

$$Si(OC_2H_5)_4 \quad + \quad xH_2O \quad \longrightarrow \quad HO - Si(OC_2H_5)_3 \quad + \quad ROH$$

Complete hydrolysis occurs when the stoichiometric molar ratio of water:TEOS is 4, otherwise partial hydrolysis occurs [122]. The sol–gel chemistry of silica is typically

driven by either acid or base catalysts as the neutral reaction is very slow. The structure of the resulting gel is significantly different depending on the catalyst and this is due to the relative rates of the hydrolysis and condensation reactions. Condensation involves the removal of H_2O from the silane groups (Si-OH) to get siloxane (Si-O-Si) bonds.

$$Si(C_2H_5O)_3OH \quad + \quad Si(C_2H_5O)_3OH \longrightarrow (C_2H_5O)_3Si - O - Si(C_2H_5O)_3 \quad + \quad H_2O$$

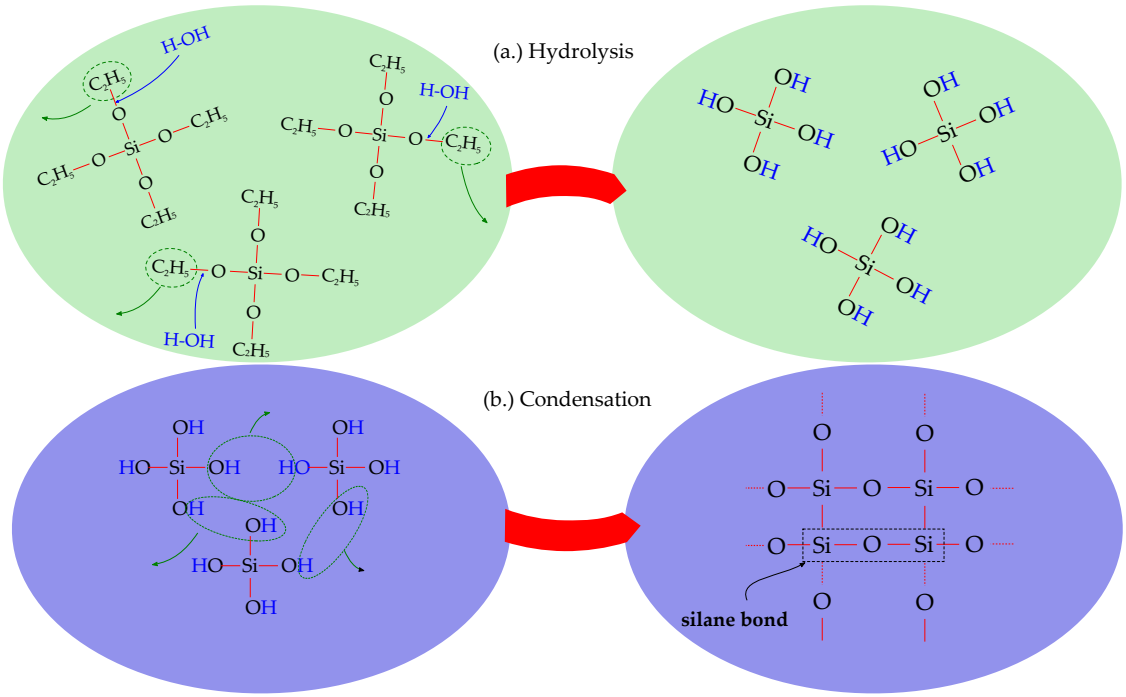

Figure 2.18: Mechanism of silane-bond formation during sol-gel process.

Gelation of sol-gel: Gelation is the phenomenon where cross-linking polymers undergo a phase-transition from a liquid-state to a solid-state after reaching a certain time period [124]. This transition from "sol" phase to "gel" phase occurs when one of the molecules of the cross-linking polymer grows so large that its size reaches the dimensions of the macroscopic sample. To follow this evolution, the sol is subjected to a shear flow and its viscosity is measured with respect to reaction time. Once it transforms into gel, the material is subjected to strain and its elastic constant is measured with respect to reaction time ([124] and references therein). Figure 2.19 illustrates the results; in sol-phase the viscosity diverges, and in gel-phase the elastic constant saturates with extent of reaction.

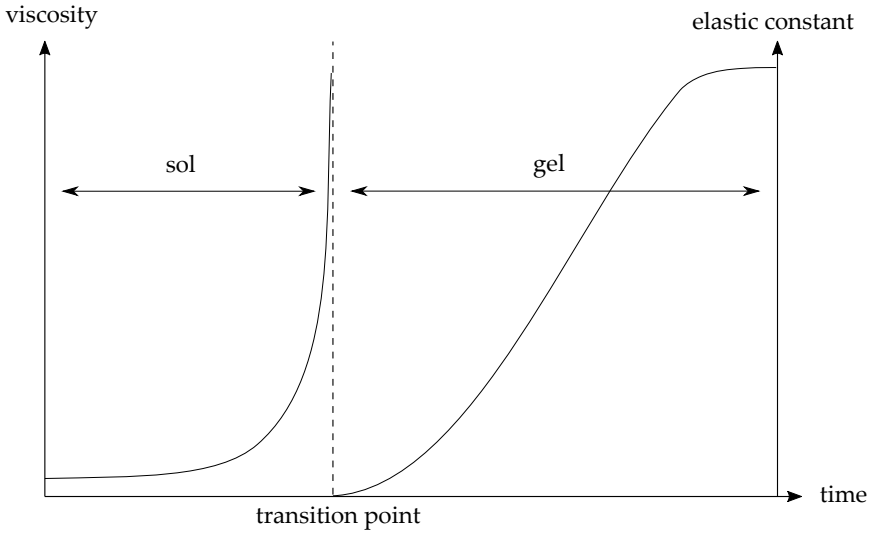

Figure 2.19: Time-evolution of viscosity in sol-phase and elastic constant in gel-phase.

The experimental procedure is as follows:

(a.) Hydrolysis: 2.7g of absolute ethanol (99% purity) is added drop-by-drop to 5.8g of TEOS and allowed to stir.

(b.) Acid Catalysis: 1g of 0.1M HCl is added to this solution. This makes the rate of hydrolysis faster than the condensation step, favoring the formation of linear polymers over branched ones. This also tends to the formation of smaller particles of the resulting gel.

(c.) Magnetic stirring: This final solution is allowed to agitate on a magnetic stirrer for about 24 hours to ensure homogeneity of the sol.

(d.) Filtering: Filtering of the solution with a 0.2 μm filter is an important step as it aides in the removal to unwanted dust particles.

(e.) Addition of $CoFe_2O_4$ ferrofluid: To this filtered mixture, different quantities of cobalt ferrite NPs are added keeping in mind the different volume fraction ϕ of NPs required. Varying the volume fraction of NPs in the composite varied the refractive-index of the resulting composite.

(f.) Filtering: This MO composite solution is again filtered through a 0.2 μm filter to ensure NP aggregates do not pass through. A well-prepared MO solution seems uniform in color and consistency.

Having successfully doped the TEOS sol with the $CoFe_2O_4$ ferrofluid, the next step is to dip-coat the solution on a substrate. The technique of dip-coating is the focus of the next section.

2.2.2 Dip-coating

Dip-coating is a simple procedure employed in this work to produce uniform thin-films. Its consists of immersing a substrate in a liquid and withdrawing it gently with a constant velocity. The result is a thin-film of the liquid deposited on both sides of the substrate. Figure 2.20 schematically illustrates these steps.

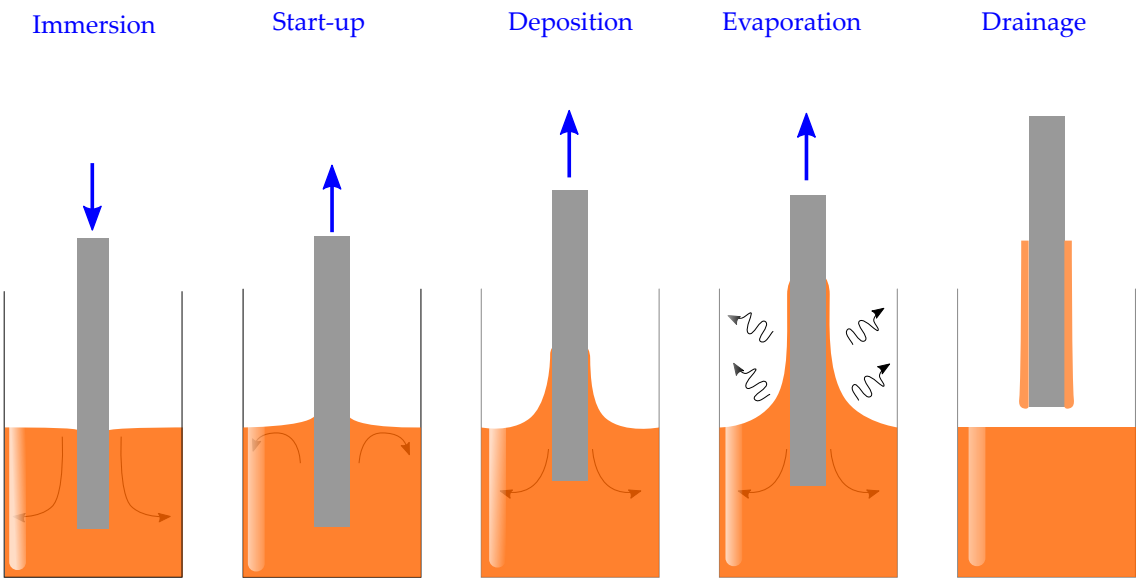

Figure 2.20: Various steps in dip-coating method.

Thin-film formation occurs during the withdrawal of the substrate. The retracting substrate causes the liquid to move with it with some part sticking to the surface and some part falling back to the liquid bath. At this stage, there is evaporation of the liquid solvent that takes place simultaneously and activates the condensation reaction. A parabolic thickness profile is seen during retraction (see figure 2.21).

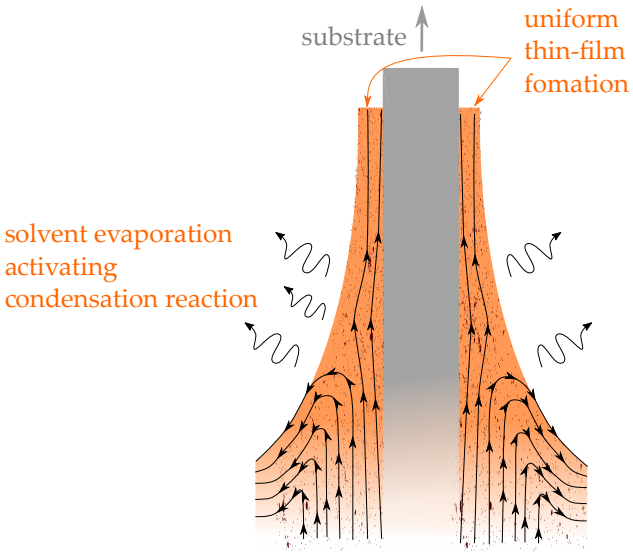

Figure 2.21: Thin film formation during dip-coating.

The final thickness, h of the film depends on the viscous drag $\eta U_0 h$ and gravitational pull $\rho g h$. Scriven *et al.* [125] state that for high-values of liquid viscosity and substrate withdrawal speed, the resulting thickness is expressed as follows:

$$h = C\sqrt{\frac{\eta U_0}{\rho g}} \tag{2.15}$$

where C is a constant, equal to 0.8 for a newtonian liquid, η is the viscosity, U_0 is the withdrawal velocity, ρ is the density of the solution, g is the gravitational constant. However, when the substrate withdrawal velocity and liquid viscosity are low, which is usually the case with sol-gel film deposition, the above relation is modified to as expressed below taking into account the liquid-vapor surface tension γ:

$$h = C\left[\frac{(\eta U_0)^{2/3}}{(\gamma)^{1/6}(\rho g)^{1/2}}\right] \tag{2.16}$$

The above relations show that the withdrawal velocity plays an important role in the final thickness of the thin film. Experimentally, the dip coating procedure was done with a glass/pyrex substrate which was firmly fixed to a holder and the sol was poured into a teflon beaker kept on a stand connected to an electric motor. Instead of moving the substrate, the beaker was allowed to move vertically with a fixed velocity thanks to a potentiometer connected to the motor that controlled its velocity (see figure 2.22).

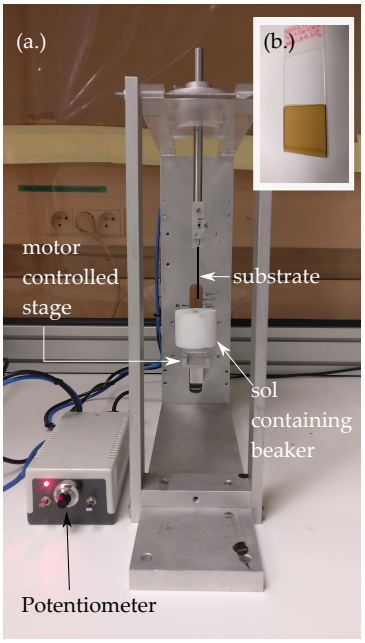

Figure 2.22: (a.) Snapshot of the dip-coating apparatus used to produce homogeneous thin-films of MO composite. (b.) (inset) MO thin film prepared by dip-coat method.

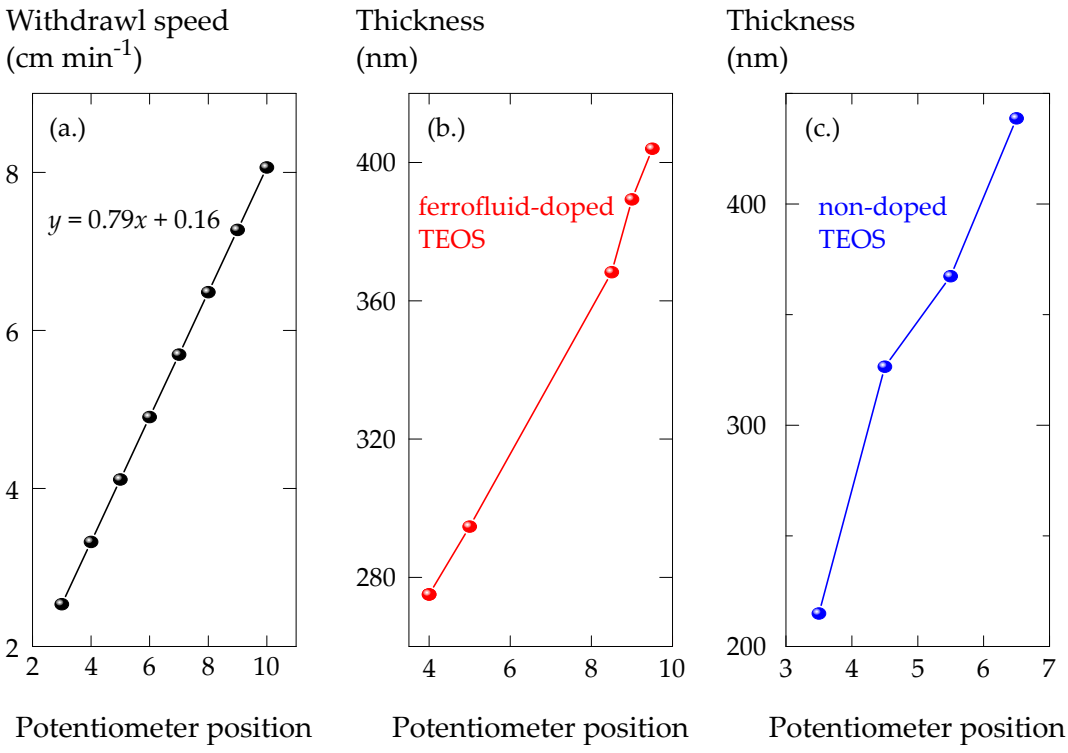

Figure 2.23: (a.) Variation of potentiometer position and consequent withdrawal speed. Variation of potentiometer position and resulting thin-film thickness for doped (b.) and non-doped (c.) silica precursor.

The potentiometer used allowed speeds from 1 cm/min to 8.2 cm/min for different positions of the potiometer (see figure 2.23). Different velocities were used to deposit thin films of varying thicknesses. Once a thin film of the MO composite was successfully produced, it was thermally annealed at 90°C for 1 hour. The thin-film thicknesses were measured using a *Bruker DektatXP* profilometer. Figure 2.23 (b.) and (c.) graphically show variation of the resulting thin-film thickness for doped (i.e. with $CoFe_2O_4$ NPs) silica precursor and non-doped (i.e. without $CoFe_2O_4$NPs) one, respectively.

2.2.3 Refractive index

Once the cobalt ferrite NPs are incorporated in the silica host, the relation between dielectric permittivity of the resulting MO composite and that of the constituent materials can be obtained through effective medium theory [126]. In first approximation, and for small values of volume fraction ϕ, it is expressed as:

$$\epsilon_c = \phi\epsilon_{NPs} + \big(1-\phi\big)\epsilon_h \tag{2.17}$$

where ϵ_c and ϵ_h are the dielectric permittivities of the composite and host, respectively and, ϕ is the volume fraction of $CoFe_2O_4$ NPs. ϵ_c is determined by ellipsometry measurements. Figure 2.24 shows the refractive-index n and coefficient of extinction k as a function of incident wavelength (600 nm-1700 nm) for the case of a MO composite doped with a volume fraction of cobalt ferrite NPs, $\phi = 22\%$. Considering the fact that the MO behavior of cobalt ferrite reaches a maximum at around 750 nm and 1550 nm (see figure 1.4(b.)), it is important to know its characteristics at these wavelengths. Figure 2.25 (a.) and (b.) shows the variation of n and k for different volume fraction of $CoFe_2O_4$ NPs at incident wavelengths of 750 nm and 1550 nm.

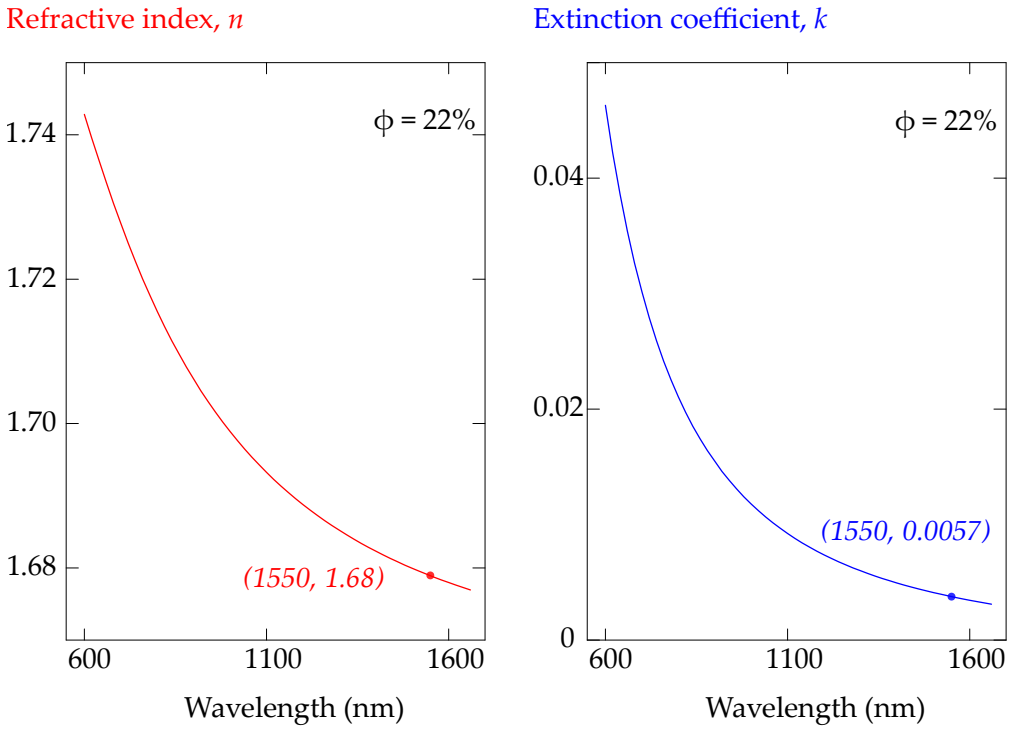

Figure 2.24: Experimentally measured values of refractive-index (a.) and coefficient of extinction (b.) for a MO composite doped with 22% volume fraction of cobalt ferrite NPs.

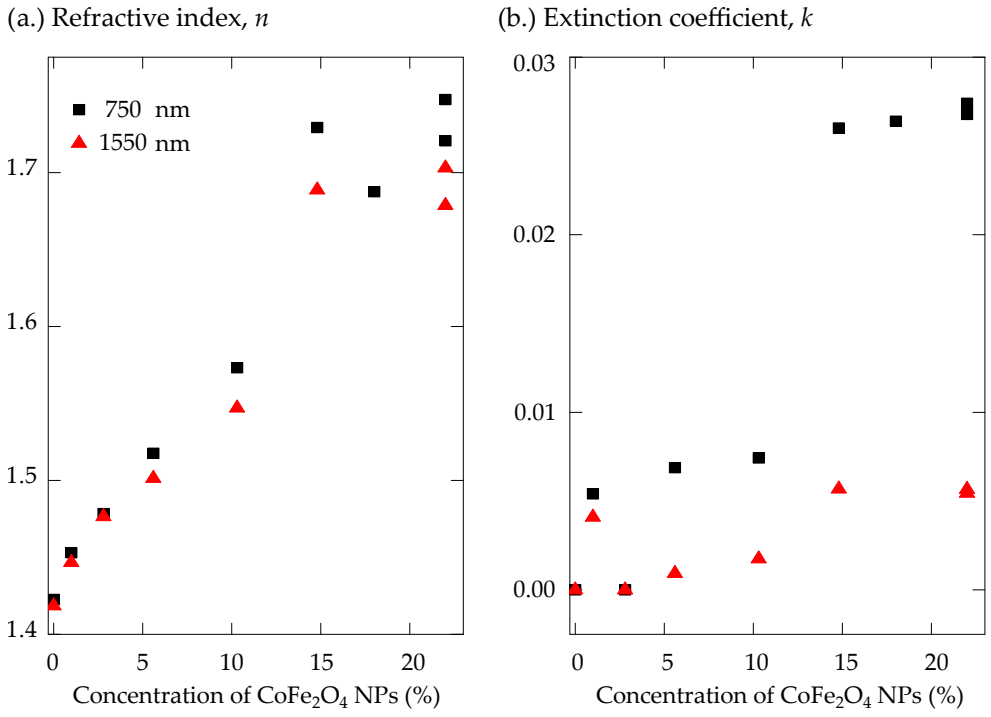

Figure 2.25: Measured refractive index n (a.), and extinction coefficient k (b.) for different concentrations of cobalt ferrite ($CoFe_2O_4$) NPs at incident wavelengths of 750 nm and 1550 nm.

Calculation of volume fraction of NPs: The volume fraction ϕ of NPs embedded in the silica matrix is determined by comparing its specific Faraday rotation to that of a liquid sample containing 1% volume fraction at 820nm (wavelength at which the detection system is most sensible) which is measured to be 166 $^{\circ}\text{cm}^{-1}$. Upon such a comparison with 0.9% sample and 22% sample, ϵ_h is calculated to be 2.04 and $\epsilon_{NP} = 5.45$ using equation 2.17. The values of ϵ_c for the 0.9% concentration and 22% concentration were taken from ellipsometry measurements to be 1.44 and 1.68, respectively. The next section introduces the experimental setups used in this work to measure the optical and MO characteristics of samples followed by a short description on their numerical simulations.

2.2.4 Compatibility of MO composite with other dielectrics

As explained in chapter 1, compared to a homogeneous MO thin-film, a MO system with 1-D periodic variation of refractive-index may produce an enhancement of resulting magneto-optic effects. Achieving this requires selecting a dielectric material that offers a high refractive-index contrast and good compatibility with the MO composite, chemical stability and low absorption in the wavelength range of interest. Figure 2.26 shows SEM images of our MO composite incorporated in a 2-D template of TiO_2 and a 1-D template of Si_3N_4. Seeing that the MO composite can completely occupy the empty space between the grating pillars/ridges is a proof of feasibility of the final MO grating structure.

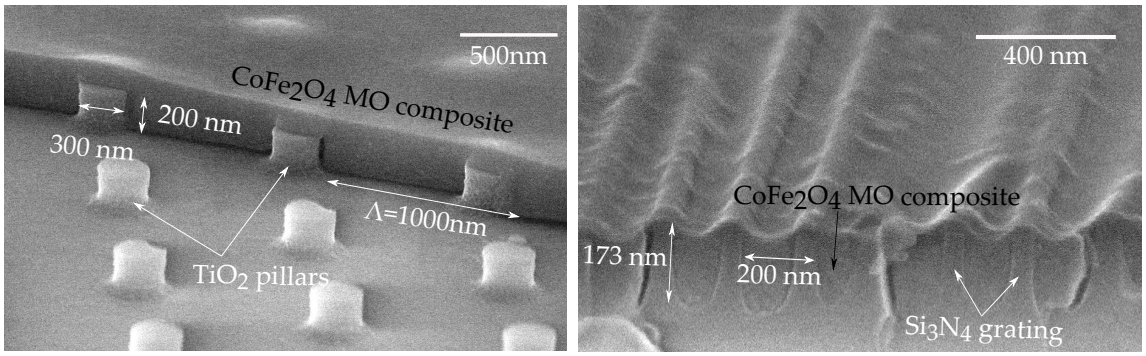

Figure 2.26: Compatibility of cobalt ferrite MO composite (doped 1%) with titanium dioxide TiO_2 (left) and silicon nitride Si_3N_4 (right).

2.3 Optical and Magneto-Optical characterization

2.3.1 Optical characterization setup

Figure 2.27 shows the optical setup used in this thesis work to characterize the reflectance and transmission of samples. It consists of a super-continuum source (*Leukos-SM-OEM*) with an output range of 200 nm-2000 nm complemented by a visible-infrared detector. Light from the source passes through a polarizer to make it either TE- or TM polarized which then hits the sample. For transmittance measurements, the incident angle can be varied from 0° to 80° while for reflectance, the incident angle can be varied from 5° to 80°.

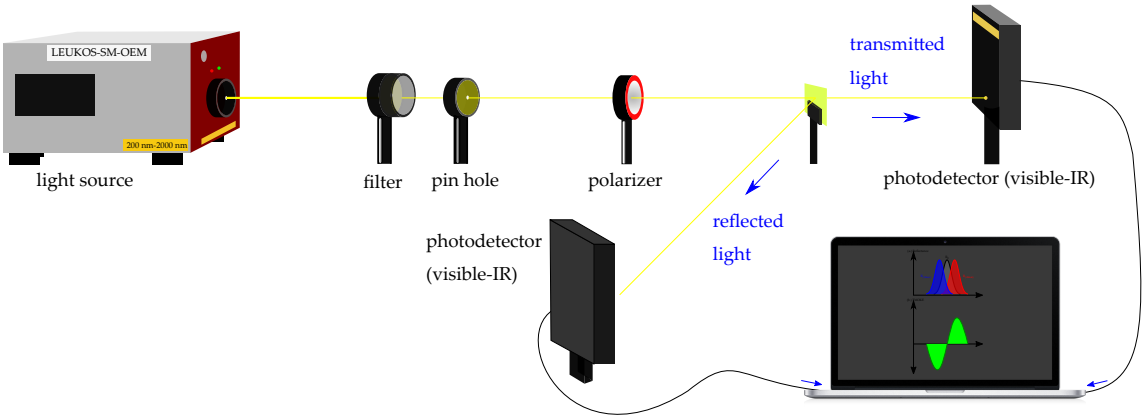

Figure 2.27: Schematic of the optical bench set-up to measure angle-varied dependence of transmission and reflection.

This bench serves no interesting purpose in the optical characterization of plain MO thin-films. However, its usefulness will be evident in the next chapter as we try to excite guided modes in those films.

2.3.2 Magneto-Optical characterization setup

MO thin films were characterized for their polarization rotation and ellipticity by a highly sensitive (0.001°) magneto-optical bench developed in-house and explained below. The bench could study the output light emitted by the thin-film in transmission configuration (Faraday effect) and in reflection configuration (PMOKE and LMOKE). Figure 2.28 schematically describes this set-up. Due to the geometry of the electromagnet polar pieces and the size of the injection and collection systems,

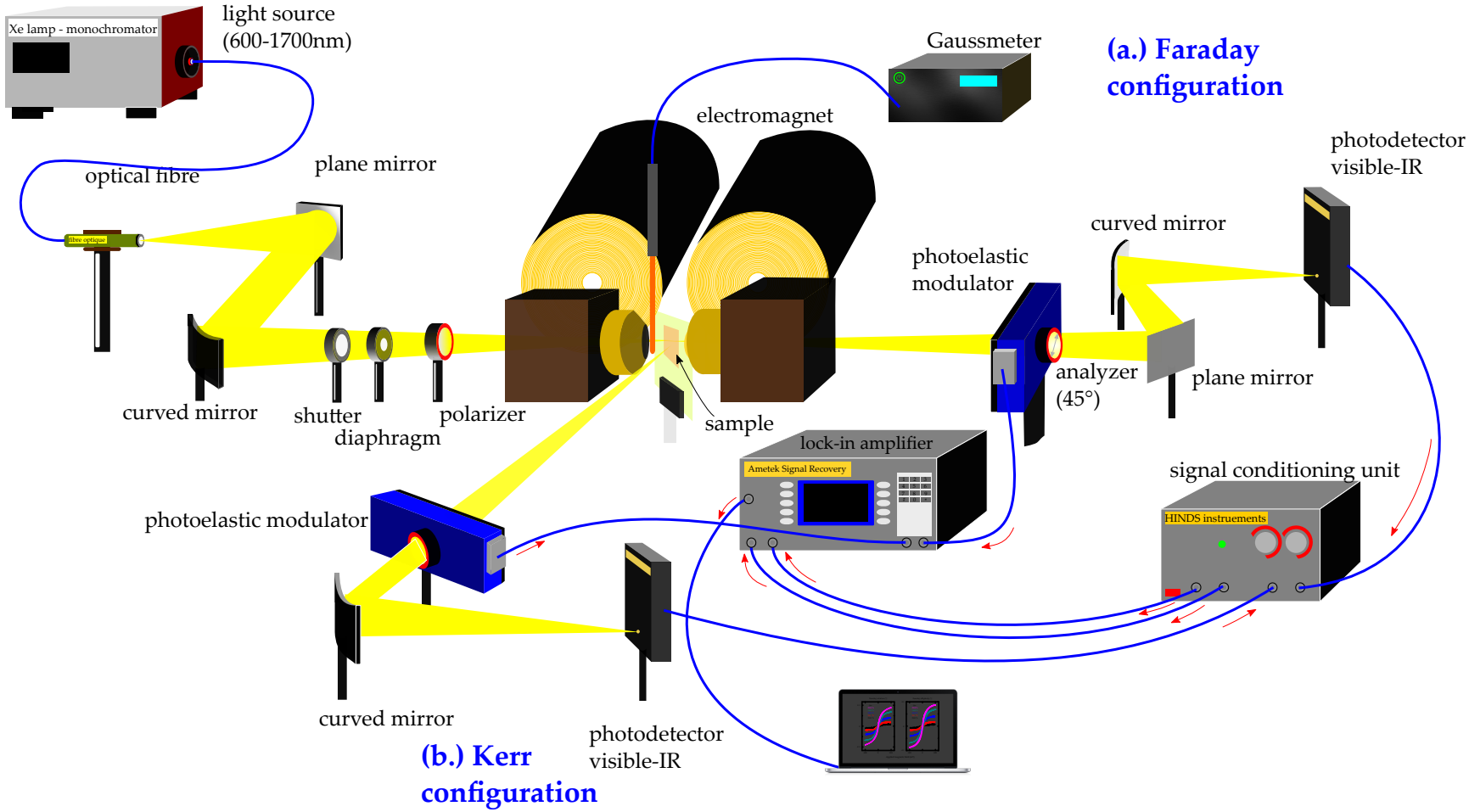

Figure 2.28: Schematic depiction of the MO bench to study polarization properties of light in transmission (a. Faraday) and in reflection (b. Kerr) configuration.

the L- and PMOKE can not be measured for every angle of incidence. LMOKE is limited to the range [25°-55°] and, PMOKE to [55°-90°] . For both, it is not possible to work at or close to the normal incidence.

The setup consists of a 450 W Xenon lamp source (*Horiba Jobin Yvon*) ranging from 150 nm to 1800 nm. In front of it is a motorized monochromator aiding in the selection of the required wavelength with an adjustable slit to modify the FWHM of the output light. This light beam from the monochromator passes through an optical fiber to a filter which serves to transmit only the zeroth diffraction order and suppresses the rest. Figure 2.29 shows the FWHM (Full-Width-Half-Maximum) and corresponding light intensity as a function of the thickness of the adjustable slit from 700 μm to 6900 μm for an incident wavelength of 493 nm.

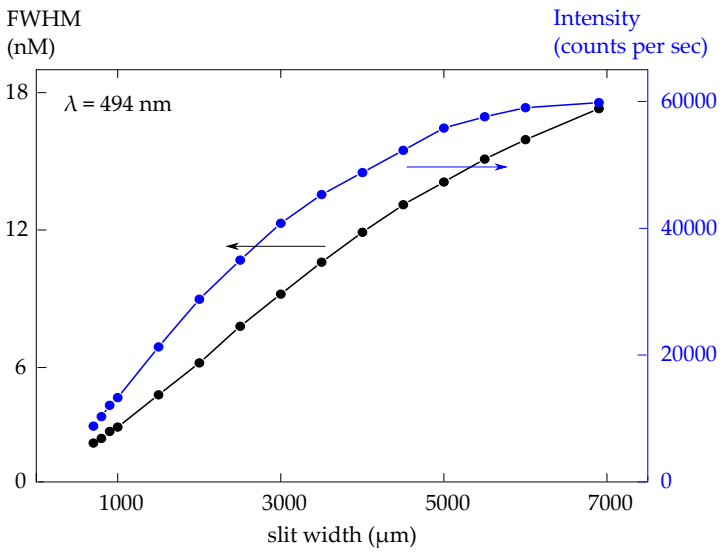

Figure 2.29: Full Width Half Maximum (FWHM) and output light intensity of the Xenon lamp source associated to the monochromator (λ=494 nm).

As evident, increasing the slit thickness increases the amount of light exiting the lamp but decreases its Q-factor i.e. $\left(\frac{\lambda_0}{\Delta\lambda}\right)$. The light exiting the optical fiber being divergent and non-polarized is made to pass through a system of spherical mirrors which focuses the light beam to a tiny point with a diameter of about 1 mm and a polarizer P1 to polarize it linearly. The latter is oriented with a sensitivity of 0.001° using an in-house software-controlled motor. The light beam passes then through an electromagnet capable of generating a dynamic magnetic magnetic field of upto 800 mT along the direction of the propagating light beam thereby facilitating the measurement of Faraday effect. The sample to be measured is

placed vertically between the two poles of the electromagnet where spherical mirrors focus the beam. A hall probe is also inserted between the two poles so as to measure the magnetic field in real-time. It is here where the light, initially linearly polarized with no ellipticity experiences Faraday effect i.e. Faraday rotation θ_F and Faraday ellipticity ϵ_F. Once the light leaves the electromagnet, it passes through a photo-elastic modulator (*Hinds Instrument PEM-90*). A PEM is an isotropic material subject to a mechanical stress due to which it becomes optically anisotropic and exhibits birefringence, this is called the photoelastic effect. The PEM used at the bench consists of a silica bar connected to a piezoelectric transducer oscillating at frequency of 50kHz driven by an electronic circuit which periodically modulates the state of polarization of the light beam. The phase-retardation produced is expressed as follows:

$$\Delta = \Delta_m \cos(2\pi f t) \tag{2.18}$$

where, Δ_m=modulation amplitude, f is the operating frequency = 50 kHz, t=time. After passing through the PEM, the light passes through an analyzer oriented at 45° so that the two decomposed components of the light can interfere together before being sent to the detection system.

The detection system consists of a photo-detector which converts the incoming light signal to a voltage signal. It is connected to a signal conditioning unit (*Hinds Instruments-SCU 100*) which splits this signal into its AC and DC components, amplifies them with a certain adjustable gain and sends these amplified AC and DC parts to the AC and DC outputs. These outputs are connected to a lock-in amplifier (*Ametek Signal Recovery Model 7270 DSP*) wherein the AC and DC components are precisely measured. The working of a lock-in amplifier is explained in the next subsection.

The light intensity reaching the photodetector can be mathematically expressed using Jones matrix formalism in which polarized light after passing through a series of optical elements is determined as a product of individual Jones matrices for the elements times the Jones vector for the initially linearly polarized light. First, linearly polarized light passing through the MO system undergoes Faraday rotation and Faraday ellipticity. Its Jones matrix can be expressed as follows:

$$\begin{bmatrix} \cos(\theta_F) & -\sin(\theta_F) \\ \sin(\theta_F) & \cos(\theta_F) \end{bmatrix} \begin{bmatrix} \cos(\epsilon_F) \\ \sin(\epsilon_F) \end{bmatrix}$$

This light then passes through the PEM. Jones matrix for a PEM is expressed as:

$$\begin{bmatrix} \exp\{i\Delta_m \cos(2\pi ft)\} & 0 \\ 0 & 1 \end{bmatrix}$$

It then passes through an analyzer with a 45° axis whose corresponding Jones matrix is expressed as:

$$\begin{bmatrix} 1/2 & 1/2 \\ 1/2 & 1/2 \end{bmatrix}$$

The resultant light beam possesses an electric field expressed by the multiplication of matrices in reverse-chronological order as follows:

$$\vec{J_{out}} = \begin{bmatrix} 1/2 & 1/2 \\ 1/2 & 1/2 \end{bmatrix} \begin{bmatrix} \exp\{i\Delta_m \cos(2\pi ft)\} & 0 \\ 0 & 1 \end{bmatrix} \begin{bmatrix} \cos(\theta_F) & -\sin(\theta_F) \\ \sin(\theta_F) & \cos(\theta_F) \end{bmatrix} \begin{bmatrix} \cos(\epsilon_F) \\ \sin(\epsilon_F) \end{bmatrix}$$

Solving the above relation, we obtain the intensity of light as:

$$\begin{aligned} I = \frac{1}{2}\big[1 - \sin(2\theta_F)\cos(2\epsilon_F) J_0\big(\Delta_m\big) + \\ 2\sin(2\epsilon_F) J_1\big(\Delta_m\big)\sin(2\pi ft) + \\ 2\sin(2\theta_F)\cos(2\epsilon_F) J_2\big(\Delta_m\big)\sin(2*2\pi ft) + ...\big] \end{aligned} \tag{2.19}$$

where the first term, independent of frequency f, is the DC term I_{DC}. The second and third terms, being dependent on the f and $2f$, respectively, are the first and second harmonics I_f and I_{2F}, J_i is the Bessel's function and Δ_m is the amplitude of modulation by the PEM. In our case, the J_0 term is made to be zero so that the first term becomes independent of the rotation and ellipticity introduced by the system with the second and third terms being expressed as:

$$\begin{aligned} I_f &\propto \sin(2\epsilon_F) &&\propto \mathbf{2}\epsilon_\mathbf{F} \\ I_{2f} &\propto \cos(2\epsilon_F)\sin(2\theta_F) &&\propto \mathbf{2}\theta_\mathbf{F} \end{aligned} \tag{2.20}$$

I_f and I_{2f} are measured in volts and so, a calibration is done to obtain values of Faraday ellipticity and FR in degrees.

Case1: By using the lock-in amplifier at the PEM modulation frequency f, it detects the I_F signal corresponding to Faraday ellipticity.

Case2: By using the lock-in amplifier at twice the PEM modulating frequency i.e. 2f, it detects the I_{2F} signal corresponding to FR.

Such a detection mechanism allows the setup to measure polarization rotations of upto 0.001° easily.

Working of a Lock-in Amplifier

The output signal of a system-under-study consists of a signal which contains information about the response of the system buried in unwanted noise. A lock in amplifier serves to extract this response signal from the unwanted noise efficiently. To be efficient, the output signal before entering the lock in amplifier is modulated, for instance with a PEM, at a high frequency f (f=50kHz in this case) so that the $1/f$ noise becomes almost negligible and the lock in amplifier is then just referenced to this frequency f. Due to the fact the noise is usually spread over a wider range of frequencies than the signal, the LIA uses Fourier transformation to convert the output signal from time domain (where the signal and noise are indistinguishable) to the frequency domain. Consider V_r as the reference signal of the lock-in amplifier

$$V_r(t) = A_r * \cos(2\pi f_r t) \tag{2.21}$$

and, V_s as the signal containing noise

$$V_s(t) = A_s * \cos(2\pi f_s t + \theta_s) \tag{2.22}$$

First step in a lock-in amplifier is to pass these two signals through a frequency multiplier. Mathematically, this is equivalent to a multiplication of the two signals

$$\begin{aligned} V_{mix} &= V_r(t)V_s(t) \\ &= A_r A_s \sin(2\pi f_r t)\sin(2\pi f_s t + \phi_s) \\ &= \left(\frac{A_r A_s}{2}\right)\left[\cos\{2\pi(f_r - f_s)t - \phi\} - \cos\{2\pi(f_r + f_s)t\}\right] \end{aligned}$$

This operation simply results in a signal with two components, one at the sum and the other at the difference of the two constituent frequencies. Adjusting the reference signal frequency to be the same as the signal frequency (i.e. $f_r = f_s$), one gets a DC component with zero frequency and an AC component at twice the frequency 2f.

$$V_{mix} = \left(\frac{A_r A_s}{2}\right)\left[\cos\{2\pi(0)t - \phi\} - \cos\{2\pi(2f_r)t\}\right] \tag{2.23}$$

The lock-in amplifier uses a narrow pass filter to remove the 2f AC part and then it measures the signal as a DC measurement.

2.4 MO measurement of thin films

2.4.1 Faraday effect

Figure 2.30 shows the FR hysteresis for a MO composite containing 22% volume fraction of cobalt ferrite NPs in a silica matrix deposited on a plain BK-7 substrate as a thin-film at an incident wavelength of 760nm.

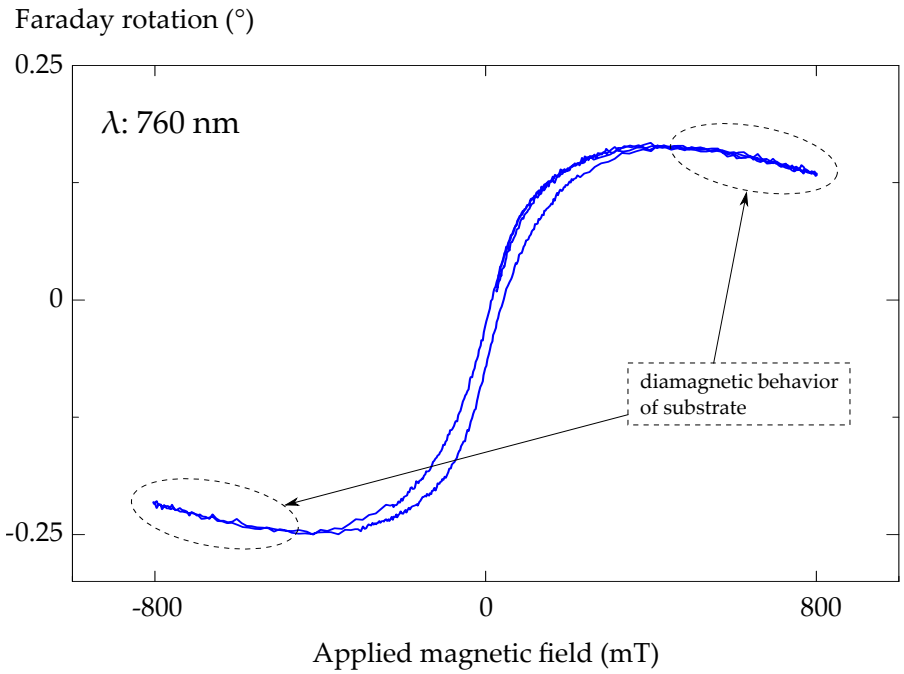

Figure 2.30: Experimental FR of a MO thin-film composite containing $CoFe_2O_4$ NPs deposited on a glass substrate for an incident wavelength of 760 nm.

At high magnetic fields, the hysteresis behavior does not attain saturation but shows a linear variation with respect to the applied field. This is due to diamagnetic contribution of the BK-7 substrate. Measuring the polarization plane rotation of just the substrate in the same magnetic field range gives its Verdet constant at that wavelength, which when subtracted from the above curve results in the FR of just the MO thin film composite. Figure 2.31 shows the determination of Verdet constant of silica substrate using equation 1.5 as slope of the curve between polarization plane rotation and applied longitudinal magnetic field. Upon subtracting the Verdet constant of the substrate from figure 2.30, one gets the FR of just a thin-film of MO composite as shown in figure 2.32 at that particular wavelength.

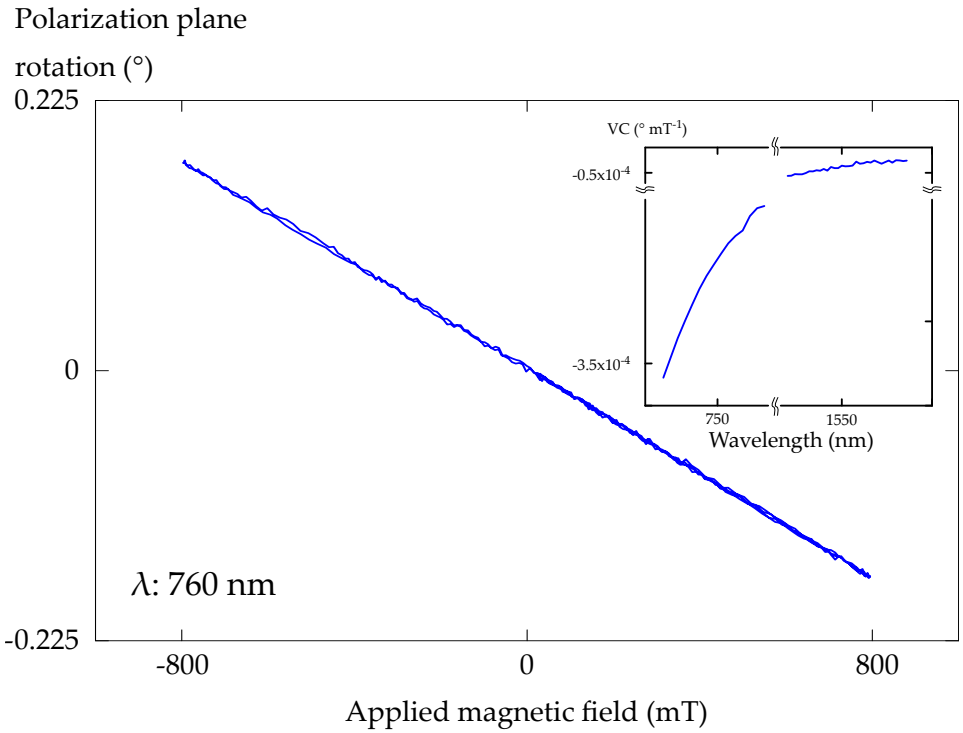

Figure 2.31: Experimental demonstration of Verdet constant of 1 mm BK-7 substrate for an incident wavelength of 760nm.

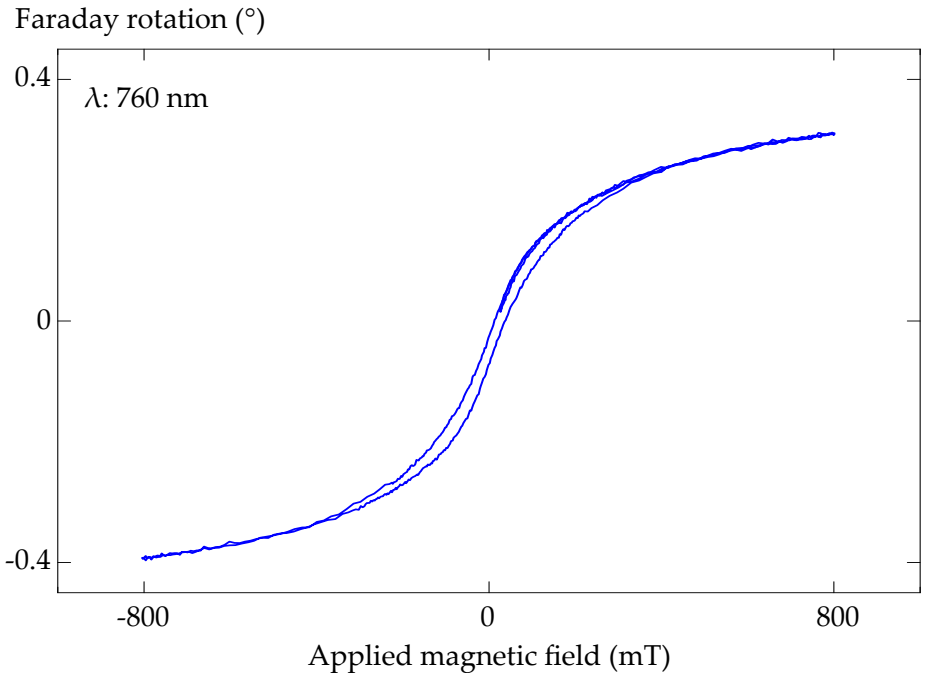

Figure 2.32: FR of just the MO thin-film after the subtraction of Verdet constant of BK-7 substrate.

In a similar manner, Faraday ellipticity can be plotted for a particular wavelength. Figure 2.33 demonstrates the Faraday ellipticity (which has a similar hysteresis behavior as FR) of MO composite thin-film containing $CoFe_2O_4$ NPs at an incident wavelength of 760 nm. Since passage of a linearly polarized light through a glass substrate does not introduce ellipticity in the output light, Faraday ellipticity hysteresis for a MO thin-film deposited on a glass substrate does not show any contribution due to the glass substrate. In such a manner, spectral variation of magneto-optic FR as well as Faraday ellipticity can be efficiently measured by extracting the average saturation value from their respective hysteresis loops and plotting them against their respective incident wavelength. Figure 2.34 demonstrates this step by plotting the specific FR and specific Faraday ellipticity for a MO thin film doped with 22% volume fraction of $CoFe_2O_4$ NPs.

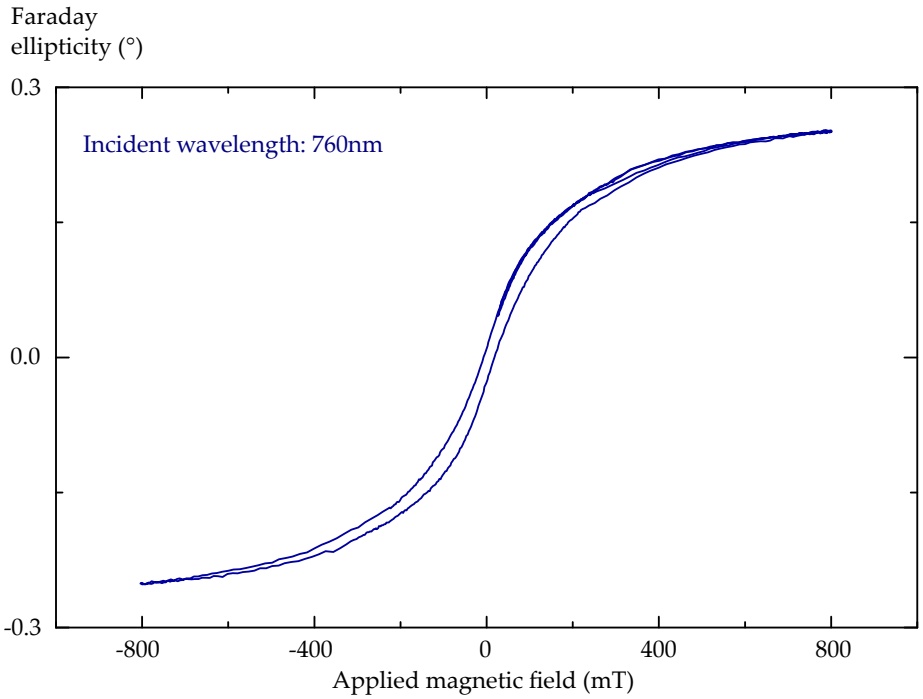

Figure 2.33: Experimental Faraday ellipticity of a MO thin-film composite containing $CoFe_2O_4$ NPs deposited on a glass substrate for an incident wavelength of 760nm.

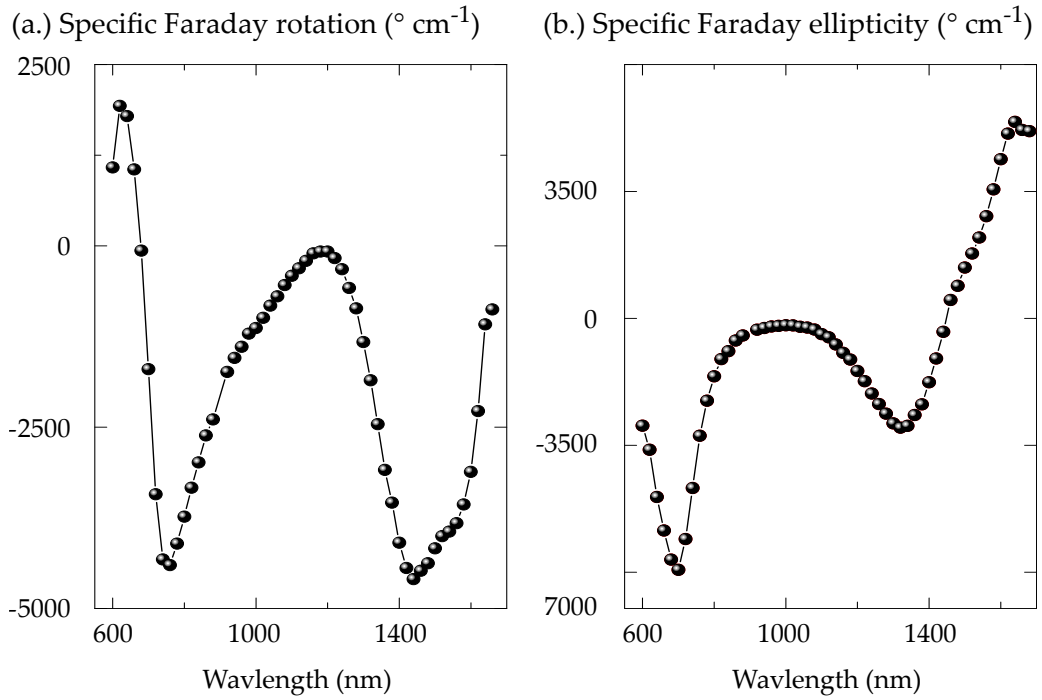

Figure 2.34: Specific FR (a.) and specific Faraday ellipticity (b.) as a function of incident wavelength for a MO thin-film doped with 22% volume fraction of $CoFe_2O_4$ NPs.

2.4.2 Kerr effect

The PMOKE is measured using the same apparatus as described in figure 2.28 but in reflection mode. Using the experimentally obtained values of specific Faraday effect in equations 1.11 and 1.12, the real and imaginary parts of the off-diagonal MO term ϵ_{MO} were calculated (figure 2.35). This was calculated for a thin MO film doped 22% having a thickness of 388 nm.

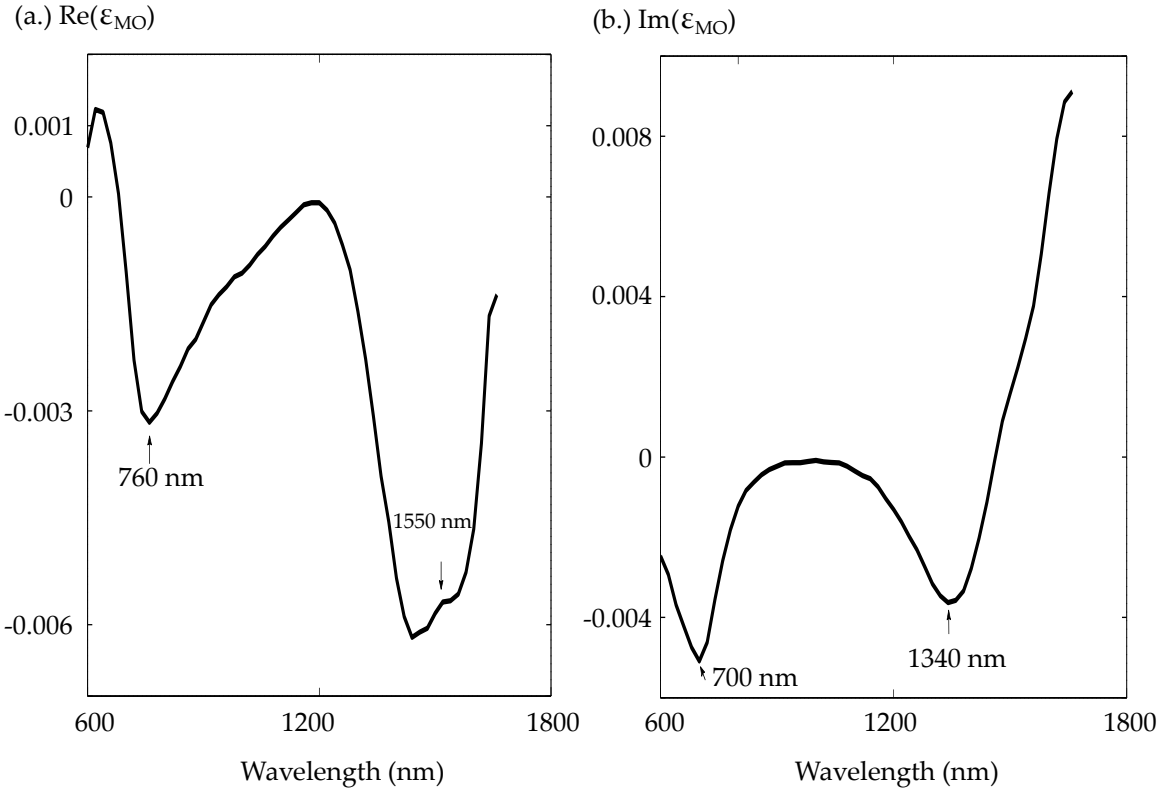

Figure 2.35: Real (a.) and imaginary (b.) parts of the off-diagonal MO term calculated for a MO composite film doped 22%.

Using these values of the MO constant, Polar MOKE for the thin film was simulated using the matrix method developed by Zak *et al.* [127], the results of which are coherent with the experimentally observed values for two angles of incidence: 55° and 72° (figure 2.36). The behavior of PMOKE resembles that of Faraday effect with two spectral regions of maxima. However, unlike Faraday effect, the magnitude of the effect is not the same in both the regions. Figure 2.37 claims the thickness of the MO layer to be the reason for it. It simulates the Kerr rotation (a.) and ellipticity (b.) for an incident angle $\theta_{\mathrm{i}} = 55°$ as the thin-film thickness increases from 300 to 420 nm.

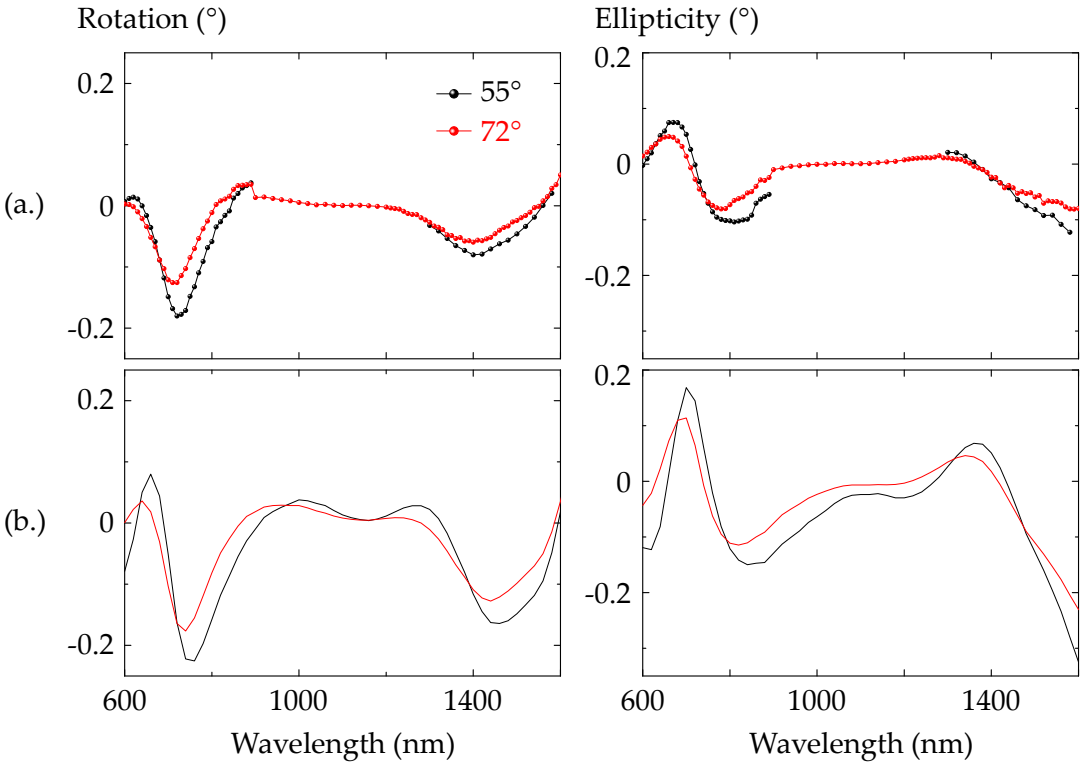

Figure 2.36: Measured (a.) and simulated (b.) polar Kerr rotation (left) and ellipticity (right) of a homogeneous MO thin film doped 22% for $\theta_{inc} = 55°$, 72°.

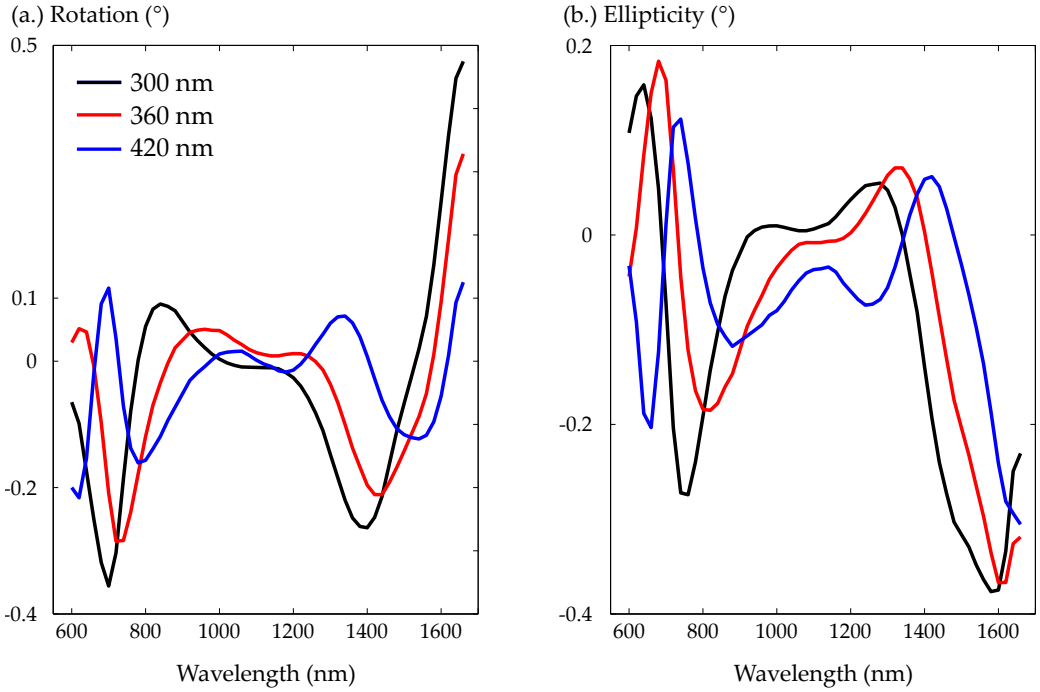

Figure 2.37: Simulations demonstrating the effect of thin film thickness on Polar Kerr rotation (a.) and ellipticity (b.) for an incident angle of 55°.

2.5 Numerical simulation of optical and MO behavior

Optical response of samples for this work were simulated with a commercial software called MC grating [108] developed from 1999 by Dr. Nikolay Lyndin – senior physicist of General Physics Institute, Moscow. It is based, among others, on:

- Rigorous Coupled Wave Analysis (RCWA), also called Fourier Modal Method for the study of rectangular profile. The method is based on the representation of electric and magnetic fields in the layers of the structure in the form of coupled waves propagating towards the Z-axis (see figure 2.38(a.)). The fields are expressed under the form of Fourier series according to Bloch theorem, and the continuity conditions of the tangential components of the fields are applied at the boundaries between the layers. Finally, the diffraction efficiencies are calculated using Poynting vector flux ratios.

- Chandezon method, (C-method) for the study of smooth profiles gratings [128–131].

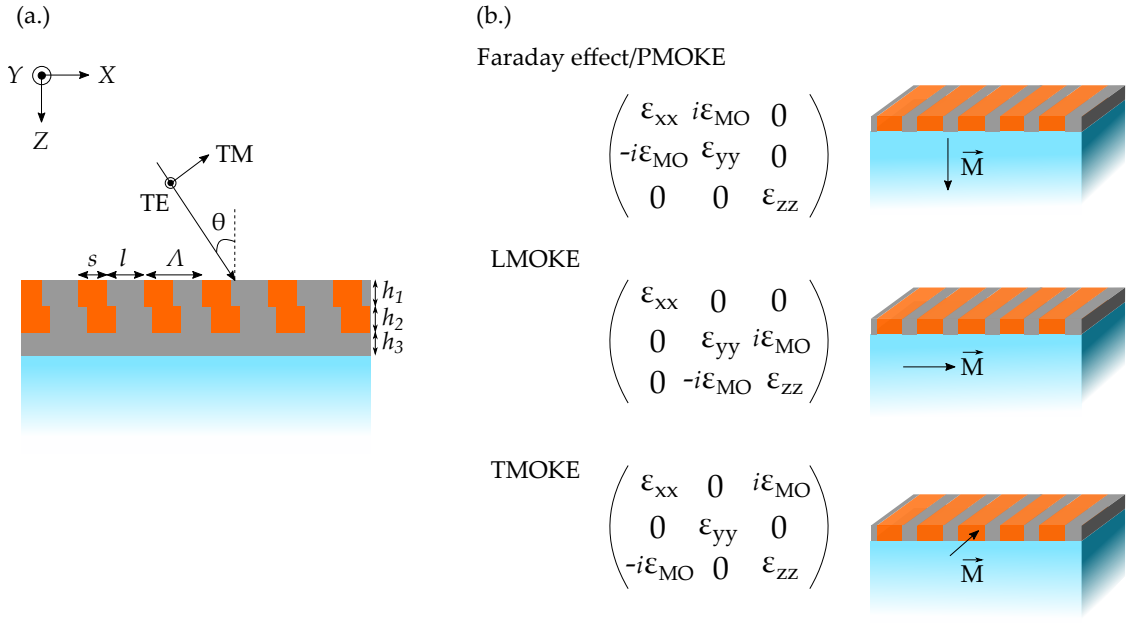

Figure 2.38: (a.) Opto-geometric parameters of 1-D lamellar diffraction gratings. (b.) Permittivity tensors associated with each MO effect for the chosen coordinate system.

This software is equipped with several features that permit, for instance, to perform

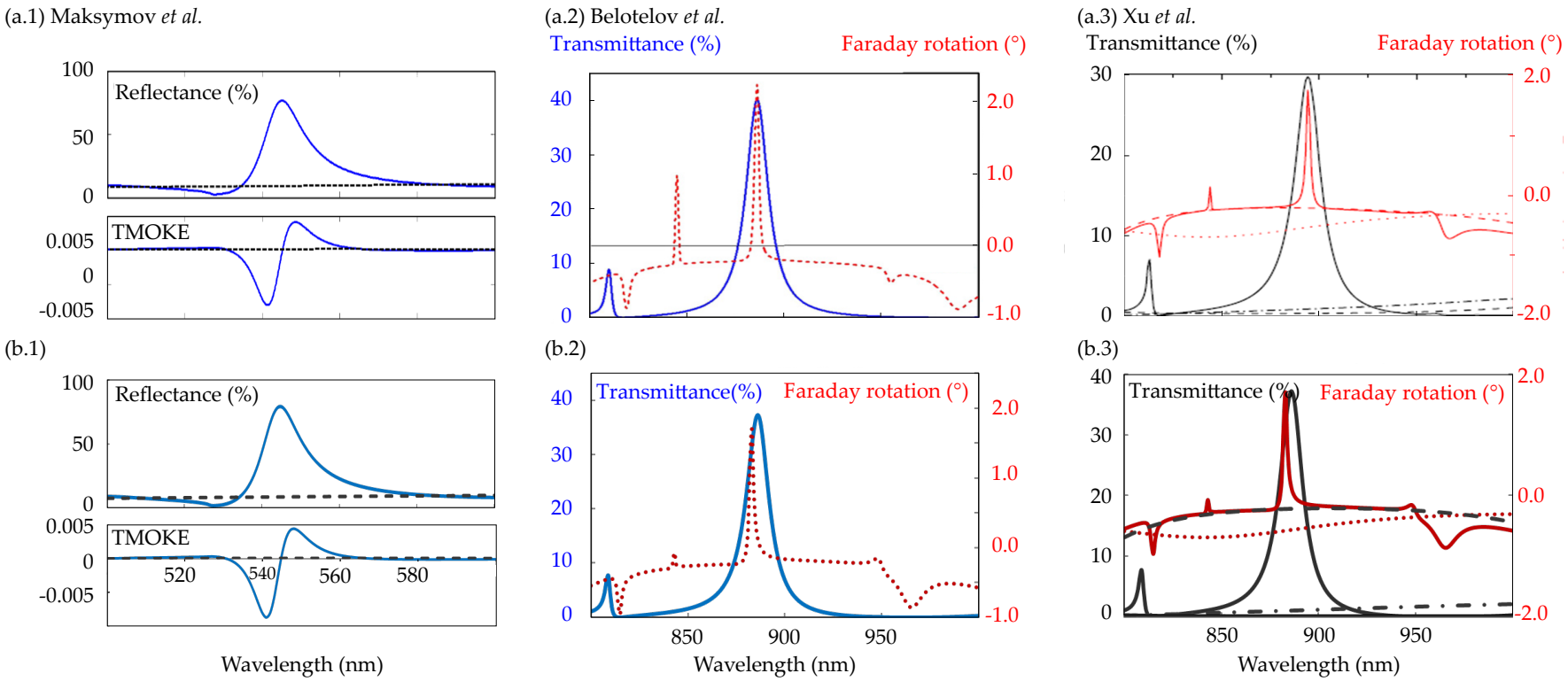

Figure 2.39: Comparison of simulations reported in literature (a.1, a.2 and a.3) with the ones performed using our homemade RCWA simulations (b.1, b.2, b.3).

optimizations, two-parameter scans and to obtain field maps. Nevertheless, it is not adapted to the simulation of diffraction gratings presenting anisotropic materials. Thus, in order to have a whole design capacity and calculate the MO response of our structures, an RCWA code has been developed within the team. Its features are reduced but, it permits to take in account the whole complex permittivity tensor for rectangular 1-D gratings. The RCWA applied to anisotropic materials is a well-documented method and is detailed in [132–135]. Validation of our anisotropic code was performed by comparing its results with published works concerning Faraday or Kerr effects. Some examples are presented in figure 2.39.

Figure 2.39(a.1), (a.2) and (a.3) represent the optical and MO behavior of the samples studied by Maksymov *et al.* [8], Belotelov *et al.* [10] and Xu *et al.* [136] respectively, which upon comparison with the corresponding simulations (figure 2.39(b.1), (b.2) and (b.3), respectively) using our RCWA code validates its efficiency.

2.6 Conclusion

The focus of this chapter was to detail the magnetic and MO properties of our composite in thin-film form. Crystal structure of cobalt ferrite was seen to be of inverse spinel structure in which Co and Fe cations occupy different tetrahedral and octahedral sites. With respect to magnetic properties, $CoFe_2O_4$ NPs are ferrimagnetic, mono-domained and possess a large magnetic anisotropy. Electronic transitions in either the tetrahedrally coordinated or octahedrally coordinated cations were responsible for the MO behavior of cobalt ferrite which in itself was due to spin-orbit interaction. Magnetization of NPs in ferrofluid form could be modeled by Langevin's theory of paramagnetism whereas that of NPs trapped in a host matrix display hysteresis behavior with a magnitude proportional to the volume fraction of NPs. A linear relationship between the magnetization and FR enables the behavior of the latter to be of hysteresis nature. A spectral variation of the FR displayed local maximum at around 750 nm and 1550 nm.

Thin film preparation of our MO composite was described starting from sol-gel method to impregnate cobalt ferrite NPs in a silica matrix followed by the details of dip-coating technique. Varying the dip-coating speed varied the thickness of the resulting film. Ellipsometry showed that by increasing the volume fraction of NPs in the composite, we can increase its refractive-index and coefficient of extinction.

SEM images of our MO composite with titanium dioxide (TiO_2) and silicon nitride (Si_3N_4) templates demonstrated good compatibility of our composite with the two materials for potential MO grating structures.

Following section focused on the experimental setups to characterize optical and MO behavior. A short description of the optical bench setup was followed by a detailed description of the magneto-optic bench along with some measurements of MO Faraday and polar Kerr effects. Measuring the polarization rotation for a sample of MO thin film composite on silica substrate showed the influence of the diamagnetic substrate at high magnetic fields. Removing its effect requires subtracting the Verdet constant of the substrate at the particular wavelength. On the other hand, since silica does not affect the ellipticity of light, no such diamagnetic influence is seen in the graphs of Faraday ellipticity. Using the experimental data for specific FR of a MO thin-film doped 22%, off-diagonal elements of the permittivity tensor were deduced. They were used to calculate polar Kerr effect at incident angles of 52° and 72° and showed coherence with experimentally measured ones. As expected, just like the Faraday effect, Polar Kerr effect also demonstrated the same regions of MO interest.

The aim of this thesis was established at this point which is to resonantly enhance the Faraday/MO effects of a homogeneous thin film by planar 1-D microstructuration. The final section of this chapter was a short description on the numerical simulation of optical and MO behavior of samples using Rigorous Coupled Wave Analysis (RCWA). A commercial software called MC grating allowed an intensive study of the optical response of samples. However, due to its inability to simulate structures presenting anisotropic materials, a homemade RCWA code was developed by the team which proved to be highly efficient in simulating the MO as well as optical results of structures reported in literature.

The next chapter is dedicated to the design, realization and characterizations of various 1-D MO structures.

CHAPTER

3

MAGNETO-OPTICAL ENHANCEMENT: DESIGN AND REALIZATION

The objective of this chapter is to materialize the main idea put forward in chapter-1 which is to enhance/modify the spectral MO effects of our composite material by 1-D planar structuration. The work presented in this chapter is, thus, a continuation of the efforts led by the group to enhance the MO properties with a system having good homogeneity at a large scale. Several MO structures with different designs and different compositions are studied for this purpose and the promising ones are presented. For the enhancement of MO effects involving polarization rotation, structures are designed with those parameters that target a simultaneous excitation of TE and TM resonances, while for TMOKE, a single TM resonance is sufficient. Optical resonances for the designed structures are simulated using a commercial software based on RCWA [108] to study their transmittance and reflectance, while their MO response is simulated using the homemade RCWA code presented in the previous chapter. Structures are then experimentally realized and compared with

their simulated performance. The chapter starts with magneto-plasmonic gratings, its design and composition followed by the different modes supported by the structure and terminating with its measured Faraday effect performance. Next is the section on all-dielectric structures. It starts with a introduction to two proposed designs and the measured performance of each structure based on that design. Finally, the chapter ends with the experimental MO study of the best grating structure.

3.1 Magneto-plasmonic gratings

Magneto-plasmonic gratings are those periodic structures containing a metal interfacing with a MO dielectric material. The motivation to use periodically perforated metals is to excite TM plasmon-modes and simultaneously invoke Extra-Ordinary Transmittance (EOT) [66], as illustrated in chapter-1. A majority of the work carried out in literature is led using a garnet magnetic film with a gold grating on top of it. More complex structures [9], [11] were only studied through simulations due to difficulties in the processing of garnets. Another kind of design has been chosen in this work.

3.1.1 Proposed design

Figure 3.1 (a.) shows the schematic of a relatively easy-to-fabricate magneto-plasmonic structure to use in transmission configuration. Our aim is to enhance Faraday effect and TMOKE at the excitation wavelength of EOT. The magneto-plasmonic grating consists of a suitable photoresist, that is sinusoidally etched to provide undulations in the thin Au layer that is deposited over it. This periodically undulated Au layer in contact with our dielectric MO composite layer above it can excite TE-/TM- guided modes in the MO layer and TM-polarized propagating surface plasmons along the Au/MO interface. The MO layer of the structure needs to be doped with enough $CoFe_2O_4$ NPs so as to ensure a high enough MO effect. Figure 3.1 (b.) shows the measured refractive index variation of our MO composite with a $CoFe_2O_4$ NP concentration of 14.8%.

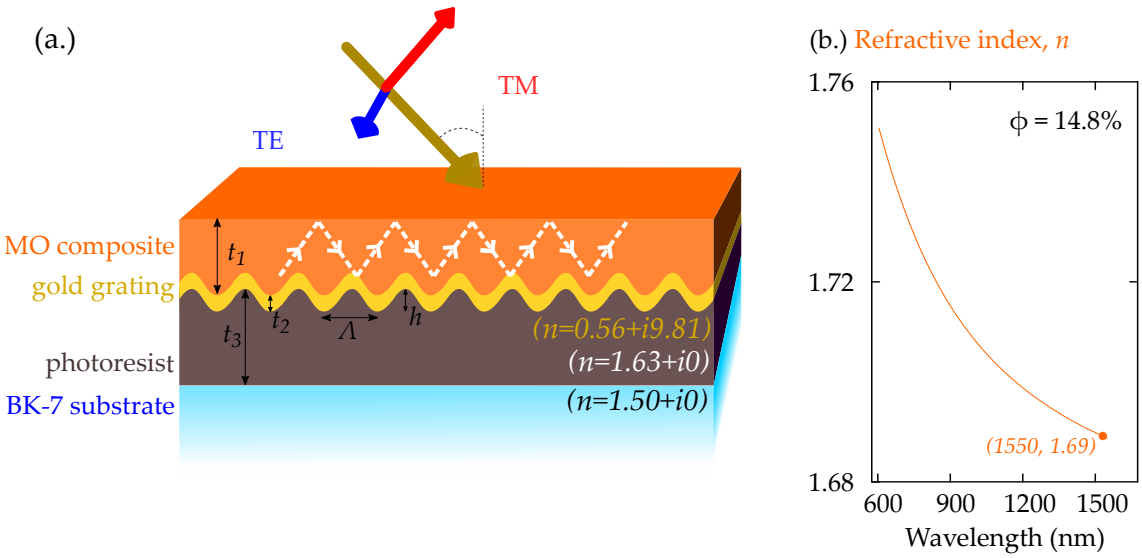

Figure 3.1: (a.) Schematic of a 1-D magneto-plasmonic grating along with refractive indices for the different layers at 1550 nm. (b.) Measured refractive index variation (n) of our MO composite containing 14.8% of $CoFe_2O_4$ NPs.

For sufficiently small thickness of the Au layer, it is possible that the plasmons created at the upper interface (*viz.* Au/MO) couple to the ones created at the bottom interface (*viz.* Au/photoresist). This coupling would result in the creation of two optical modes: an asymmetric mode with a high propagation loss called short-range plasmons, and a symmetric mode with a low propagation loss called long-range plasmons [137]. For a symmetric structure, its dispersion equations are expressed as follows:

$$\begin{aligned} \tanh\left(\frac{k_m w}{2}\right) + \frac{k_c \epsilon_m}{k_m n_c^2} &= 0 \qquad \text{Long-range plasmons} \\ \tanh\left(\frac{k_m w}{2}\right) + \frac{k_m n_c^2}{k_c \epsilon_m} &= 0 \qquad \text{Short-range plasmons} \end{aligned} \tag{3.1}$$

where ϵ_m is the permittivity of the metal medium, w is the metal layer thickness, $k_m = k_0\sqrt{n_e^2 - \epsilon_m}$, $k_c = k_0\sqrt{n_e^2 - n_c^2}$ and n_e is the modal effective index. Our structure is neither symmetrical nor posses a uniform metal layer. Nevertheless, approximating the asymmetry and the undulations to be small perturbations, the above equations still prove to be sufficient for our case.

Now, let us look at some optical and MO features of such a magneto-plasmonic structure starting with TMOKE.

3.1.2 TMOKE features

As a reminder, TMOKE enhancement occurs only in the presence of a TM resonance. Figure 3.2(a.) shows the TM transmittance simulated at 1550 nm for the above presented structure as a function of the grating period and incidence angle for a set of parameters (inset). For a grazing incidence ($\approx 80°$) and a period of 600 nm, an indication of extra-ordinary transmittance reaching 73% with a Full-Width Half Maximum (FWHM) of 81 nm manifested by the excitation of long-range and short-range plasmons can be evidenced (figure 3.2(b.)). Such a TM resonance should result in a TMOKE enhancement since the MO composite has quite a large effect around 1550 nm. Figure 3.2(c.) shows an influence of grating period and incidence angle variation on the spectral transmittance from which the chosen parameters of $\theta_{inc} = 80°$ and $\Lambda = 600$ nm seems to be the best.

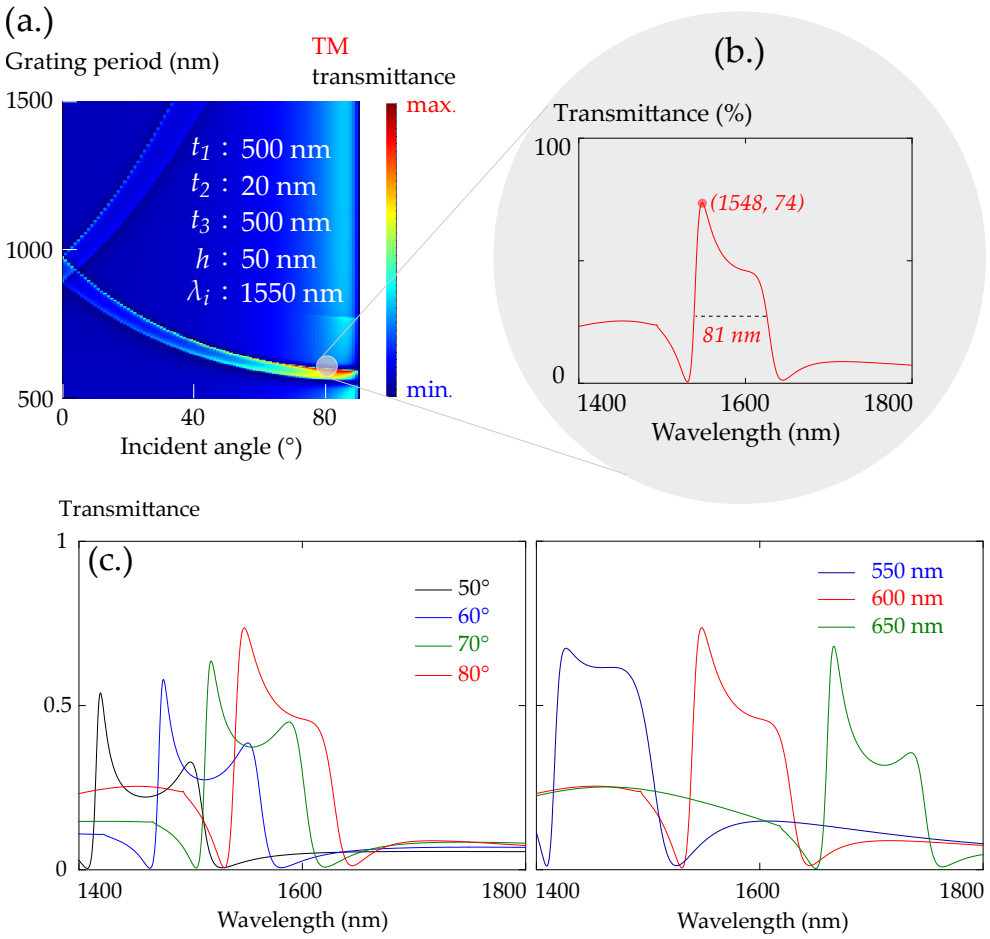

Figure 3.2: (a.) Color map of transmittance as function of grating period and incident angle for an $\lambda_i = 1550$ nm. (b.) TM transmittance at 80° incidence for $\Lambda = 600$ nm. (c.) Tolerance of incident angle, θ_i (left) and grating period, Λ (right).

Fabrication of the structure involves the first step of depositing a 500 nm photoresist (*Shipley SPR220*) layer on a BK-7 substrate followed by photolithographic exposure and etching. Figure 3.3 (a.) shows an Atomic Force Microscope (AFM) image of the etched photoresist with a period of 600 nm and height 136 nm. To this template 20 nm Au is thermally evaporated followed by a 525 nm thin layer of our MO composite with concentration ϕ=14.8%. Figure 3.3 (b.) demonstrates the TE and TM transmittances for the resulting magneto-plasmonic structure at 80° incidence. As expected, a resonant feature takes place around 1550 nm for TM transmittance, while TE transmittance remains close to zero. Comparing the measured TM resonance with the simulated one, there is a noticeable difference in its spectral behavior and efficiency, which could be explained by deviations in the grating profile shape and height from what was expected. Nevertheless, the spectra shows a peak in TM transmittance at 1474 nm signaling the definite presence of EOT.

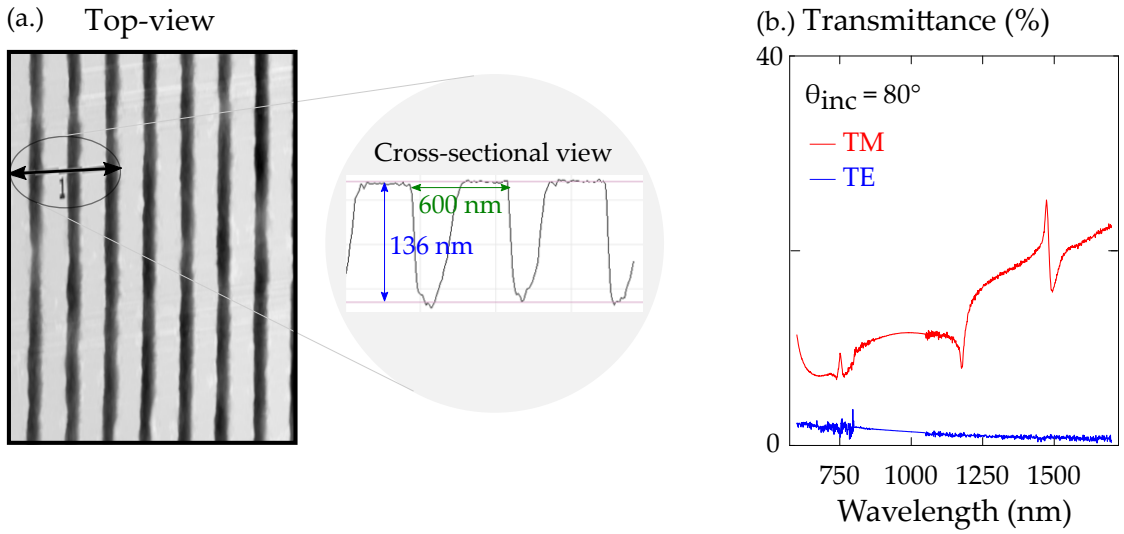

Figure 3.3: (a.) AFM image of the etched photoresist. (b.) Transmittance (TE, TM) measured for the magneto-plasmonic structure at 80° incidence.

At the moment, it is not possible to measure TMOKE at an angle of 80° with the MO setup. Thus, experimental TMOKE enhancement of this structure remains to be validated. The issue will be resolved in the future. As shown in figure 3.3(b.) no TE resonance occurs at 1550 nm. To obtain a Faraday effect enhancement, another configuration has to be chosen with this device.

3.1.3 Faraday effect modification

As explained previously, to obtain an optimal enhancement of FR, the proposed structure needs to simultaneously excite TE and TM modes. Figure 3.4 shows color maps of reflectance and transmittance as a function of grating period and incident wavelength for TM and TE light at 0° incidence on the structure. These color maps show that several modes are excited in the structure. To identify these modes, an analytical study is reported in figure 3.5 through the plot of plasmon modes, dielectric guided-modes and Wood's anomaly with a period/wavelength dispersion diagram.

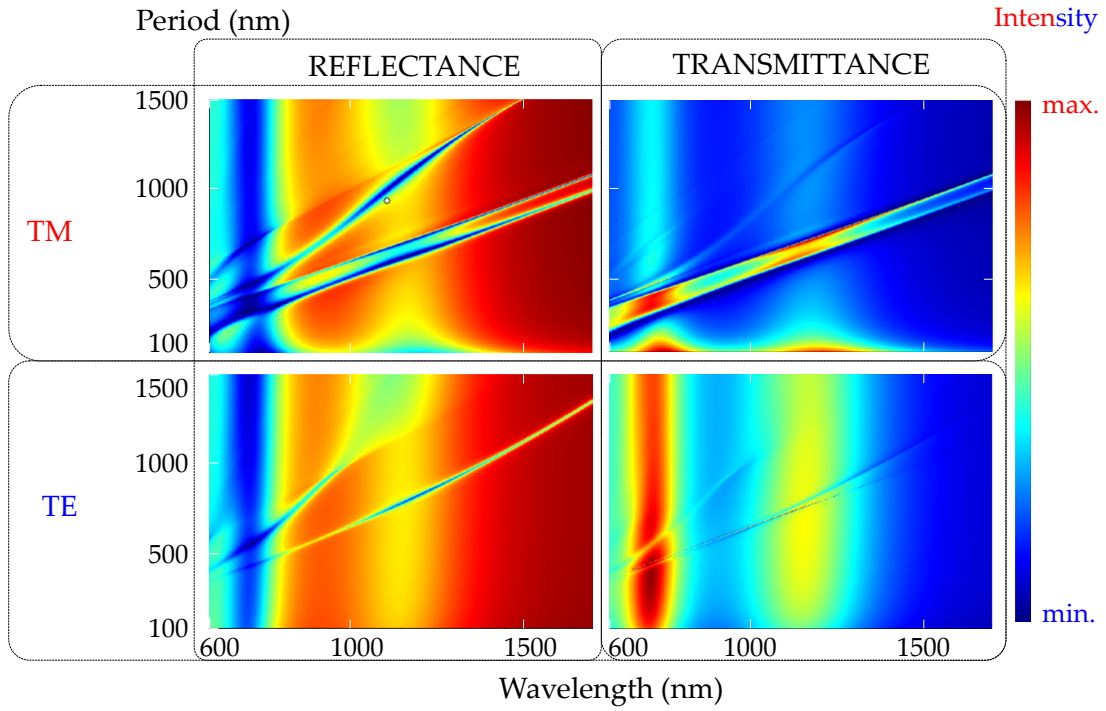

Figure 3.4: Color map of light intensity as a function of incident wavelength and grating period for the proposed magneto-plasmonic structure at 0° incidence.

Plasmon modes follow equation 3.1. The guided modes in the MO layer can be expressed by the dispersion relations demonstrated in chapter-1 (refer equations 1.27, 1.28) replacing the phase-change term when light reflects from the metal layer to $(\pi/2)$. Furthermore, a non-resonant situation (for both TE- and TM- polarization) called Rayleigh-Wood anomaly can arise when a diffraction order lies in the grating plane itself. It is described by the following equation:

$$\Lambda = \lambda_i \times \frac{m}{n_i \pm \sin(\theta_i)} \qquad \text{i = substrate, cover} \tag{3.2}$$

where Λ is the grating period, λ_i is the incident wavelength, m is the diffraction order, n is the refractive index, θ_{inc} is the incidence angle and $\pm$ sign represent the negative and positive orders, respectively. This dispersion diagram, realized on an equivalent structure (shown in inset), which is only constituted of a Au layer without undulations gives way to understand the color maps of figure 3.4.

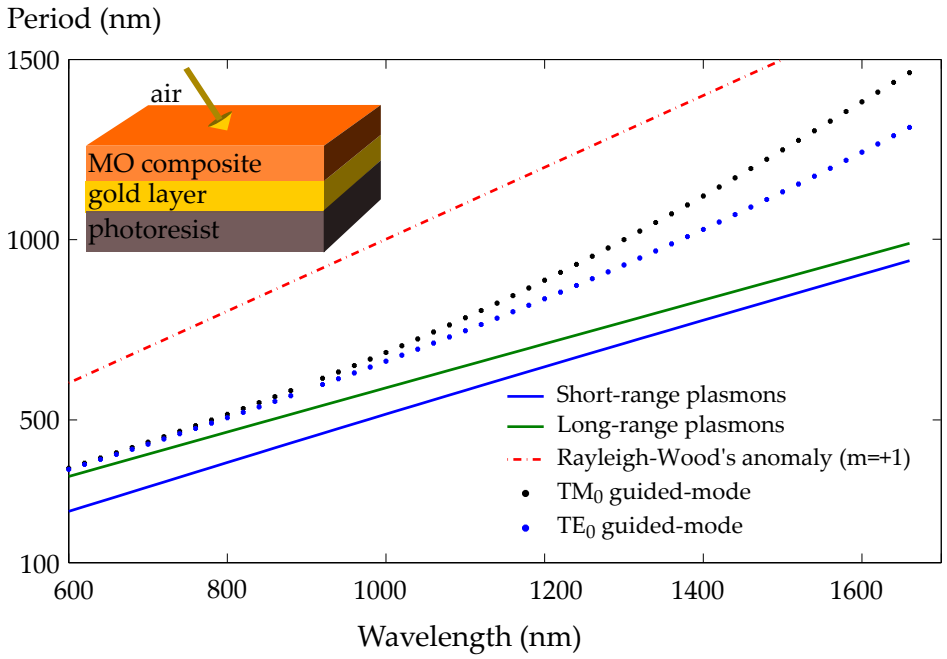

Figure 3.5: Simulation of various features of figure 3.4 for an equivalent magneto-plasmonic system (inset).

For TE-polarized light, only dielectric modes in the MO layer are excited whereas for TM-light, both plasmon and dielectric modes are excited. An EOT situation is clearly obtained for TM-polarization. Furthermore, the TE and TM resonances are more closely-spaced near the bottom-left of the graphs (corresponding to low grating periods and low wavelengths) than near the top-right (corresponding to high grating periods and increased wavelengths). Recalling that 750 nm of wavelength is also a MO area of interest (refer figure 1.4), this means the magneto-plasmonic grating fabricated for TMOKE measurements (with a grating period of 600 nm for an incidence angle of 80°), at the same time, lies close to fulfilling the phase-match condition for Faraday effect enhancement as well, for an incidence angle of 0°. Figure 3.6 shows the measured TE and TM transmittances of the prepared magneto-plasmonic structure. As the simulations predicted, the TE and TM resonances lie spectrally close to one another thereby lying close to the phase-match condition

(equation 1.33) for optimal polarization rotation. But, the only drawback of these resonances, apart from their very low efficiencies, is the fact that they occur in a spectral area ($\approx$ 900 nm) where the MO activity of our composite is not the strongest (refer figure 1.4). Nonetheless, there is a modification near the optical resonances of the FR for TM polarization (figure 3.6) compared to that of a homogeneous thin film. In this spectral area, FR should be negative, as measured on the homogeneous film. For the magneto-plasmonic device, the sign of FR passes from the negative to positive at 920 nm and 950 nm showing the impact of resonance on the MO spectrum. Such a behavior is not a huge enhancement, but it shows the ability of the device to modify the MO spectrum. To improve this behavior, the device parameters should be closer to that obtained from design: height of the grating, thickness of the MO layer. The latter is different on glass substrates than on metallic substrates, as the average MO effect is weaker from the device compared to the homogeneous film. To adapt such a thickness, the dip-coating speed has to be modified accordingly.

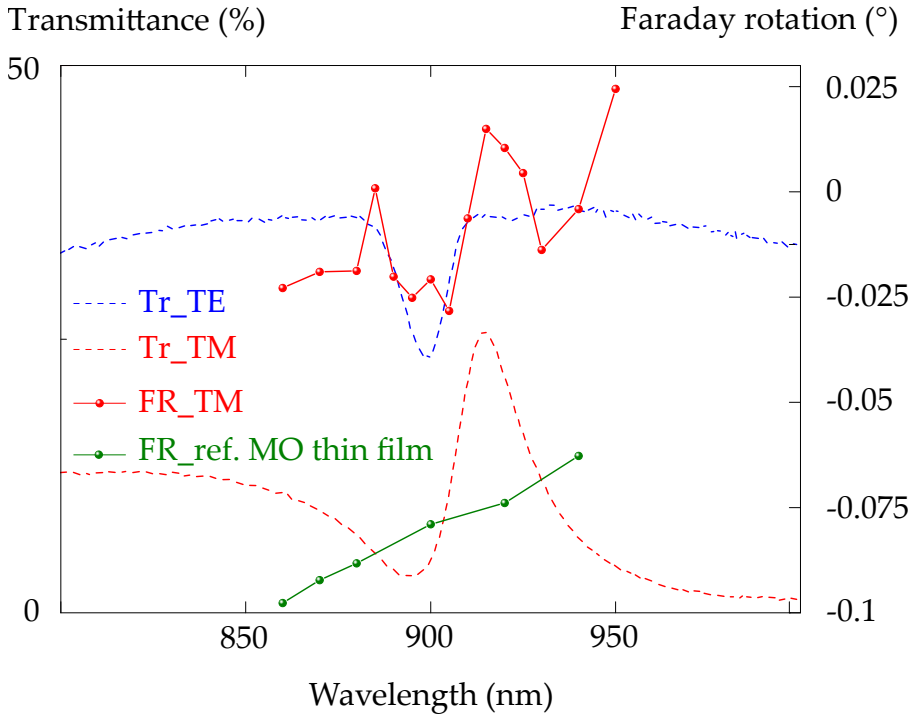

Figure 3.6: Measured transmittance (TE and TM) along with FR (TM) for the realized magneto-plasmonic grating and a reference MO thin-film.

This spectral modification of FR is a first demonstration that should be improved in the future. To reach such an improvement, the design has to be reviewed with the other targeted configurations. In fact, Floess *et al.* [138] have shown that the metal

position in the device has to be carefully chosen in order to obtain an adequate hybridization of TM mode between plasmons and guided-mode.

As exposed in chapter-1, the use of metals in photonic systems can be a bit challenging considering their high absorption. The following section presents the optical and MO behavior of 1-D all-dielectric MO gratings.

3.2 All-dielectric gratings

With all-dielectric MO structures, the condition to enhance MO properties remains the same: simultaneous excitation of TE and TM resonances for the enhancement of FR and other polarization effects (P/LMOKE), and a unique TM resonance for TMOKE. But contrary to magneto plasmonic structures, the TM resonance has to be from guided-modes only. Thus, it will not be possible to take benefit from the different dispersive behavior of TM plasmonic and TE dielectric mode. Considering this requirement and the challenge of physically realizing the proposed structures, two different kind of designs are finalized (figure 3.7). The first type involves two layers, a uniform MO layer followed by a periodically modulated grating layer atop it (named **design-A**), the other involves just a single layer with a spatial 1-D periodicity of our MO composite with an appropriate dielectric in the grating-voids (named **design-B**).

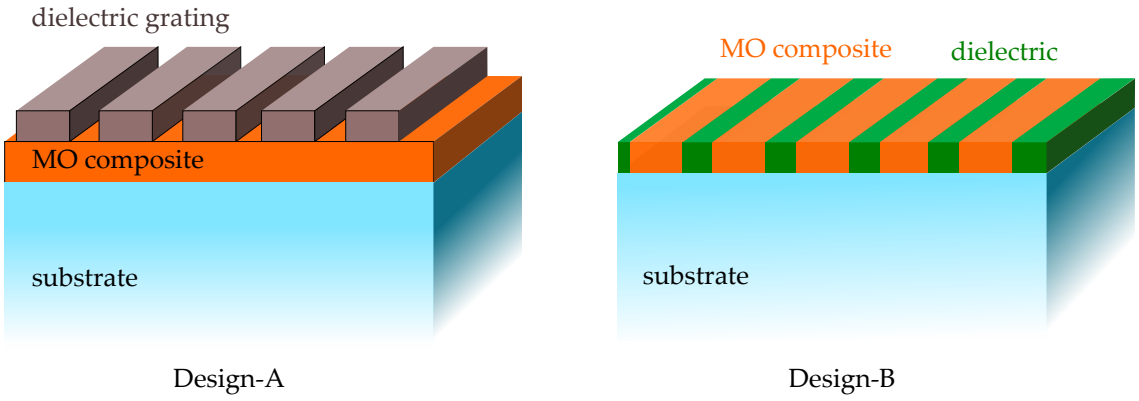

Figure 3.7: Proposed schematic of all-dielectric MO structures.

3.2.1 Design-A: grating on a MO layer

Of the two designs, gratings of design-A are relatively easy and inexpensive to fabricate. They involve first, depositing a thin-film of our MO composite onto a substrate such as BK-7 or pyrex followed by the deposition of a photoresist or a photopolymerizable sol-gel with subsequent photolithographic etching. However, fabrication of design-A structures do not offer flexibility in terms of the grating fill-factor. It is limited to 45%-50%. Because of its ease of fabrication and low cost, gratings of type design-A are more suited for practical applications such as non-destructive testing, for instance. Two structures are proposed with this design for target wavelengths of 750 nm and 1550 nm (refer figure 1.4) in transmission configuration for Faraday effect.

For 750 nm, figure 3.8(a.) shows a color map of transmittance as a function of grating height and incident wavelength for 0° incidence. The structure consists of a 500 nm periodic grating made with TiO_2-based photopolymerizable sol-gel. Table 3.1 presents rest of the parameters used in the simulations.

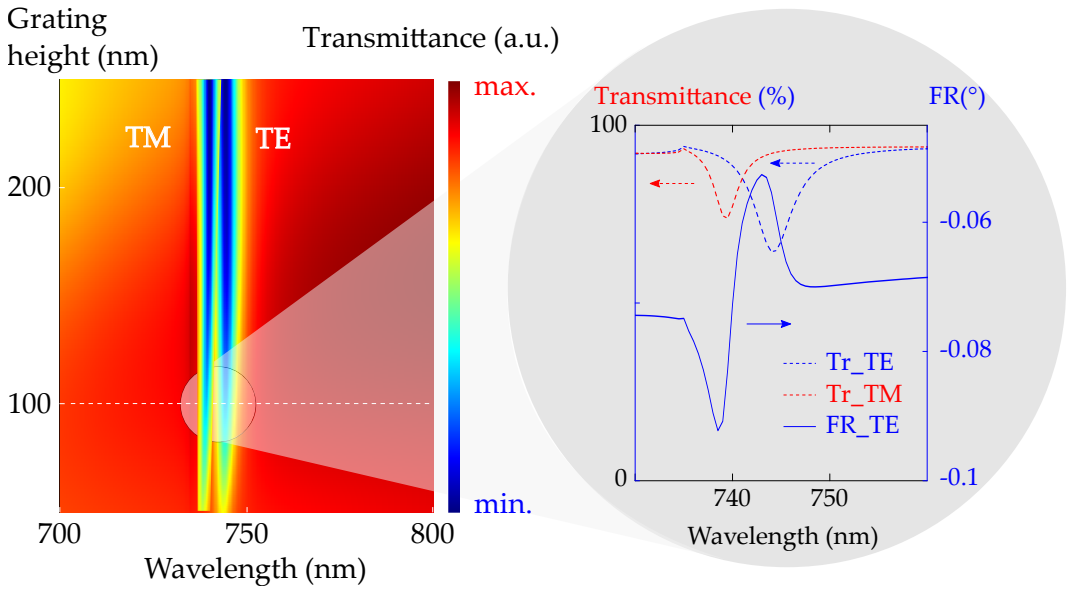

Figure 3.8: (a.) Simulated color map of transmittance (TE, TM) as a function of incident wavelength and grating height. (b.) Simulated transmittance (TE, TM) and FR (TE; right) for a structure with period of 500 nm and grating height of 100 nm. The rest of the parameters are listed in table 3.1

.

Parameter	Value
Grating period	500 nm
Grating refractive index	$1.51 + i0$ (w/o dispersion)
Grating fill-factor	50%
MO thickness	340 nm
MO concentration	10%
MO refractive index	$1.57 + i0.008$ (w/ dispersion)
Substrate refractive index	$1.47 + i0$ (w/o dispersion)

Table 3.1: Parameters used in the simulation of figure 3.8(a.).

As evident from the figure, the structure is capable of exciting both TE and TM guided-modes very close to one another with better results towards higher grating heights. Keeping realization in mind, figure 3.8 (b.) shows the spectral transmittance (left) for 100 nm grating height. The TM and TE optical resonances present efficiencies of 20% and 30%, respectively with a mutual separation of 5 nm. FR, simulated on the same structure, also demonstrates a resonant modification at these wavelengths (figure 3.8(b.)) as a result of this narrow separation. The rotation reaches -0.09° at 740 nm and -0.05° at 742 nm whereas, the off-resonance value is about -0.07°. The modification is seen for both TE and TM polarizations and even for Faraday ellipticity (not shown here for clarity).

Similarly, for 1550 nm, figure 3.9 (a.) shows a color map of TE and TM transmittance as a function of grating height and incident wavelength at 0° incidence with rest of the parameters listed in table 3.2. The period is fixed at 1000 nm to work around a wavelength of 1550 nm.

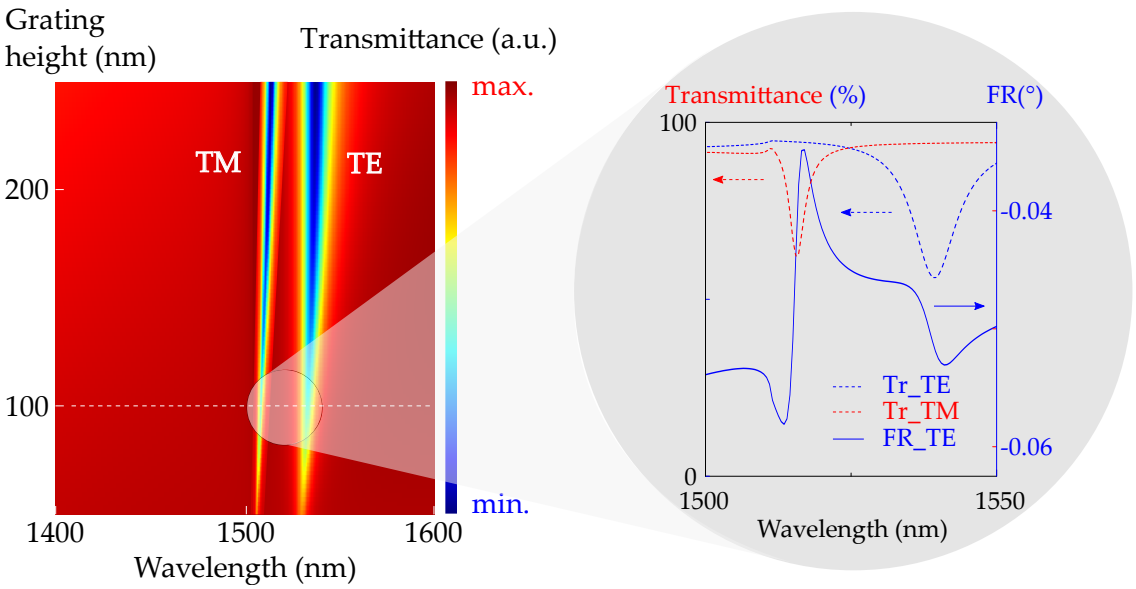

Figure 3.9: (a.) Simulated color map of transmittance (TE, TM) as a function of incident wavelength and grating height. (b.) Simulated transmittance (TE, TM; left) and FR (TE; right) for a structure with a period of 1000 nm and grating height of 100 nm. The rest of the parameters are listed in table 3.2

Parameter	Value
Grating period	1000 nm
Grating refractive index	$1.63 + i0$ (w/o dispersion)
Grating fill-factor	50%
MO thickness	420 nm
MO concentration	22%
MO refractive index	$1.70 + i0.005$ (w/ dispersion)
Substrate refractive index	$1.47 + i0$ (w/o dispersion)

Table 3.2: Parameters used in the simulation of figure 3.9.

Here also, the structure shows closely spaced TE and TM resonances with efficiencies that increase with the grating height. Figure 3.9 (b.) shows the spectral

transmittance (left) for 100 nm grating height. Both resonances show an efficiency of around 40% with a mutual separation of 24 nm. Due to this closeness, a resonant modification of the FR occurs at both the spectral positions of TE and TM resonances.

The structures proposed above show promise with respect to Faraday effect enhancement but, due to poor structural quality of the realized samples, an equally good effect could not be achieved experimentally. Figure 3.10 shows the optical and MO response for a structure based on figure 3.9. The gratings of this structure were made with the same photoresist material used for magneto-plasmonic samples. The structure could excite TE and TM resonances with 17% and 7% efficiency, respectively with a mutual separation of 21 nm. Consequently, a very small modification of FR and ellipticity for TM polarization was visible resembling the simulations.

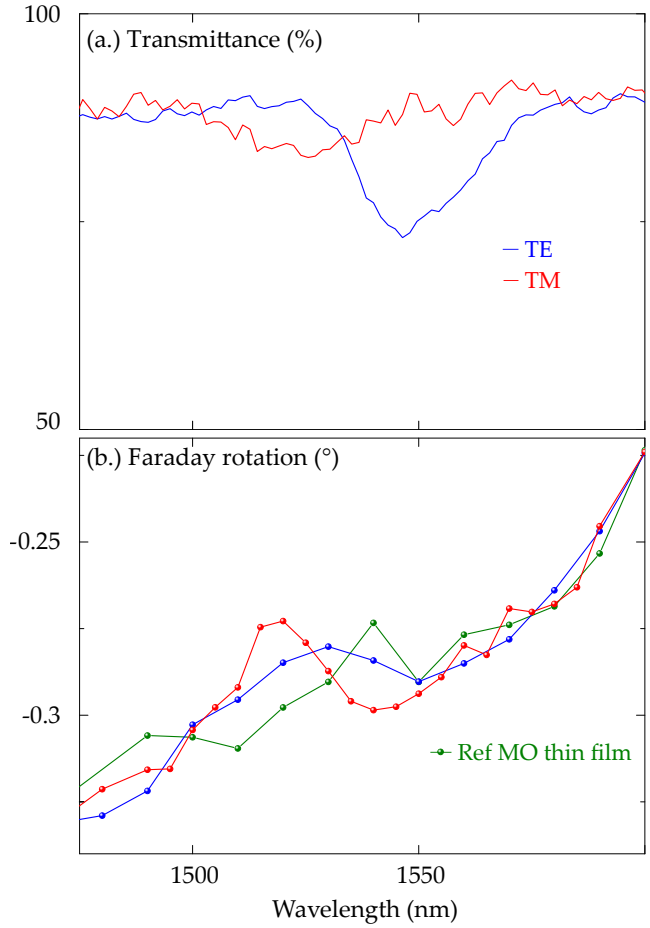

Figure 3.10: Measured transmittance (a.) and FR (b.) for MO structure of design-A.

These above presented structures show good potential to enhance MO effects for an all-dielectric structure with TE/TM resonances reaching 70% efficiencies at

grating heights close to 250 nm. Practically, this was a little difficult to realize thus, limiting the efficiency of the fabricated structure. Nevertheless, even a slight modification of the spectra represents the capability of the structure to perform better. In addition to remarking a grating height influence on the transmitted efficiency, it was observed that samples of type design-A fabricated on pyrex substrates performed a little better than the ones prepared on BK-7 substrates.

Continuing with the analysis of all-dielectric MO gratings, let us focus on the performance of MO structures of type design-B.

3.2.2 Design B: impregnation of templates

The objective to realize such MO structures is to start with a template structure of high quality so that the region under illumination, unlike in the above case, is well homogeneous. Two different materials were used to realize such a design, titanium dioxide and silicon nitride. They were decided based on their refractive index contrast with our MO composite.

MO gratings with TiO_2:

TiO_2 templates were fabricated using sol-gel technique and photolithography on BK-7 substrates (refer [139] for details). They were the first structures to be analyzed in this work. These templates were impregnated with our MO composite having a NP concentration of 1% which provided a refractive index contrast of 0.26 at 1550 nm and 0.29 at 750 nm (see table 3.3). The period of the structure was 970 nm with a grating height of 315 nm and a fill-factor close to 50%. Figure 3.11 shows its transmittance simulated and experimentally measured in the infrared region for 0° incidence. A TE resonance with 50% transmission efficiency at 1500 nm can be evidenced. However, the structure was incapable of exciting TM resonance at 0° unless it was an oblique incidence.

Material	Refractive index	
	750 nm	1550 nm
MO composite (1%)	1.45+i0.005	1.44+i0.004
TiO_2	1.74+i0.004	1.71+i0.002

Table 3.3: Refractive indices for MO composite (1%) and TiO_2 at 750 nm and 1550 nm.

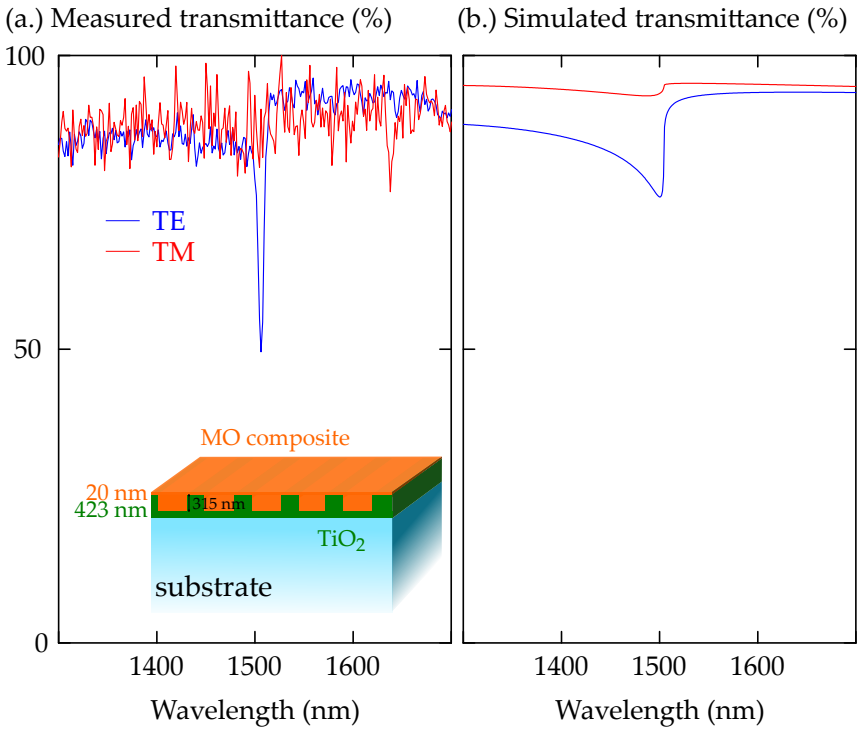

Figure 3.11: Transmittance measured (a.) and simulated (b.) of TiO_2-based MO structure (inset) at normal incidence.

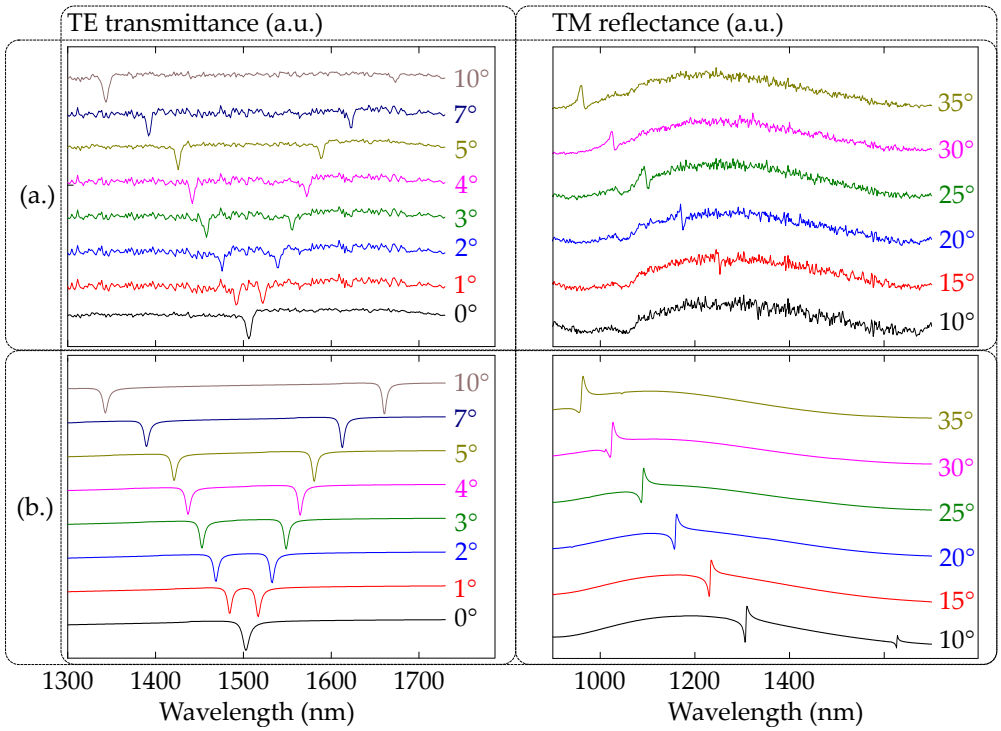

Figure 3.12: Experimental (a.) and simulated (b.) angle variation of TE transmittance (left) and TM reflectance (right) for a TiO_2-based MO grating.

Figure 3.12 confirms the excitation of TE and TM guided modes in the waveguide-grating layer with an angle variation of TE transmittance and TM reflectance. Each curve in the figure is normalized from 0 to 1 and vertically stacked with an offset. These resonant dips/peaks are well coherent with the grating equation 1.33 confirmed by the simulations. Using the measured data for TE transmittance (figure 3.12(a.)), the effective-index of the guided-mode is calculated to be 1.68, which is coherent with the effective index values of the materials employed.

However, due to the lack of simultaneous TE/TM resonance at 0° and limitations of the MO setup to measure Faraday effect at high oblique incidence (where TE and TM resonances both exist), no Faraday enhancement was observed. Also, the refractive index contrast in grating region was low to achieve notable efficiencies. This could be varied by changing the concentration of NPs in the MO composite. Furthermore, simulations showed that increasing the grating height from 315 nm to 600 nm can lead a much higher transmission efficiencies. The results of TiO_2-based MO structures concludes two points: first, both TE and TM resonances should be efficiently excited by the structure and second, the structures need to be impregnated with high enough concentration of $CoFe_2O_4$ NPs.

All of the above mentioned factors were taken into account to make a MO structure with silicon nitride.

MO gratings with Silicon nitride (Si_3N_4):

Structures of type design-B with silicon nitride ($n_{Si_3N_4} = 1.931 + i0$) presented a refractive index contrast with 15% doped MO composite ($n_{MO} = 1.606 + i0.005$) of 0.325 at 1550 nm (see figure 3.13(a.)). The substrate considered was BK-7. To obtain a resonance at 1550 nm with the given refractive indices and an incidence angle of 0°, the grating period Λ was fixed at 950 nm. Such a grating period is attainable by fabrication and results in a sub-wavelength grating: only the zeroth-diffraction order would exist in the substrate and the upper cover of air. Other physical parameters of the grating structure were determined based on their ability to simultaneously excite guided-modes for TE and TM polarizations. These adjustable parameters were the height h of the grating and the line-space ratio (l/s), line l being the width of Si_3N_4 and, space s being the width of the MO material. Alasaarela *et al.* [64] showed that a proper choice of these two parameters can lead to a polarization-independent resonance situation. Figure 3.13(b.) shows the conditions

to obtain TE and TM resonances at 1550 nm as a function of these two parameters: h and l. The intersection point of the two curves determine the desired values of the grating height and the line-space ratio of the structure to be realized.

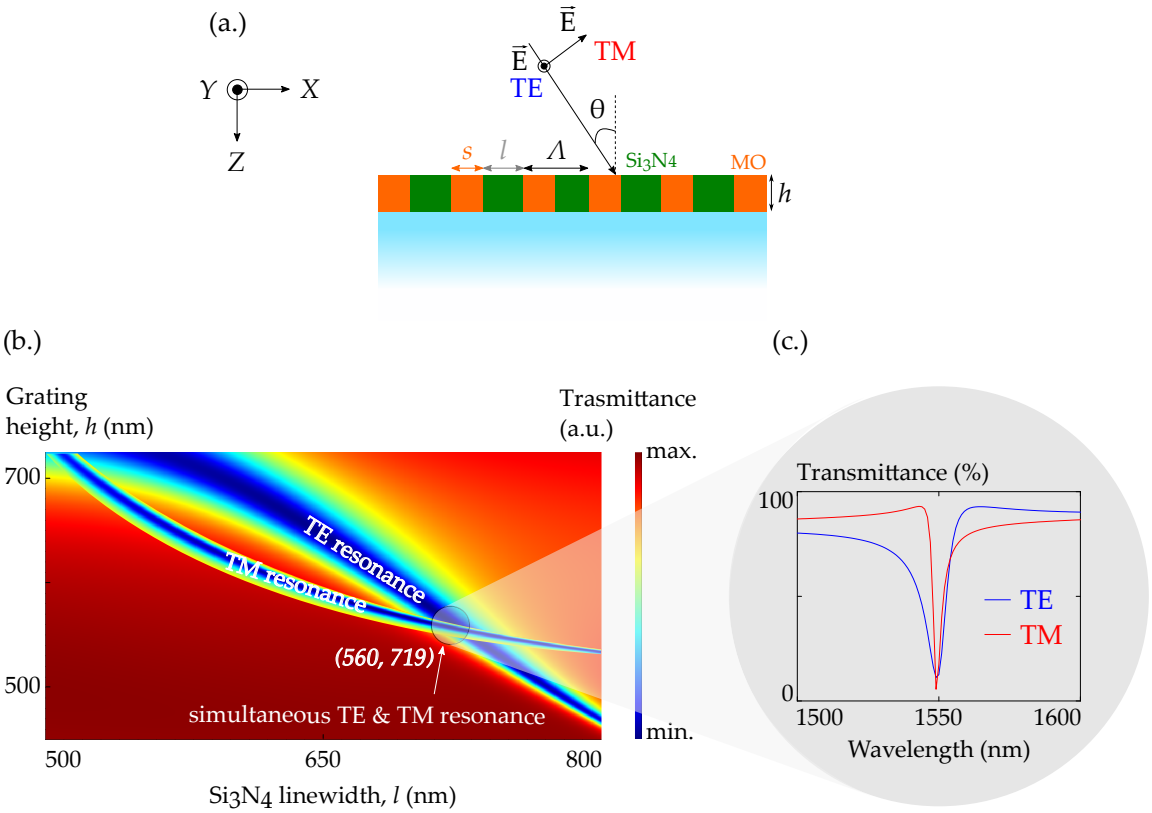

Figure 3.13: (a.) Color map of transmittance as a function of Si_3N_4 linewidth and grating height. (b.) Transmittance for a Si_3N_4 based MO structure using the intersection parameters.

Parameter	Transmittance	
	TE	TM
FWHM	7 nm	3 nm
λ_r	1549 nm	1549 nm
efficiency	79.8%	84.4%

Table 3.4: Characteristics of TE and TM resonances presented in figure 3.13(c.)

These parameters were $h = 560$ nm, $l = 719$ nm and $s = 231$ nm. Simulated transmittances for the structure based on these parameters are reported for both

polarizations in figure 3.13(c.). For both the polarizations, the resonance manifests itself by a dip in transmittance, going down from 80% (outside resonance) to 10% (at resonance) around 1550 nm. Table 3.4 lists the optical features of both the resonances.

But, the shape of these transmittance curves around the dip show a different behavior for TE and TM polarizations, with a narrower resonance for TM. This dip in transmittance was associated with a corresponding peak in the reflection spectrum which reaches 80% at resonance (not shown here).

Figure 3.14 shows a simulation of transmittance (T), FR (θ_F) and Figure of Merit (FoM: $\sqrt{T} \times \theta_F$) for this structure. In figure 3.14(b.) is also reported the FR calculated on a reference MO thin film with an identical thickness to that of the grating (h= 560 nm) on a BK-7 substrate. The obtained value is 0.15° at a wavelength of 1550 nm according to equation 1.11 for such a layer.

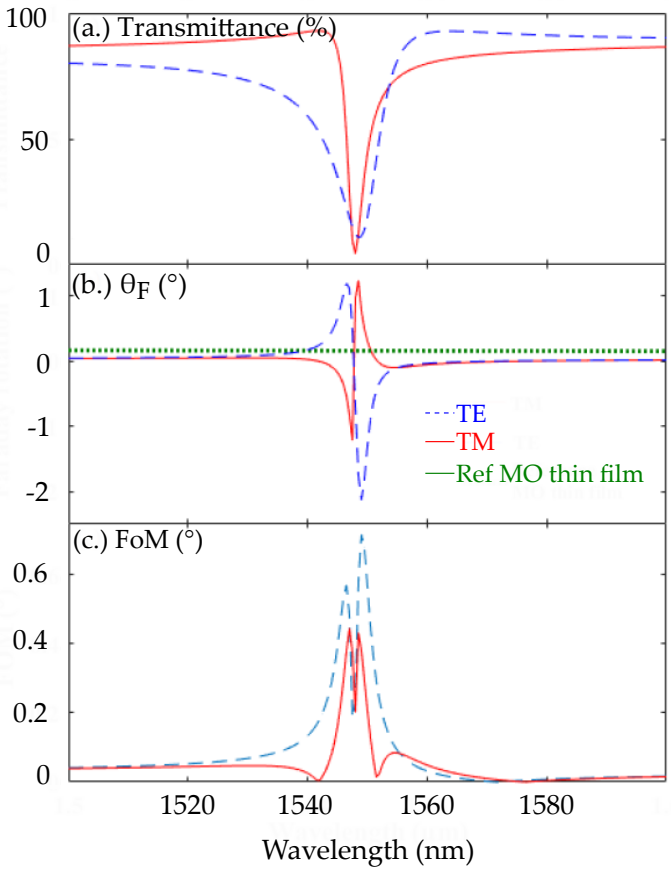

Figure 3.14: (a.) TE (dashed line) and TM (solid line) spectral transmittances. (b.) Corresponding simulated FRs and simulated FR for the reference thin film (dotted line). (c.) Figure of Merit for both polarizations.

Analyzing figure 3.14, the spectral behavior of FR evidences a large enhancement through the presence of large opposite peaks on both sides of the resonance for both polarizations. For TE polarized light, Faraday effect reaches -2° of rotation on the long-wavelength side. One can see that the enhancement of FR is better for TE than TM polarization, even if the resonance is less sharp. On one hand, comparing this value of 2° to the "off-resonance" value of 0.027°, a gain as large as 100 is evident. So, a MO sensor, for instance, based on this kind of structure would take a large advantage of such an enhancement in terms of its sensitivity. It is worth noting that the off-resonance value is weaker than that of the reference layer because it contains rather less MO material, which is present only inside the slits of the Si_3N_4 grating. On the other hand, the drawback is that the spectral position of this maximum coincides with the minimum of transmittance which is close to 7%. Regardless, in the case of a sensor, it is not always required to have a high optical intensity, but it may be the case for other applications. Thus, it is relevant to analyze the trade-off between the signal intensity and the FR through its FoM. Its off-resonance values are respectively, 0.02° and 0.016° for TE and TM polarization. It is obvious that the FoM is really enhanced at the two edges of the resonances reaching 0.7° for TE polarization and 0.4° for TM polarization. The FoM is multiplied by a factor of about 30 compared to the off-resonant values. The maximum value obtained here can be compared to that of Lei *et al.* [9] who numerically demonstrated a FoM of 0.75° with a more complex structure made of 2-D dielectric/metallic nano-antennas on a BIG film, which employs an extraordinary optical resonance. Belotelov *et al.* [85], numerically demonstrated a 0.48° FoM with a 2-D metallic grating on a BIG substrate, and Chin *et al.* [91] experimentally evidenced a FoM of 0.48° with a 1-D sub-wavelength metallic grating on a BIG film. Caballero *et al.* [11] numerically obtained values less than 0.01° with 2-D metallic/ferromagnetic perforated membranes. Finally, the 0.7° of FoM demonstrated here is, to the best of our knowledge, one of the highest reported and obtained on a 1-D grating which can be easily fabricated. Furthermore, compared to the other works cited [9, 11, 85, 91] which employ a metallic material, this result is obtained with an all-dielectric 1-D grating. Besides Faraday effect, other magneto-optical effects such as Kerr effects have also been studied on this structure around the resonance area.

The PMOKE and LMOKE are both calculated for a 1° incidence, LMOKE being null at normal incidence. Recalling that for PMOKE, the magnetic field direction is identical to that in Faraday configuration (along Z-axis), whereas for LMOKE its

direction is along X-axis. For both effects, the analysis of the polarization modification is led in reflection configuration, for TM polarization. As illustrated in figure 3.15(a), the optical resonance manifests itself through the presence of an asymmetric Fano-type reflectance (R) peak. One can see that the presence of the resonance drastically modifies the spectral MO response for both effects, which are widely enhanced on both sides of the resonance. The polar and longitudinal Kerr rotation peaks reach respectively 14° and -12° which compared to "off-resonance" values leads to an enhancement of 700 and 105, respectively (figure 3.15(b)). Here also, the drawback is that the position of the maximum of Kerr rotation (θ_K) coincides with the weakest value of reflectivity. But, in terms of Figure of Merit ($\sqrt{R} \times \theta_K$), the enhancement is huge: from $10^{-4\circ}$ (0.007°) outside the resonance to 0.5° (0.4°) at the resonance for longitudinal (polar) effect (figure 3.15(c)).

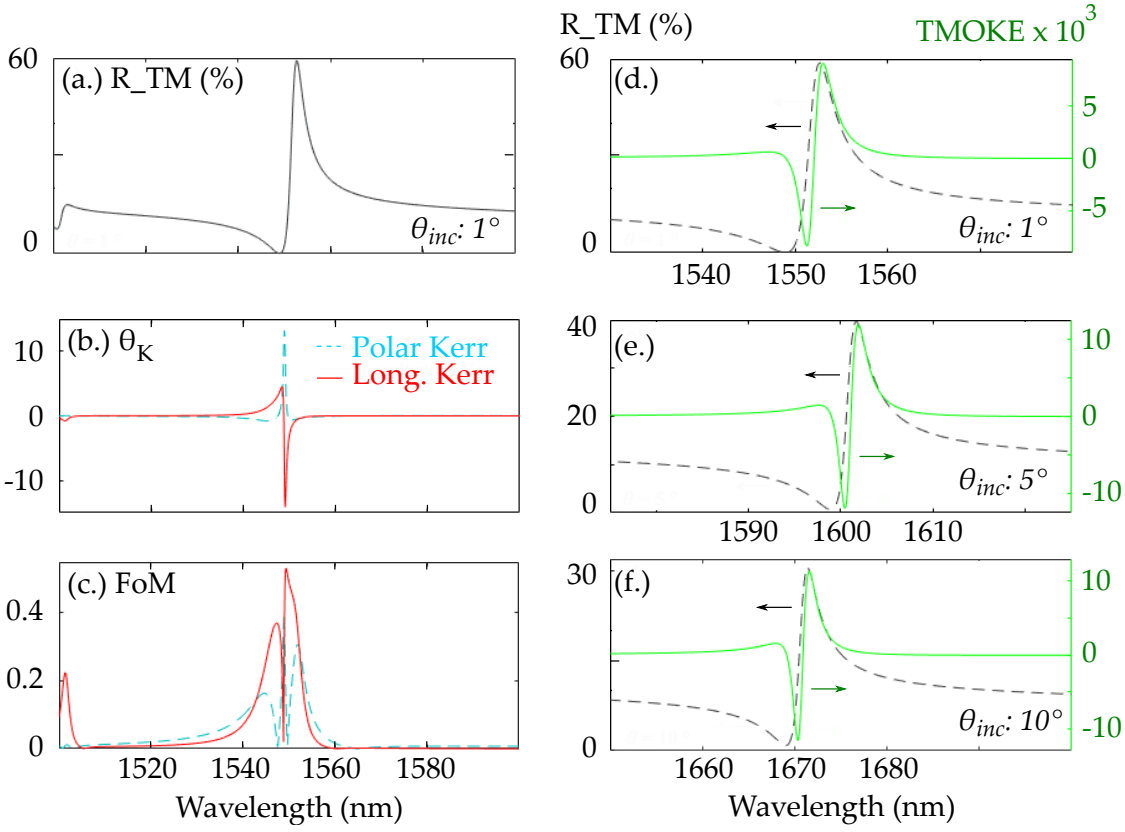

Figure 3.15: (a.) TM spectral reflectance for 1° incidence. (b.) Corresponding polar and longitudinal Kerr rotations and, (c.) Figure of Merit. (d, e, f) Spectral TMOKE and corresponding reflectance for 1°, 5° and 10° incidence, respectively.

In the case of TMOKE, the magnetic field is oriented along Y-axis and involves no coupling between the TE and TM polarization and thus, no magnetically-

induced polarization rotation. Figures 3.15 (d.), (e.) and (f.) demonstrate simulated TMOKE for the structure as a difference between the reflectance spectra obtained for opposite directions of the induced magnetization: $R_{(+Msat)} - R_{(-Msat)}$. As it is null at zero incidence, it is calculated for 1°, 5° and 10° incidence. Such low values of incidence angle guarantee good reflectivity. One can notice, for each angle, the presence of two opposite peaks in the TMOKE spectra with a maximum value of 1.2×10^{-2} at 5° of incidence. Contrary to Faraday effect and LMOKE/PMOKE, the enhanced value is obtained for one peak with an intensity of signal which is high (58% at 1° and 40% at 5°). As a comparison and using the previous definition of TMOKE ($R_{(+Msat)} - R_{(-Msat)}$), the enhanced value reported here is of the same order as that measured by Pohl *et al.* with a 1-D gold grating on top of a BIG layer (7.8×10^{-3}) [23]. This layer possesses a magneto-optical activity given by a permittivity with an off-diagonal element of 0.0085. On the same kind of structure, Halagačka *et al.* numerically obtained a giant effect as large as 0.5 with an off-diagonal element of 0.1 [101]. For all-dielectric structures, Maksymov *et al.* evidenced through numerical simulations, a TMOKE of 4×10^{-2} with an off-diagonal element of 0.005 [8]. And, Caballerro *et al.* numerically demonstrated a TMOKE value of 4×10^{-3}, using 2D magneto-plasmonic membranes with a high sensitivity of this TMOKE effect to the surrounding medium [11]. Our results show that even if we are using an off-diagonal element with a weak value (0.0037), and even if the structure has not been optimized for TMOKE but for Faraday effect, the enhanced TMOKE value is of the same order as that reported in literature.

The obtained results show that it is possible to obtain an enhancement of four MO effects with the same structure. In the context of magnetic sensors, such a structure gives the possibility to access, at least, two different components of the magnetic field: one component from the modification of the reflectivity (TMOKE), and the other one from polarization rotation (Faraday, P/LMOKE). Nevertheless, if we consider only the three effects leading to a polarization rotation, it is evident that the maximum of rotation is obtained for small values of the corresponding diffraction efficiency. Now, we will focus only on Faraday effect.

By changing the incidence angle, it is possible to shift the spectral position of both TE and TM resonances separately. The computed TM FRs for 1°, 5° and 10° are plotted in figures 3.16(a.), (b.) and (c.), respectively. In the case corresponding to a 5° incidence for TM polarization (figure 3.16(b.)), a FR of 0.15° is obtained for a value of transmittance as high as 82%. This gives a possibility of the structure

to present a good transmittance as well as an enhanced MO effect. At 1° and 10° incidence (figure 3.16(a.) and 3.16(c.), respectively), the same kind of behavior can be also remarked but, with smaller FRs. The spectral modification of the rotation is thus preserved for all the resonances, the native polarization (here TM) but also the opposite one (i.e. TE). Nevertheless, despite a FoM (see figure 3.16(d)) that is lower than that at normal incidence, i.e. at the phase-matching condition in our case, one can see that it is possible to obtain an enhancement of the rotation at a wavelength where the transmittance is close to 80%. Working at this level of transmittance can be really interesting for the development of sensors, for instance. The Faraday effect in this kind of structure could be enhanced by using a material with a larger off-diagonal term which is possible with our MO composite by using a larger amount of NPs in the sol-gel. The narrowness of the resonances gives rise to spectral modifications with a FWHM of a few nanometers. This is less than what could be obtained using magneto-plasmonic structures [9], but it is larger than what is expected for a 2D all-dielectric grating as demonstrated by Bai *et al.* [90].

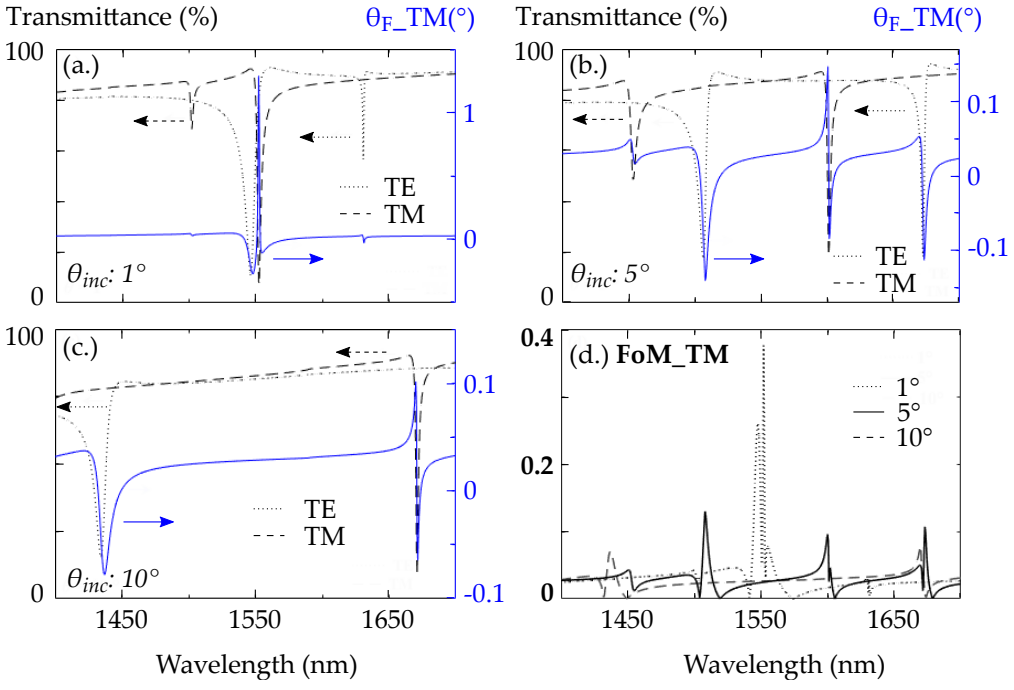

Figure 3.16: (a) TE (dotted line) and TM (dashed line) spectral transmittances and corresponding TM FRs for (a) 1°, (b) 5°, (c) 10° incidence. (d) Figure of Merit for the three incidence angles.

The above simulations show that it is possible to enhance four MO effects using a single 1-D all-dielectric resonant grating. The structure was optimized for Faraday

effect, thus in transmission at normal incidence. An achievement of a phase-match between TE and TM modes was the basis of the opto-geometrical design. The enhancement of TMOKE was not optimized but showed an order of magnitude comparable to that obtained in literature. To achieve an enhancement of TMOKE, the design strategy should be to obtain a TM resonance with a high efficiency.

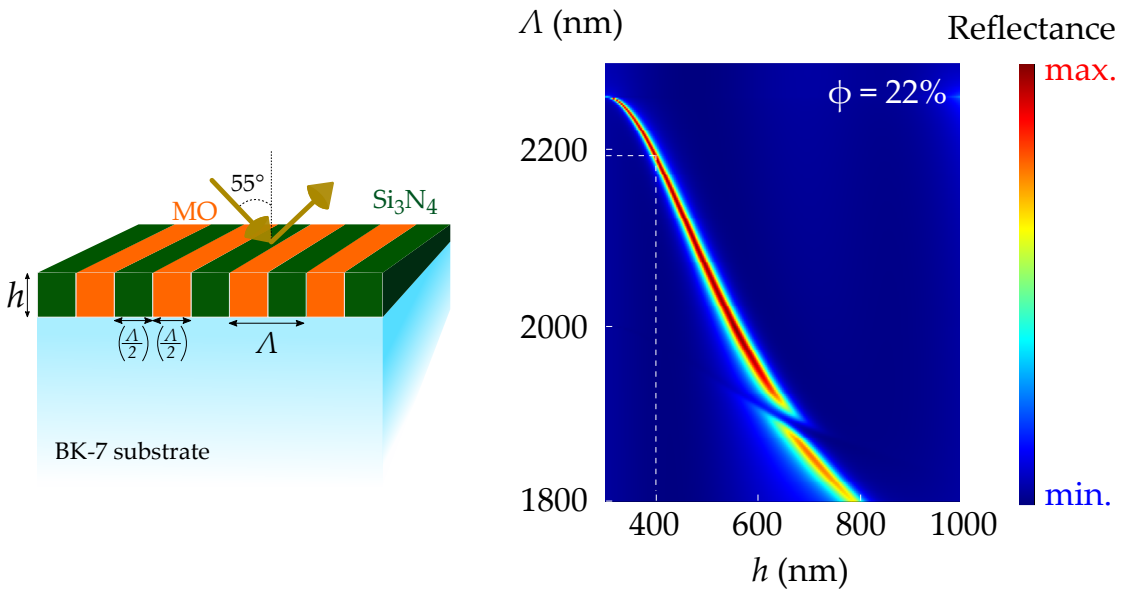

Figure 3.17: Color map of reflectance for Si_3N_4 structure at 55° incidence for TM-polarized light.

Figure 3.17 shows a color map of reflectance at 1550 nm as a function of grating period (Λ) and height (h) for an angle of incidence of 55°. The structure is the same as before with silicon nitride and MO composite, but the fill factor is fixed at 50% and the concentration is a bit higher (22%). This color map evidences that a large TM resonance takes place. As illustrated in figure 3.18, when the period and height are respectively, fixed at 2190 nm and 400 nm, the reflectance varies from 0 to 40%, whereas the transmittance varies from 90% to 15% at the resonance position. Such TM resonance gives rise to an enhancement of TMOKE which reaches 0.014 in reflectance (figure 3.18(a.)). This is higher than that obtained at 5° on the previous device designed for Faraday enhancement. And, in transmission mode, the TMOKE is even higher with a maximum value of 0.018 (figure 3.18(b.)). This last value is of the order demonstrated by Maksymov *et al.* [8], but in our case, the off-diagonal element is weaker, and the resonance is not as narrow as they demonstrated.

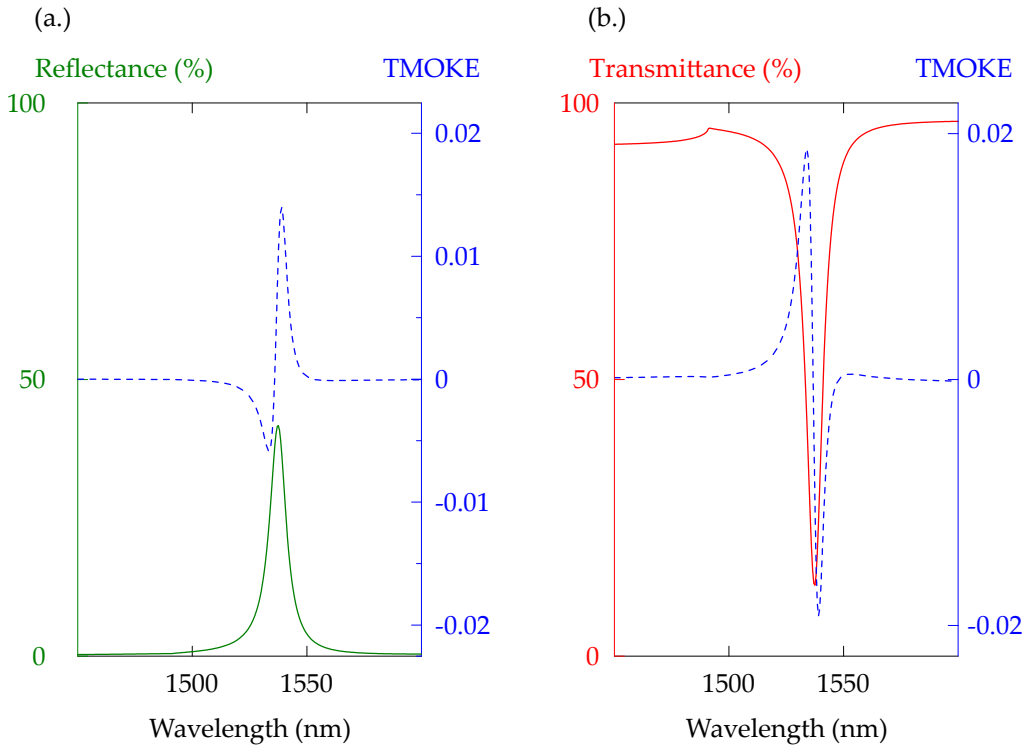

Figure 3.18: Reflectance (a.) and transmittance (b.) with corresponding TMOKE for θ_{inc}=55° for a structure having a period of 2190 nm with a grating height of 400 nm.

This numerical study on design-B structures with silicon nitride has shown a great potential of such devices to enhance every MO effect. The next section is thus dedicated to the experimental analysis of this kind of devices.

3.3 Experimental evidence of MO enhancement

In order to experimentally demonstrate a MO enhancement in an all-dielectric 1-D structure, the structure simulated and detailed in the previous section had been fabricated. This targeted structure was a 1-D periodic grating constituting alternatively of silicon nitride ($n = 1.93 + i0$) and MO composite ($n = 1.606 + i0.005$) with a period of 950 nm on a BK-7 substrate. The elaboration strategy was to start from a Si_3N_4 grating template which would be then dip-coated in a NP doped sol-gel solution in order to fill the grating slits with the MO composite. In order to fulfill the requirements of simultaneous TE and TM resonances, thickness of the template would have to be adjusted at 560 nm with a Si_3N_4 line width of 719 nm.

3.3.1 Description of samples

Fabrication of the Si_3N_4 grating template was subcontracted to the University of Joensuu (Finland). The first step was the deposit of silicon nitride on BK-7 substrates. Then, electron beam lithography and reactive ion etching were performed to obtain the template. Compared to the fabrication of previous gratings based on classical coating and photolithography, this elaboration method was more complex and expensive. It can not so easily be applied to an industrial process, but it ensures a very good homogeneity of the pattern over the 5×5 mm surface of the device.

However, manufacturing tolerances did not yield the targeted geometric characteristics given above. But different templates had been realized whose geometrical characteristics are summarized in the following table:

Sample	Grating period (nm)	Si_3N_4 thickness (nm)	Grating depth (nm)	Line width (nm)
S0	951	593	576	320
S3	966	593	623	608
S5	966	593	612	531
S6	966	593	617	502
S7	966	593	583	580
S8	966	593	611	521

Table 3.5: Structural characteristics of Si_3N_4-based MO gratings realized for this work.

Each sample was characterized for its grating period using the Littrow configuration setup. Even if the parameters did not match with the targeted ones, different samples were selected to be impregnated by the magnetic material. This selection was based on simulations of the different gratings with our MO material filled in the slits and variation of the refractive index of our MO composite. In fact, as detailed in the previous chapter, the refractive index of our composite depends on the concentration of $CoFe_2O_4$ NPs, which can be tuned at the sol doping stage. The aim was to identify those structures which when filled with our MO material allows a coincidence of TE and TM resonances. This was done for samples S0, S3 and S6, which were then dip-coated with the appropriate sol-gel solution.

In the following paragraphs, the results related to sample S3 will be mainly detailed. For this sample, the best choice was a refractive index of 1.61, i.e. a NP

volume fraction of 15% in the silica host matrix. The schematic of the final sample is given in figure 3.19(a.) along with the refractive indices of the Si_3N_4 and our MO composite (figure 3.19(b.). Theses indices had been measured by ellipsometry on reference films. These curves indicate that the refractive index of the MO composite (1.69 at 1550 nm) is higher than expected. Such difference can be explained by the method employed to calibrate the NP volume which is based on FR measurements led on films during the doping. Evidently, even if the FR value indicates a volume fraction of 15%, the final refractive index obtained corresponds much more to 22%. This shows that the doping process is not so repeatable.

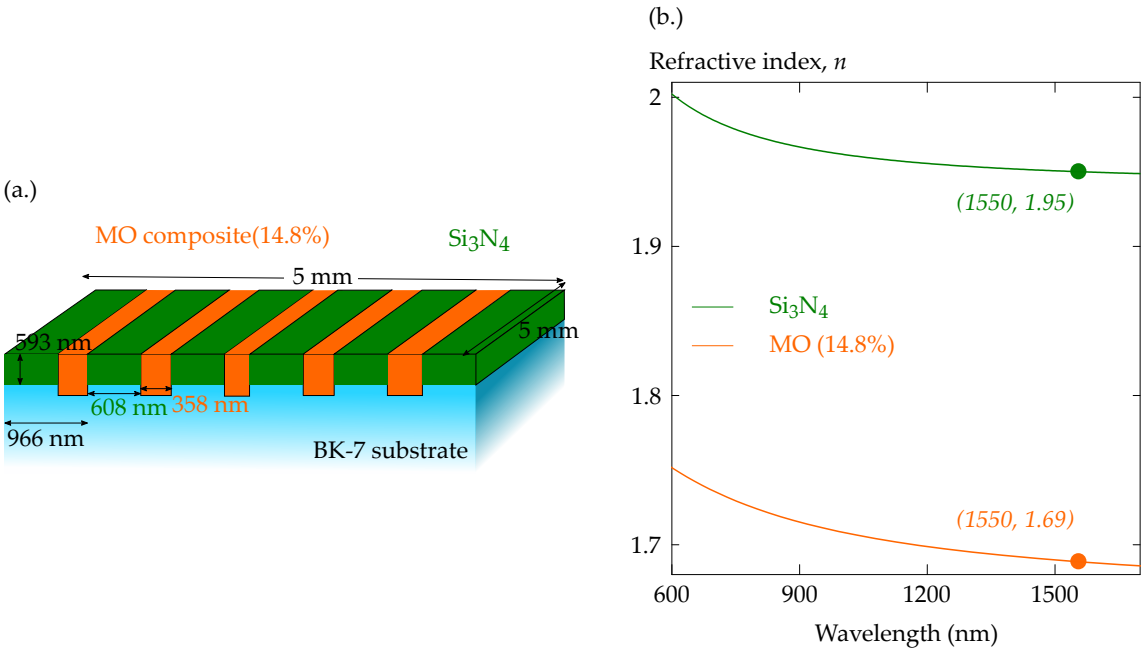

Figure 3.19: (a.) Schematic of sample S3. (b.) Measured spectral refractive index for Si_3N_4 and MO composite (14.8%).

Finally, the obtained all-dielectric MO grating described in figure 3.19 was carefully characterized and its optical and MO properties are detailed in the following sections.

3.3.2 Optical characterization

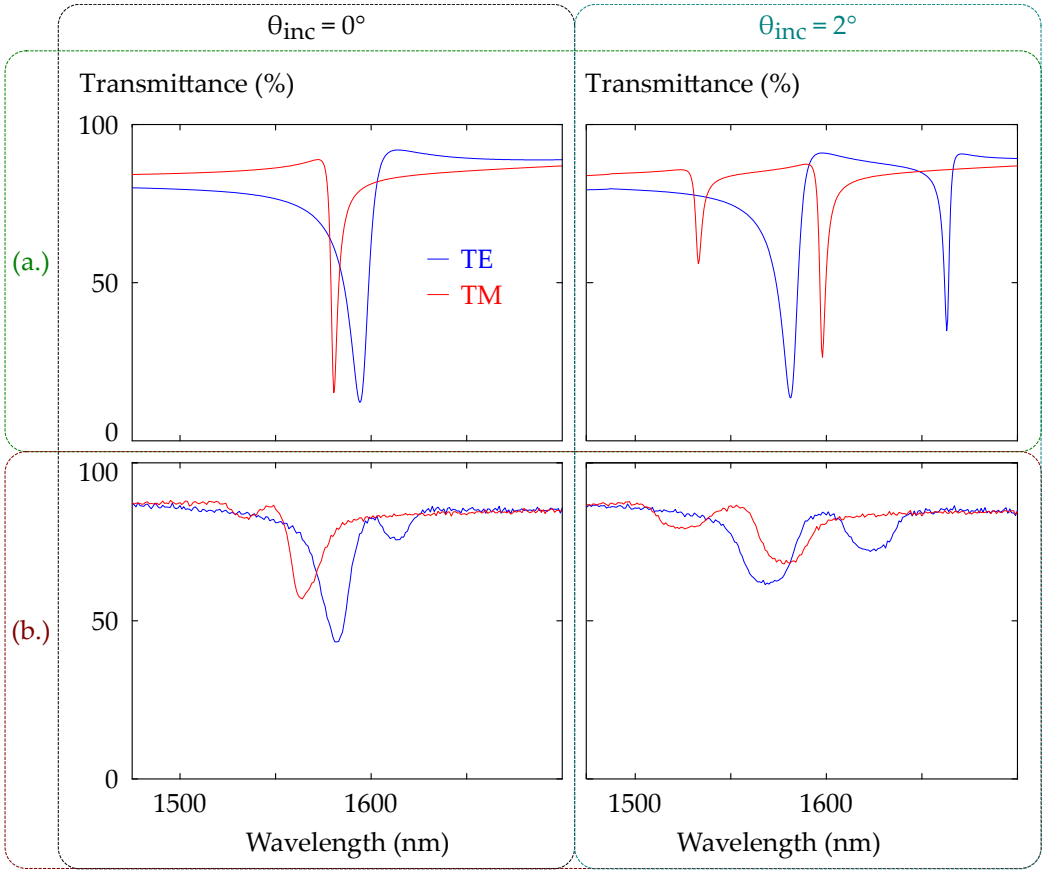

Figure 3.20: Simulated (a.) and measured (b.) TE and TM transmittances for sample S3 at 0° (left) and 2° (right) incidence.

Figure 3.20 compares the experimental TE and TM optical transmittances with the theoretical ones for normal and 2° incidence. One can see a good agreement between theory and measurements. The TE and TM resonances are very close to each other: 1572 nm (TM), and 1583 (TE), i.e. a mutual separation of 11 nm. Such a low separation should ensure the enhancement of MO effects. It can nevertheless be noticed that the narrowness of the theoretical dips (in TM, particularly) leads shallower and wider dips in practice. This can be explained by the imperfections of the MO gratings (surface condition, irregularities in the impregnation and in the geometrical characteristics). The resolution of the measurement (performed with a *Carry5000 spectrometer-Agilent Technologies*) close to 2 nm can also explain the measured depth of the dips.

3.3.3 Faraday effect

Figure 3.21 compares the experimental and simulated Faraday effects for TE and TM polarizations as well as the corresponding Figures of Merit for a normal incidence. A good agreement can be also noticed between experimental and simulated MO results, even if the spectral resolution of the MO setup is of about 10 nm (§ 2.3.2). Consistent with our hypothesis, simultaneous excitation of TE and TM resonances aides in the enhancement of Faraday effect. For TE polarization, the FR reaches 0.49° at 1579 nm, whereas it is -0.13° for the reference thin-film. In absolute terms, this rotation is multiplied by 3.5. As for the TM polarization, the resonance produces a sign inversion of FR as well as the ellipticity (figure 3.22), which is more specifically illustrated in figure 3.22(c.), through a plot of the magnetic behavior of the effect at two specific wavelengths. Concerning the TE Figure Of Merit, its maximum value is 0.31° on both sides of the resonance. This value has to be compared with 0.7° obtained on the simulated targeted device presented in the previous section. As the TE and TM optical resonances do not exactly match, the MO enhancement is not maximum. Comparing experiments with simulations in figures 3.21 and 3.22, one can notice that the shape of the curves as well as the amplitudes of the effects are respected. For FR, it can also be noticed that the measured effects are quite higher in TM and shifted slightly in wavelength. These remarks can of course, be transposed to the Figure of Merit's curves. The fact that the effects are more marked in simulation for TM can be explained by the width of the corresponding experimental transmittance dip in TM which is wider than in theory. Thus, the overlap of the 2 curves is therefore better, which could explain a greater enhancement of the rotation. This should be true also for the TE FR, but the narrowness of the dip can explain that the measured FR is close to the simulated one.

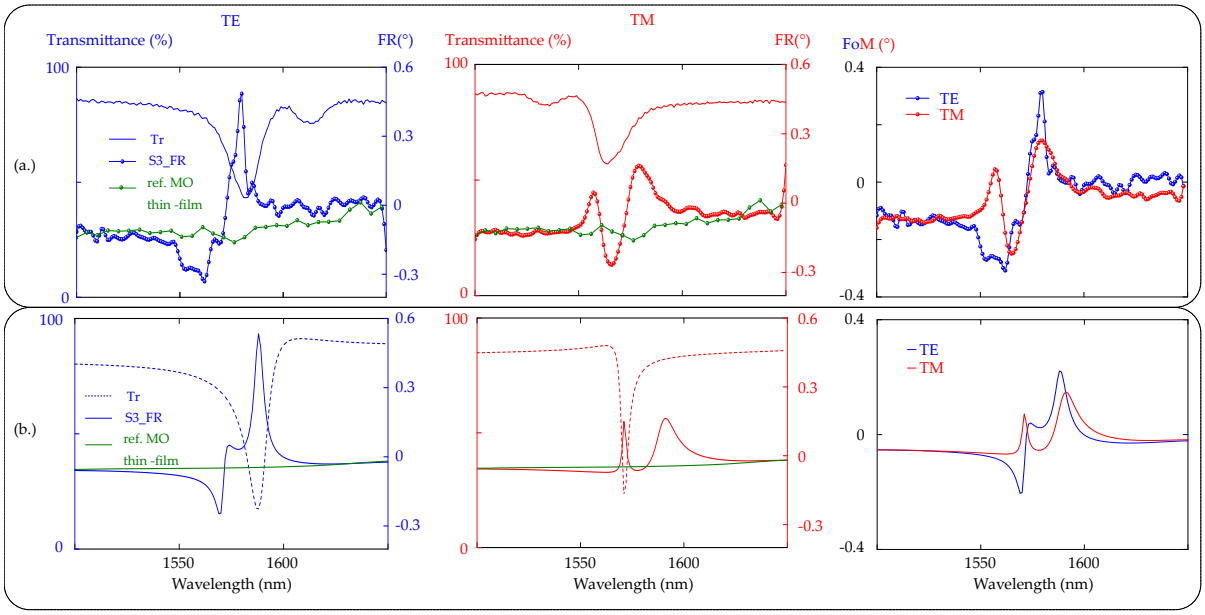

Figure 3.21: Sample S3 at 0° incidence. Measured (a.) and simulated (b.) transmittance, FR and FoM for TE and TM polarizations with a reference thin-film (h = 593 nm).

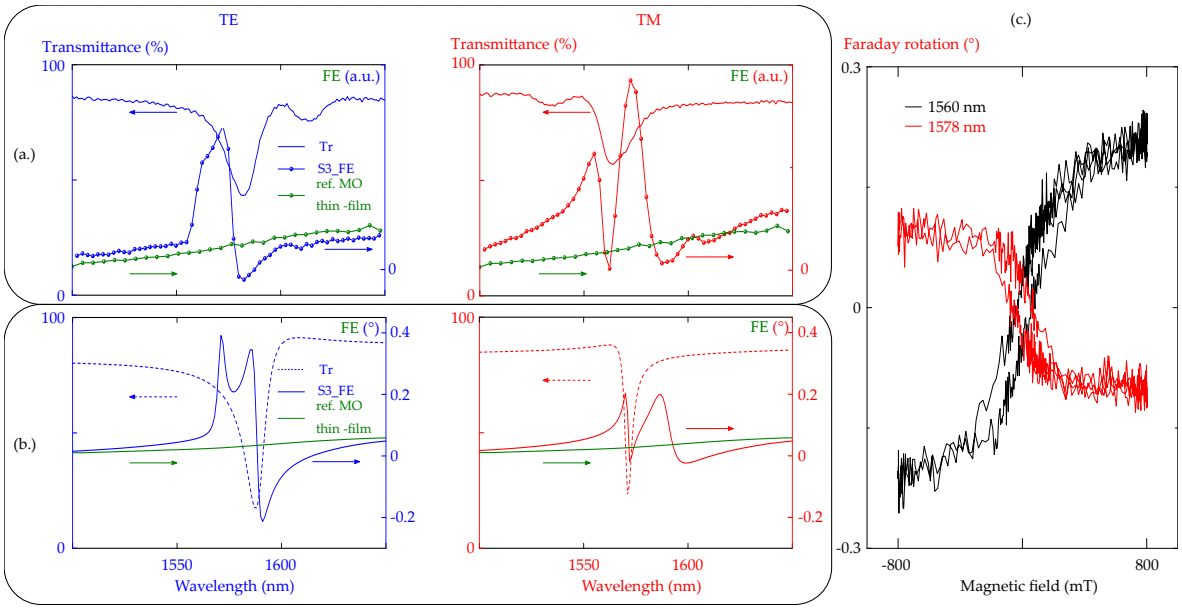

Figure 3.22: Sample S3 at 0° incidence. Measured (a.) and simulated (b.) transmittance and Faraday ellipticity for TE and TM polarizations with a reference thin-film (h = 593 nm). (c.) Sign inversion of FR hysteresis at 1560 nm and 1578 nm for TM polarization.

Concerning Faraday ellipticity, only a qualitative comparison is possible because the characterization bench is not calibrated for ellipticity measurements. Nevert-

heless, one can also notice the presence of an enhancement, and a good agreement between simulated and experimental data. It is to be noted that the difference of sign between the FR of reference thin-film for the optimized grating (refer figure 3.14) and the one realized (refer figure 3.21) is due to a difference in the applied magnetic field direction.

3.3.4 Kerr effect

Longitudinal Kerr effect had been measured and simulated in transmission, as the angle used is close to zero. Indeed, the parameters of the grating have been optimized to enhance the Faraday effect at 0° incidence. Due to geometry of the electromagnet, the magneto-optical bench described in the previous chapter and dedicated to Kerr effects (§ 2.4.2) permits to perform the L/PMOKE measurements in reflection only for large angles of incidence (higher than 25° for LMOKE). This is not suitable here as the resonance takes place around 0°. Nevertheless, it has been possible to perform LMOKE measurements in transmission for angles close to 0°, using the same bench. The PMOKE in transmission is equivalent to the Faraday effect. The experimental and simulated LMOKE data are reported in figure 3.23 for different incident angles. In this configuration also, an optical resonance produces a large enhancement of the MO effect with a peak whose magnitude and position depend on the angle of incidence. The maximum is 0.37° at 1565 nm for an incidence angle of 1.2°. Furthermore, the measurement of this effect had been carried out for different slit-widths of the monochromator. As presented in the previous chapter, a decrease of this width produces an increase of spectral resolution of the measurement. On one hand, thinner the slit, better is the spectral resolution and closer is the measured FR to what is expected from simulations. While on the other hand, the corresponding curves are much more noisy than the other two. Thus, a choice of slit-width of 3.45 mm is the best trade-off to perform the measurements.

Comparing experimental and simulated curves, one can see that the shapes are well respected, despite a spectral shift towards low wavelengths. Furthermore, the LMOKE resonances are wider for experimental curves and do not possess the same of kind of shoulders than what is expected from simulations.

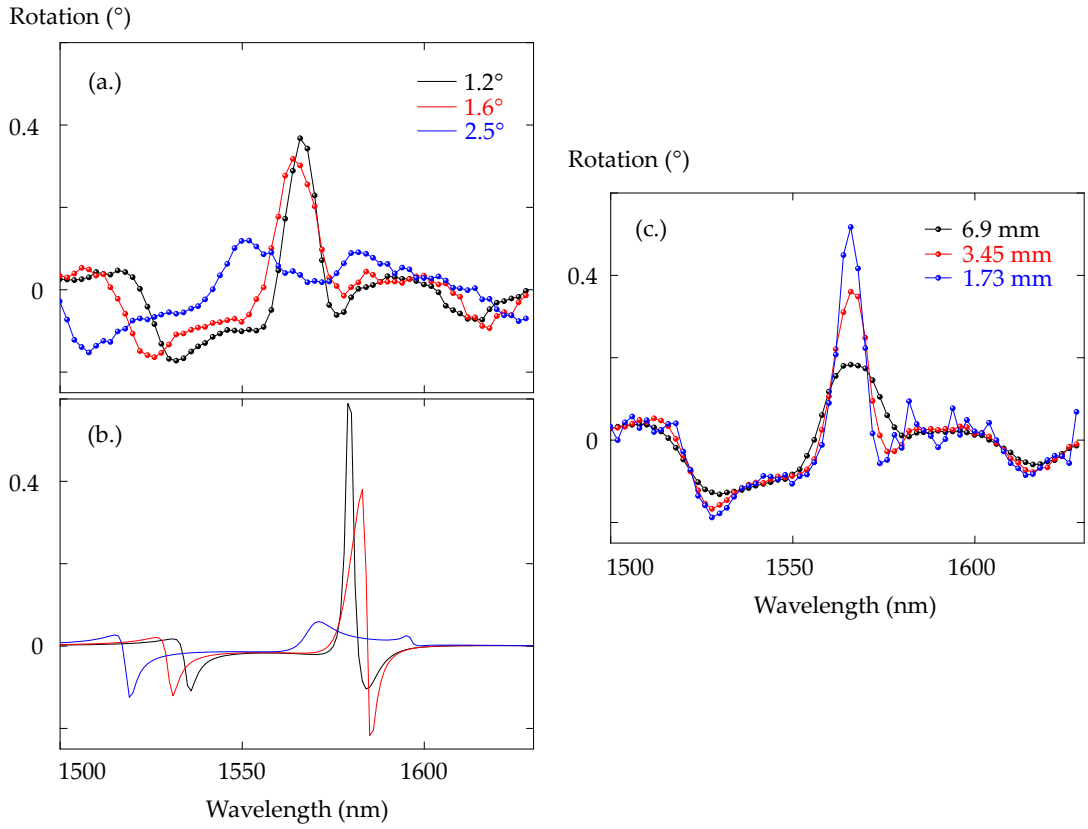

Figure 3.23: Longitudinal Kerr rotation in TM transmission. Measured (a.) and simulated (b.) Kerr rotation with variation of incidence angle for a monochromator slit-width of 3.45 mm. (c.) Measured Kerr rotation with variation of monochromator slit-width for $\theta_{inc} = 1.6°$.

This is due to the form of the optical resonances which are thinner in simulation (refer figure 3.20) and present specific behavior on their edges depending on the polarization, what is not so visible in experiments.

A TMOKE measurement had been carried out in reflection and transmission with an experimental electromagnet configuration which does not allow magnetic saturation of the MO composite. In fact, the applied magnetic field was limited to just 200 mT, as opposed to 800 mT for Faraday effect measurements. The principle of measurements did not allow an exact transmittance measurement of the sample with and without magnetic field, but only the intensity of output signal. Thus, the measurements reported in figure 3.24(a.) is not an absolute value of TMOKE. Nevertheless, an enhancement of the effect is demonstrated whether in transmission or in reflection, with a mutual coherence of the corresponding experimental and simulated curves. These shapes are directly linked to the shape of the optical reso-

nances. Evidently, TMOKE measured in transmission is larger than in reflection, as predicted by the simulation.

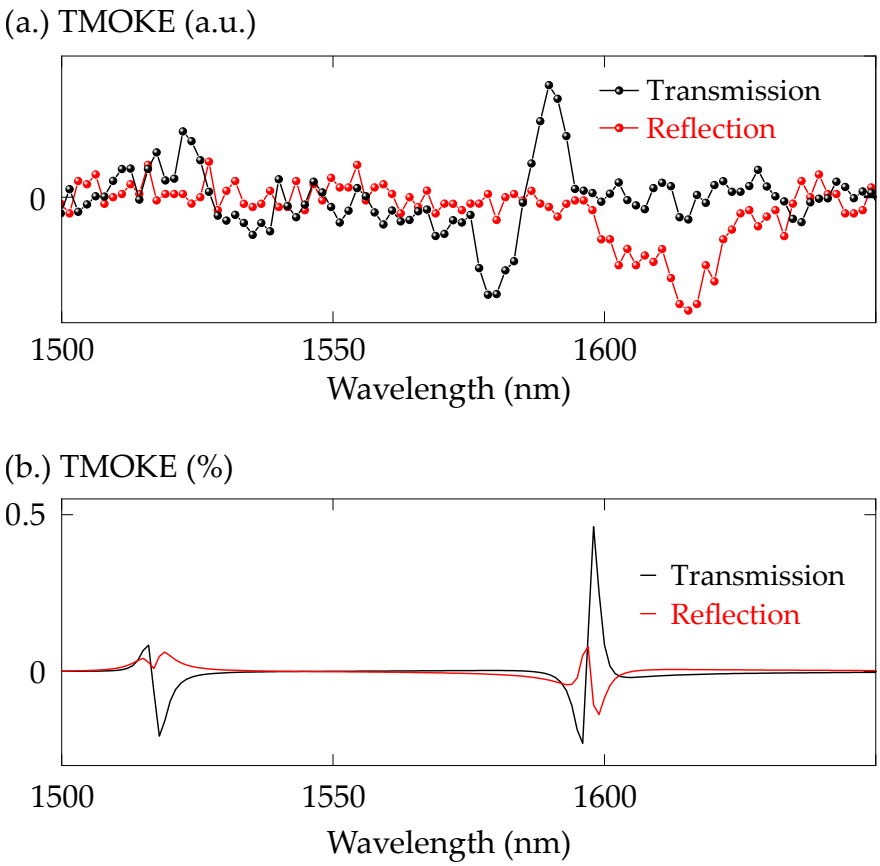

Figure 3.24: Experimental (a.) and simulated (b.) TMOKE for $\theta_{inc} = 2.6°$.

To conclude this experimental study of sample S3, enhancements of Faraday effect, LMOKE and TMOKE have been experimentally demonstrated. To the best of our knowledge, this is the first time that three different magneto-optical effects are shown to be enhanced using a single device. In addition, these results are obtained on a single all-dielectric grating, whereas works dedicated to such enhancement in the literature employ magneto-plasmonic devices. The results obtained in this work are based on the simultaneous excitation of TE and TM resonances through a proper choice of geometrical parameters of the dielectric grating. As a complement, the next section will illustrate that the MO enhancement is weaker when the TE/TM matching is worse.

3.3.5 Additional experiments

Samples S0 and S6, presented in table 3.5, had also been impregnated with the MO composite. In their cases, the volume fraction of NPs was fixed at 10% ($n = 1.547 + i0.005$). In figure 3.25 are reported the transmittances and FRs for both samples.

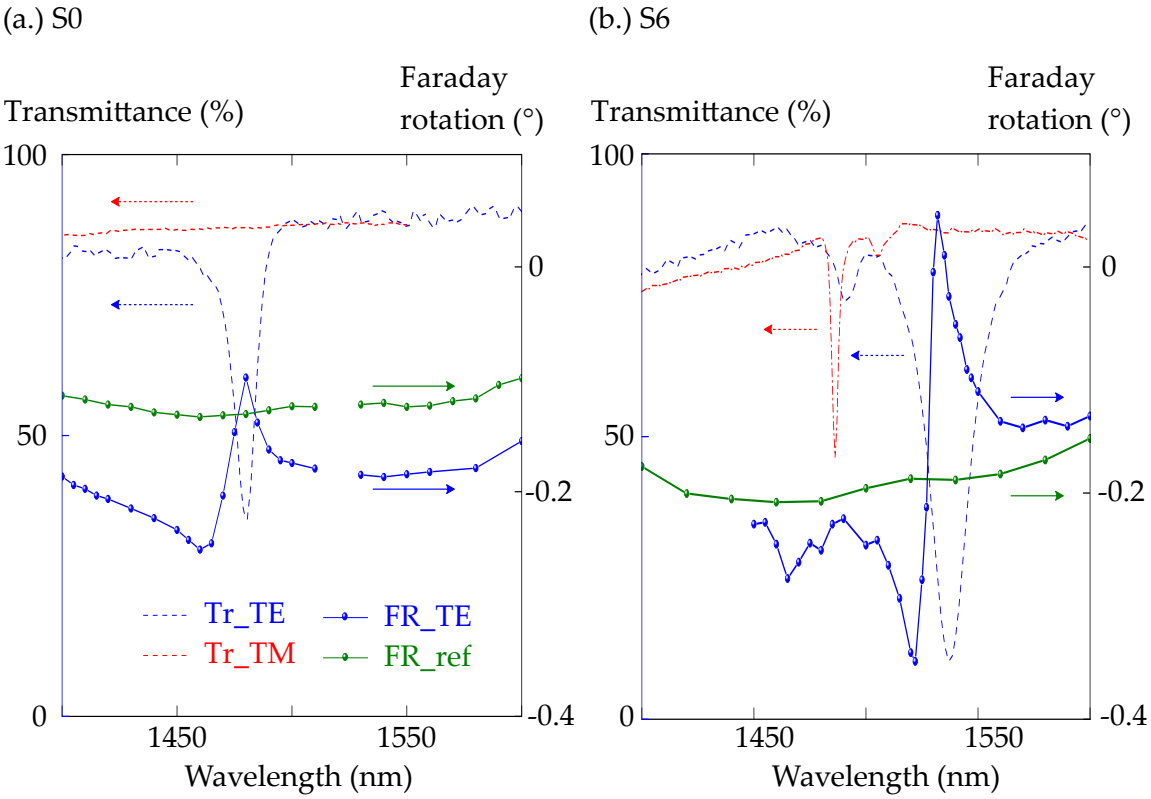

Figure 3.25: Transmittance (TE, TM) and FR (TE, reference) for samples S0 (a.) and S6 (b.).

No TM optical resonance had been evidenced for sample S0 whereas, TE resonance takes place at 1480 nm. The simulations performed on the S0 structure showed a very narrow TM resonance at 1430 nm. Our hypothesis is that the resolution of the spectrophotometer employed was too large to detect it. Nonetheless, one can still see a small spectral modification of the TE FR due to the poor matching and overlap between both TE and TM optical resonances.

Sample S6 exhibits an intermediate behavior between S0 and S3. Here, we can measure the TE and TM resonances, which are spaced 60 nm apart. The overlap is obviously better than in the S0 case, leading to an enhancement of the FR of approximately 1.5.

These experimental results confirm our design strategy which consists of maximizing the overlap between the TE and TM resonance to obtain an optimal FR enhancement.

Ellipsometry analysis of samples

In order to complete the analysis of the samples, supplementary measurements had been done by ellipsometry in transmission configuration at 0° incidence. Previous ellipsometry measurements presented in this manuscript were done classically in reflection mode on thin-films in order to determine their complex refractive index.

Ellipsometry spectra obtained in transmission configuration are reported in figure 3.26 for samples S3 and S0, in terms of ellipsometric parameters, Ψ and Δ. Ψ is related to the dichroism and, Δ to the phase-shift between both eigenstates (TE and TM). For both samples, the guided-mode resonant behavior manifests itself around 1500 nm as variations in Ψ and Δ. This modification in dichroism can be attributed to the difference in transmittance behavior of TE and TM light (see figure 3.22 or 3.25). Concerning the phase-shift parameter Δ, the physical origin of its behavior has not been attributed yet.

Another important feature can be pointed out in the ellipsometric spectra of S0 around 500 nm: a large variation of the ellipsometric parameters takes place. At the time, we do not have any clear explanation of this behavior which does not exist for S3. The only element is that a fine analysis of the TE and TM transmittance curves in this area shows that they go down to zero at 550 and 500 nm, respectively. Such annulations may explain the large dichroic variation. The magneto-optical spectrum had also been studied in this wavelength area. It is reported in figure 3.27 which evidences a large enhancement of the Faraday effect around 500 nm. But even if the rotation reaches 0.4°, one should be reminded that the transmittance is very low due to a large absorption produced by the NPs in this area (see figure 2.25). Thus, the Figure Of Merit is very low, whatever be the polarization.

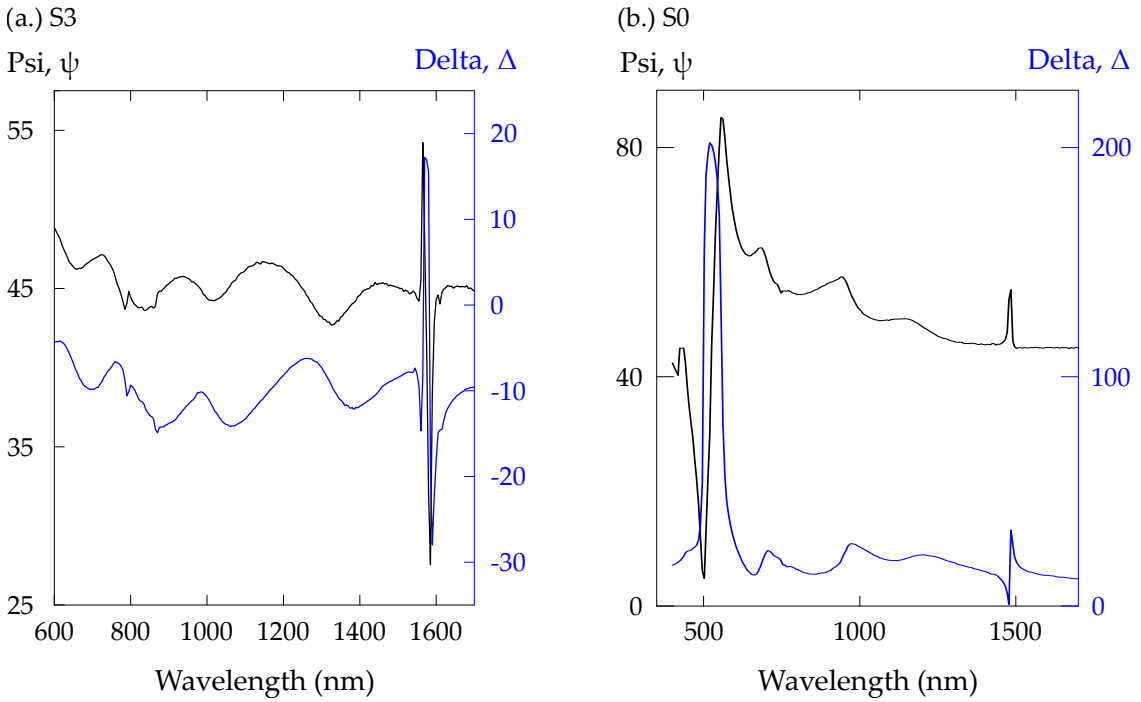

Figure 3.26: Measured values of ellipsometric parameters, Psi (Ψ) and Delta (Δ) for samples S3 (a.) and S0 (b.).

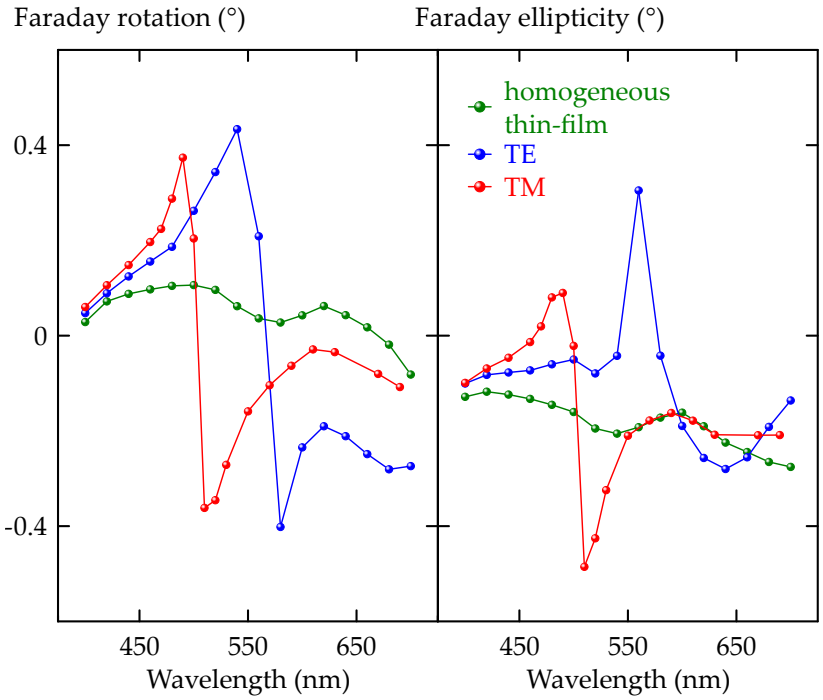

Figure 3.27: Experimentally measured FR and Faraday ellipticity for sample S0.

3.4 Conclusion

Using the methods described in chapter-2 and the design strategies resulting from the bibliographic analysis of the first chapter, the objectives of this chapter were to design, realize and analyze 1-D resonant gratings able to produce MO enhancement. Different routes had been followed in terms of materials and templates. Several results can be highlighted:

- The realization of 1-D magneto-plasmonic gratings with sinusoidal undulation of the metal is promising because such a device is easy to realize even on a large scale. Furthermore, it allows to work in transmittance through EOT, and a preliminary modification of the MO spectra has been evidenced. However, for improving this modification to an actual enhancement, the design has to be more precisely analyzed to take more benefits from the different dispersion behavior of plasmonic and dielectric modes, and even their hybridization.

- Resonant gratings made of a plain MO film with a dielectric grating on top of it are also very easy to realize. They produce TE and TM resonances with good efficiency, but these resonances cannot be matched. Despite this drawback, MO simulations have evidenced the possibility to enhance Faraday effect, but experimental demonstrations were limited by the low magnitude of these modifications. To improve them, among others, the thickness of the grating has to be increased to improve the resonant efficiencies.

- The use of 1-D silicon nitride gratings as a template to be impregnated by the composite produce an enhancement of several magneto-optical effects: Faraday, LMOKE and TMOKE. This enhancement, first demonstrated using numerical simulations, has been experimentally confirmed. Such a demonstration is, to the best of our knowledge, the first obtained with an all-dielectric device.

In all cases, studies of TMOKE enhancement were limited by the setup characteristics, which have to be improved in the future in order to allow such studies.

CONCLUSION AND FUTURE WORK

The aim of this thesis work was to design and realize resonant magneto-optical structures that can be made from a sol-gel material doped with magnetic nanoparticles. The advantages of the considered material are that it can be easily deposited on a wide range of substrates and can also impregnate pre- micro-structured gratings.

The bibliographic work, presented in chapter 1, permitted to identify the different type of structures leading to a MO effect enhancement and to understand the related underlying mechanisms. It showed that 1-D and 2-D magneto-plasmonic as well as 2-D and 3-D all-dielectric structures can lead to an enhancement of MO effects. It appeared that the condition to improve the rotation of polarization involved in Faraday effect, PMOKE and LMOKE is the coincidence of TE- and TM- optical resonances. This phase-matching condition has been theoretically demonstrated using plasmonic resonances in magneto-plasmonic structures or in 2-D crossed dielectric MO gratings. The TMOKE effect requires only a TM- resonance and has been demonstrated in magneto-plasmonic as well as all-dielectric structures.

To achieve our objectives, it had been decided to work on the design and on the realization of 1-D, all-dielectric and magneto-plasmonic resonant gratings. Fabrication of some structures, sol-gel synthesis, deposition as well as the spectral optical and magneto-optical characterizations were performed in our lab. The grating designs were performed using a commercial simulation software (MC Gratings) and the associated MO effects were computed using a homemade RCWA based code.

The main results concern a theoretical demonstration of an enhancement of the four first-order MO effects with a single 1-D resonant grating. This simulation study has been confirmed experimentally on a Si_3N_4 based MO composite material grating. Magneto-optical characterizations confirmed an enhancement of three MO effects: Faraday effect, LMOKE and TMOKE. This is, to the best of our knowledge, the first experimental demonstration of an enhancement of several MO effects with an all-dielectric structure. The magneto-plasmonic approach gave less obvious FR enhancement but presents the advantages of EOT. Moreover, the manufacturing steps of the different presented structures are relatively simple compared to those involved in the production of structures based on standard magnetic materials. This point makes possible to envisage a realization at reasonable cost, which would be compatible with sensor applications.

The demonstrated results of this thesis have highlighted the potential of our composite material for the realization of devices allowing the exaltation of different MO effects. Furthermore, the possibility of obtaining a simultaneous enhancement of different effects allows considering the realization of magnetic-field sensors able to detect at least two components of the field. The work done throughout this thesis enables us to discuss different perspectives:

- The design and fabrication steps of the magneto-plasmonic structure have to be optimized to improve the association of large transmittance and FR enhancement.

- To further simplify the fabrication of structures, a study on the possibility to employ a photopolymerizable sol-gel material doped with magnetic NP is a track that is already being explored as part of a joint thesis with Institut de Sciences des Matériaux de Mulhouse. The aim is to avoid the need of a grating template, which is essential today.

- The MO characterization setups have to be improved to measure the four first-order effects in transmission and reflection, and for a large range of incidence. The realization of a suitable electromagnet is in progress.

- Once such a setup is available, the realization of a TMOKE dedicated structure, i.e. optimized for this effect should be led. Such structure would allow larger TMOKE values than that obtained in this work. TMOKE being an

intensity effect and not a polarization rotation effect, its use in a sensor is more convenient.

BIBLIOGRAPHY

[1] AK Zvezdin and VA Kotov. *Modern magnetooptics and magnetooptical materials*. CRC Press, 1997.

[2] D Regatos, David Fariña, A Calle, Alfonso Cebollada, Borja Sepúlveda, G Armelles, and Laura M Lechuga. Au/Fe/Au multilayer transducers for magneto-optic surface plasmon resonance sensing. *Journal of Applied Physics*, 108(5):054502, 2010.

[3] Yuya Shoji, Tetsuya Mizumoto, Hideki Yokoi, I-Wei Hsieh, and Richard M Osgood Jr. Magneto-optical isolator with silicon waveguides fabricated by direct bonding. *Applied physics letters*, 92(7):071117, 2008.

[4] William E Ross, Demetri Psaltis, and Robert H Anderson. Two-dimensional magneto-optic spatial light modulator for signal processing. *Optical Engineering*, 22(4):224485–224485, 1983.

[5] E Betzig, JK Trautman, R Wolfe, EM Gyorgy, PL Finn, MH Kryder, and C-H Chang. Near-field magneto-optics and high density data storage. *Applied Physics Letters*, 61(2):142–144, 1992.

[6] Alexander B Khanikaev, Alexander V Baryshev, Andrey A Fedyanin, Alexander B Granovsky, and Mitsuteru Inoue. Anomalous faraday effect of a system

with extraordinary optical transmittance. *Optics Express*, 15(11):6612–6622, 2007.

[7] Mehmet C Onbasli, Lukáš Beran, Martin Zahradník, Miroslav Kučera, Roman Antoš, Jan Mistrík, Gerald F Dionne, Martin Veis, and Caroline A Ross. Optical and magneto-optical behavior of Cerium Yttrium iron garnet thin films at wavelengths of 200–1770 nm. *Scientific reports*, 6, 2016.

[8] Ivan S Maksymov, Jessica Hutomo, and Mikhail Kostylev. Transverse magneto-optical kerr effect in subwavelength dielectric gratings. *Optics express*, 22(7):8720–8725, 2014.

[9] Chengxin Lei, Sihao Wang, Zhixiong Tang, Daoyong Li, Leyi Chen, Shaolong Tang, and Youwei Du. Extraordinary optical transmission and enhanced magneto-optical effects induced by hybrid waveguide-surface plasmon polariton mode in bilayer metallic grating. *Journal of Physics D: Applied Physics*, 50(12):125002, 2017.

[10] VI Belotelov, LL Doskolovich, VA Kotov, EA Bezus, DA Bykov, and AK Zvezdin. Magnetooptical effects in the metal-dielectric gratings. *Optics communications*, 278(1):104–109, 2007.

[11] B Caballero, A García-Martín, and JC Cuevas. Faraday effect in hybrid magneto-plasmonic photonic crystals. *Optics express*, 23(17):22238–22249, 2015.

[12] VI Belotelov, IA Akimov, M Pohl, VA Kotov, S Kasture, AS Vengurlekar, Achanta Venu Gopal, DR Yakovlev, AK Zvezdin, and M Bayer. Enhanced magneto-optical effects in magnetoplasmonic crystals. *Nature Nanotechnology*, 6(6):370–376, 2011.

[13] Hadi Amata, Francois Royer, Fadi Choueikani, Damien Jamon, François Parsy, Jean-Emmanuel Broquin, Sophie Neveu, and Jean Jacques Rousseau. Hybrid magneto-optical mode converter made with a magnetic nanoparticles-doped SiO_2/ZrO_2 layer coated on an ion-exchanged glass waveguide. *Applied physics letters*, 99(25):251108, 2011.

[14] Renata Kekesi. *Experimental study of 3D magneto-photonic crystals made of silica inverse opals doped by magnetic nanoparticles.* PhD thesis, Saint Etienne, 2011.

[15] Masud Mansuripur. The faraday effect. *Optics and Photonics News*, 10:32–36, 1999.

[16] DK Misemer. The effect of spin-orbit interaction and exchange splitting on magneto-optic coefficients. *Journal of magnetism and magnetic materials*, 72(3):267–274, 1988.

[17] Koji Ando, Tokio Okoshi, and Naoki Koshizuka. Waveguide magneto-optic isolator fabricated by laser annealing. *Applied physics letters*, 53(1):4–6, 1988.

[18] Nicola A Spaldin. *Magnetic materials: fundamentals and applications.* Cambridge University Press, 2010.

[19] Jia-Ming Liu. *Photonic devices.* Cambridge University Press, 2009.

[20] PS Pershan. Magneto-optical effects. *Journal of applied physics*, 38(3):1482–1490, 1967.

[21] AK Zvezdin and VI Belotelov. Magnetooptical properties of two dimensional photonic crystals. *The European Physical Journal B-Condensed Matter and Complex Systems*, 37(4):479–487, 2004.

[22] Eugene Hecht and Alfred Zajac. Optics, ch. 8, 1998.

[23] Martin Pohl, LE Kreilkamp, Vladimir I Belotelov, Ilya A Akimov, NE Khokhlov, VJ Yallapragada, AV Gopal, M Nur-E-Alam, Mikhail Vasiliev, DR Yakovlev, et al. Tuning of the transverse magneto-optical kerr effect in magneto-plasmonic crystals. *New Journal of Physics*, 15(7):075024, 2013.

[24] JS Krasiński and GW Pearson. Optical nonreciprocal devices and their applications.

[25] Fabrice Donatini, Damien Jamon, J Monin, and Sophie Neveu. Experimental investigation of longitudinal magneto-optic effects in four ferrite ferrofluids in visible-near infrared spectrum. *IEEE transactions on magnetics*, 35(5):4311–4317, 1999.

[26] V Kirilyuk, A Kirilyuk, and Th Rasing. A combined nonlinear and linear magneto-optical microscopy. *Applied physics letters*, 70(17):2306–2308, 1997.

[27] Shinji Mino, Morito Matsuoka, Atsushi Shibukawa, and Ken'ichi Ono. Preparation of Bi iron garnet film with a two-step growth technique. *Japanese journal of applied physics*, 29(10A):L1823, 1990.

[28] Mehmet C Onbasli, Taichi Goto, Xueyin Sun, Nathalie Huynh, and CA Ross. Integration of bulk-quality thin film magneto-optical cerium-doped yttrium iron garnet on silicon nitride photonic substrates. *Optics express*, 22(21):25183–25192, 2014.

[29] DC Hutchings. Prospects for the implementation of magneto-optic elements in optoelectronic integrated circuits: a personal perspective. *Journal of Physics D: Applied Physics*, 36(18):2222, 2003.

[30] Robert Lux, Andreas Heinrich, Stephan Leitenmeier, Timo Körner, Michael Herbort, and Bernd Stritzker. Pulsed-laser deposition and growth studies of $Bi_3Fe_5O_{12}$ thin films. *Journal of applied physics*, 100(11):113511, 2006.

[31] T Wehlus, T Körner, S Leitenmeier, A Heinrich, and B Stritzker. Magneto-optical garnets for integrated optoelectronic devices. *Physica status solidi (a)*, 208(2):252–263, 2011.

[32] T Aichele, A Lorenz, R Hergt, and P Görnert. Garnet layers prepared by liquid phase epitaxy for microwave and magneto-optical applications–a review. *Crystal Research and Technology*, 38(7-8):575–587, 2003.

[33] Koji Ando, Naoki Koshizuka, Takashi Okuda, and Yuko Yokoyama. Growth-induced optical birefringence in LPE-grown Bi-based iron garnet films. *Japanese Journal of Applied Physics*, 22(10A):L618, 1983.

[34] Anne-Laure Joudrier, Maurice Couchaud, Hubert Moriceau, Jean-Emmanuel Broquin, Bernard Ferrand, and Jean-Luc Deschanvres. Direct bonding conditions of ferrite garnet layer on ion-exchanged glass waveguides. *physica status solidi (a)*, 205(10):2313–2316, 2008.

[35] Tetsuya Mizumoto and Yuya Shoji. Optical isolator with SOI waveguide. In *Optical Fiber Communication Conference and National Fiber Optic Engineers Conference*, page OWV3. Optical Society of America, 2009.

[36] Vadym Zayets, Mukul C Debnath, and Koji Ando. Optical isolation in $Cd_{1-x}Mn_xTe$ magneto-optical waveguide grown on GaAs substrate. *JOSA B*, 22(1):281–285, 2005.

[37] Magneto-optical mode conversion in $Cd_{1-x}Mn_xTe$ waveguide on GaAs substrate. *Applied Physics Letters*, 77(11):1593–1595, 2000.

[38] V Zayets, MC Debnath, and K Ando. Complete magneto-optical waveguide mode conversion in $Cd_{1-x}Mn_xTe$ waveguide on GaAs substrate. *Applied physics letters*, 84(4):565–567, 2004.

[39] Ml Freiser. A survey of magnetooptic effects. *IEEE Transactions on magnetics*, 4(2):152–161, 1968.

[40] Sadao Higuchi, Shunji Takekawa, Kenji Kitamura, et al. Magneto-optical properties of cerium-substituted yttrium iron garnet single crystals grown by traveling solvent floating zone method. *Japanese journal of applied physics*, 38(7R):4122, 1999.

[41] M Huang and Z-C Xu. Wavelength and temperature characteristics of BiY-bIG film/YIG crystal composite structure for magneto-optical applications. *Applied Physics A*, 81(1):193–196, 2005.

[42] TR Zaman, X Guo, and RJ Ram. Faraday rotation in an InP waveguide. *Applied physics letters*, 90(2):3514, 2007.

[43] Taichi Goto, Yu Eto, Keiichi Kobayashi, Yoji Haga, Mitsuteru Inoue, and CA Ross. Vacuum annealed Cerium-substituted Yttrium iron garnet films on non-garnet substrates for integrated optical circuits. *Journal of Applied Physics*, 113(17):17A939, 2013.

[44] Hyun-Suk Kim, Lei Bi, GF Dionne, and CA Ross. Magnetic and magneto-optical properties of Fe-doped $SrTiO_3$ films. *Applied Physics Letters*, 93(9):2506, 2008.

[45] Fadi Choueikani, François Royer, Damien Jamon, Ali Siblini, Jean Jacques Rousseau, Sophie Neveu, and Jamal Charara. Magneto-optical waveguides made of cobalt ferrite nanoparticles embedded in silica/zirconia organic-inorganic matrix. *Applied physics letters*, 94(5):051113, 2009.

[46] R Kekesi, F Royer, D Jamon, MF Blanc Mignon, E Abou-Diwan, JP Chatelon, S Neveu, and E Tombacz. 3D magneto-photonic crystal made with cobalt ferrite nanoparticles silica composite structured as inverse opal. *Optical Materials Express*, 3(7):935–947, 2013.

[47] Elie Abou Diwan, François Royer, Damien Jamon, Renata Kekesi, Sophie Neveu, Marie-Françoise Blanc-Mignon, and Jean Jacques Rousseau. Large spectral modification of the faraday effect of 3D $SiO_2/CoFe_2O_4$ magneto-photonic crystals. *Journal of Nanoscience and Nanotechnology*, 16(9):10160–10165, 2016.

[48] Fadi Choueikani. *Study of the potentiality of sol-gel thin layers doped by magnetic nanoparticles for the realization of integrated magneto-optic components*. PhD thesis, Université Jean Monnet de Saint Etienne, 2009.

[49] Sajeev John. Strong localization of photons in certain disordered dielectric superlattices. *Physical review letters*, 58(23):2486, 1987.

[50] Eli Yablonovitch. Inhibited spontaneous emission in solid-state physics and electronics. *Physical review letters*, 58(20):2059, 1987.

[51] Wenyi Cao, Antonio Muñoz, Peter Palffy-Muhoray, and Bahman Taheri. Lasing in a three-dimensional photonic crystal of the liquid crystal blue phase II. *Nature materials*, 1(2):111–113, 2002.

[52] Masahiro Imada, Susumu Noda, Alongkarn Chutinan, Takashi Tokuda, Michio Murata, and Goro Sasaki. Coherent two-dimensional lasing action in surface-emitting laser with triangular-lattice photonic crystal structure. *Applied physics letters*, 75(3):316–318, 1999.

[53] Rajesh V Nair and R Vijaya. Photonic crystal sensors: An overview. *Progress in Quantum Electronics*, 34(3):89–134, 2010.

[54] Hua Xu, Pin Wu, Chu Zhu, Abdelrahman Elbaz, and Zhong Ze Gu. Photonic crystal for gas sensing. *Journal of Materials Chemistry C*, 1(38):6087–6098, 2013.

[55] Susumu Noda and Masayuki Fujita. Light-emitting diodes: Photonic crystal efficiency boost. *Nature photonics*, 3(3):129–130, 2009.

[56] Christopher Wiesmann, Krister Bergenek, Norbert Linder, and Ulrich T Schwarz. Photonic crystal leds–designing light extraction. *Laser & Photonics Reviews*, 3(3):262–286, 2009.

[57] Yurii A Vlasov, Martin O'boyle, Hendrik F Hamann, and Sharee J McNab. Active control of slow light on a chip with photonic crystal waveguides. *Nature*, 438(7064):65–69, 2005.

[58] Toshihiko Baba. Slow light in photonic crystals. *Nature photonics*, 2(8):465–473, 2008.

[59] Shawn-yu Lin, JG Fleming, DL Hetherington, BK Smith, R Biswas, KM Ho, MM Sigalas, W Zubrzycki, SR Kurtz, and Jim Bur. A three-dimensional photonic crystal operating at infrared wavelengths. *Nature*, 394(6690):251–253, 1998.

[60] Peter Lodahl, A Floris Van Driel, Ivan S Nikolaev, Arie Irman, Karin Overgaag, Daniël Vanmaekelbergh, and Willem L Vos. Controlling the dynamics of spontaneous emission from quantum dots by photonic crystals. *Nature*, 430(7000):654–657, 2004.

[61] A Sharon, D Rosenblatt, and AA Friesem. Resonant grating–waveguide structures for visible and near-infrared radiation. *JOSA A*, 14(11):2985–2993, 1997.

[62] David Rosenblatt, Avner Sharon, and Asher A Friesem. Resonant grating waveguide structures. *IEEE Journal of Quantum electronics*, 33(11):2038–2059, 1997.

[63] MG Moharam and TK Gaylord. Rigorous coupled-wave analysis of planar-grating diffraction. *JOSA*, 71(7):811–818, 1981.

[64] Tapani Alasaarela, Dandan Zheng, Lingling Huang, Arri Priimagi, Benfeng Bai, Ari Tervonen, Seppo Honkanen, Markku Kuittinen, and Jari Turunen. Single-layer one-dimensional nonpolarizing guided-mode resonance filters under normal incidence. *Optics letters*, 36(13):2411–2413, 2011.

[65] Stefan Alexander Maier. *Plasmonics: fundamentals and applications*. Springer Science & Business Media, 2007.

[66] Thomas W Ebbesen, H J Lezec, HF Ghaemi, Tineke Thio, and PA Wolff. Extraordinary optical transmission through sub-wavelength hole arrays. *Nature*, 391(6668):667–669, 1998.

[67] JA Porto, FJ Garcia-Vidal, and JB Pendry. Transmission resonances on metallic gratings with very narrow slits. *Physical review letters*, 83(14):2845, 1999.

[68] Mitsuteru Inoue, Ken'ichi Arai, Toshitaka Fujii, and Masanori Abe. Magneto-optical properties of one-dimensional photonic crystals composed of magnetic and dielectric layers. *Journal of applied physics*, 83:6768–6770, 1998.

[69] Mitsuteru Inoue, Ken'ichi Arai, Toshitaka Fujii, and Masanori Abe. One-dimensional magnetophotonic crystals. *Journal of Applied Physics*, 85(8):5768–5770, 1999.

[70] M Inoue, R Fujikawa, A Baryshev, A Khanikaev, PB Lim, H Uchida, O Aktsipetrov, A Fedyanin, T Murzina, and A Granovsky. Magnetophotonic crystals. *Journal of Physics D: Applied Physics*, 39(8):R151, 2006.

[71] R Rosenberg, CB Rubinstein, and DR Herriott. Resonant optical Faraday rotator. *Applied Optics*, 3(9):1079–1083, 1964.

[72] Takuya Yoshimoto, Taichi Goto, Ryosuke Isogai, Yuichi Nakamura, Hiroyuki Takagi, CA Ross, and M Inoue. Magnetophotonic crystal with Cerium substituted Yttrium Iron Garnet and enhanced Faraday rotation angle. *Optics express*, 24(8):8746–8753, 2016.

[73] Yoji Haga, Taichi Goto, Baryshev AV, and Mitsuteru Inoue. One-dimensional single-and dual-cavity magnetophotonic crystal fabricated by bonding. *Journal of the Magnetics Society of Japan*, 36(1_2):54–57, 2012.

[74] Grishin AM and Khartsev SI. All-garnet magneto-optical photonic crystals. *Journal of the Magnetics Society of Japan*, 32(2_2):140–145, 2008.

[75] Rong Li and Miguel Levy. Bragg grating magnetic photonic crystal waveguides. *Applied Physics Letters*, 86(25):251102, 2005.

[76] Andrey A Fedyanin, Oleg A Aktsipetrov, Daisuke Kobayashi, Kazuhiro Nishimura, Hironaga Uchida, and Mitsuteru Inoue. Phase-matched magnetization-induced second-harmonic generation in Yttrium-Iron-Garnet magnetophotonic crystals. *IEEE transactions on magnetics*, 40(4):2850–2852, 2004.

[77] AA Fedyanin, OA Aktsipetrov, D Kobayashi, K Nishimura, H Uchida, and M Inoue. Enhanced faraday and nonlinear magneto-optical kerr effects in magnetophotonic crystals. *Journal of magnetism and magnetic materials*, 282:256–259, 2004.

[78] Lijuan Dong, Haitao Jiang, Hong Chen, and Yunlong Shi. Enhancement of faraday rotation effect in heterostructures with magneto-optical metals. *Journal of Applied Physics*, 107(9):093101, 2010.

[79] Mikhail Vasiliev, Kamal E Alameh, Vladimir I Belotelov, Vyacheslav A Kotov, and Anatoly K Zvezdin. Magnetic photonic crystals: 1D optimization and applications for the integrated optics devices. *Journal of lightwave technology*, 24(5):2156, 2006.

[80] John D Joannopoulos, Steven G Johnson, Joshua N Winn, and Robert D Meade. *Photonic crystals: molding the flow of light*. Princeton university press, 2011.

[81] Zongfu Yu, Zheng Wang, and Shanhui Fan. One-way total reflection with one-dimensional magneto-optical photonic crystals. *Applied physics letters*, 90(12):121133, 2007.

[82] Kejie Fang, Zongfu Yu, Victor Liu, and Shanhui Fan. Ultracompact nonreciprocal optical isolator based on guided resonance in a magneto-optical photonic crystal slab. *Optics letters*, 36(21):4254–4256, 2011.

[83] Wai Lam Chan, Hou-Tong Chen, Antoinette J Taylor, Igal Brener, Michael J Cich, and Daniel M Mittleman. A spatial light modulator for terahertz beams. *Applied Physics Letters*, 94(21):213511, 2009.

[84] Nina Skivesen, Amølie Têtu, Martin Kristensen, Jørgen Kjems, Lars H Frandsen, and Peter I Borel. Photonic-crystal waveguide biosensor. *Optics Express*, 15(6):3169–3176, 2007.

[85] VI Belotelov, LL Doskolovich, and AK Zvezdin. Extraordinary magneto-optical effects and transmission through metal-dielectric plasmonic systems. *Physical review letters*, 98(7):077401, 2007.

[86] Victor Dmitriev, Fernando Paixão, and Marcelo Kawakatsu. Enhancement of faraday and kerr rotations in three-layer heterostructure with extraordinary optical transmission effect. *Optics letters*, 38(7):1052–1054, 2013.

[87] Daoyong Li, Chengxin Lei, Leyi Chen, Zhixiong Tang, Shaoyin Zhang, Shaolong Tang, and Youwei Du. Waveguide plasmon resonance induced enhancement of the magneto-optics in a Ag/Bi:YIG bilayer structure. *JOSA B*, 32(9):2003–2008, 2015.

[88] AV Baryshev, H Uchida, and M Inoue. Peculiarities of plasmon-modified magneto-optical response of gold–garnet structures. *JOSA B*, 30(9):2371–2376, 2013.

[89] AV Baryshev and AM Merzlikin. Tunable plasmonic thin magneto-optical wave plate. *JOSA B*, 33(7):1399–1405, 2016.

[90] Benfeng Bai, Jani Tervo, and Jari Turunen. Polarization conversion in resonant magneto-optic gratings. *New Journal of Physics*, 8(9):205, 2006.

[91] Jessie Yao Chin, Tobias Steinle, Thomas Wehlus, Daniel Dregely, Thomas Weiss, Vladimir I Belotelov, Bernd Stritzker, and Harald Giessen. Nonreciprocal plasmonics enables giant enhancement of thin-film faraday rotation. *Nature communications*, 4:1599, 2013.

[92] Lars E Kreilkamp, Vladimir I Belotelov, Jessie Yao Chin, Stefanie Neutzner, Daniel Dregely, Thomas Wehlus, Ilya A Akimov, Manfred Bayer, Bernd Stritzker, and Harald Giessen. Waveguide-plasmon polaritons enhance transverse magneto-optical kerr effect. *Physical Review X*, 3(4):041019, 2013.

[93] Dominik Floess, Jessie Y Chin, Akihito Kawatani, Daniel Dregely, Hanns-Ulrich Habermeier, Thomas Weiss, and Harald Giessen. Tunable and switchable polarization rotation with non-reciprocal plasmonic thin films at designated wavelengths. *Light: Science & Applications*, 4(5):e284, 2015.

[94] Hugues Marinchio, Rémi Carminati, Antonio García-Martín, and JJ Sáenz. Magneto-optical kerr effect in resonant subwavelength nanowire gratings. *New Journal of Physics*, 16(1):015007, 2014.

[95] AV Chetvertukhin, AA Grunin, AV Baryshev, TV Dolgova, H Uchida, M Inoue, and AA Fedyanin. Magneto-optical kerr effect enhancement at the Wood's anomaly in magnetoplasmonic crystals. *Journal of Magnetism and Magnetic Materials*, 324(21):3516–3518, 2012.

[96] AG Zhdanov, Andrey A Fedyanin, AV Baryshev, AB Khanikaev, Hiornaga Uchida, M Inoue, et al. Wood's anomaly in two-dimensional plasmon-assisted magnetophotonic crystals.

[97] AN Kalish and VI Belotelov. Magneto-optical effects for detection of in-plane magnetization in plasmonic crystals. *Physics of the Solid State*, 58(8):1563–1572, 2016.

[98] VV Kruglyak, SO Demokritov, and D Grundler. Magnonics. *Journal of Physics D: Applied Physics*, 43(26):264001, 2010.

[99] AA Serga, AV Chumak, and B Hillebrands. YIG magnonics. *Journal of Physics D: Applied Physics*, 43(26):264002, 2010.

[100] Nikita Kostylev, Ivan S Maksymov, Adekunle O Adeyeye, Sergey Samarin, Mikhail Kostylev, and Jim F Williams. Plasmon-assisted high reflectivity and strong magneto-optical kerr effect in permalloy gratings. *Applied Physics Letters*, 102(12):121907, 2013.

[101] Lukáš Halagačka, Mathias Vanwolleghem, Kamil Postava, Beatrice Dagens, and Jaromír Pištora. Coupled mode enhanced giant magnetoplasmonics transverse kerr effect. *Optics express*, 21(19):21741–21755, 2013.

[102] Olga Borovkova, Andrey Kalish, and Vladimir Belotelov. Transverse magneto-optical kerr effect in active magneto-plasmonic structures. *arXiv preprint arXiv:1609.07883*, 2016.

[103] Daria O Ignatyeva, Grigory A Knyazev, Pavel O Kapralov, Giovanni Dietler, Sergey K Sekatskii, and Vladimir I Belotelov. Magneto-optical plasmonic heterostructure with ultranarrow resonance for sensing applications. *Scientific Reports*, 6, 2016.

[104] Jorge F Torrado, Juan B González-Díaz, María U González, Antonio García-Martín, and Gaspar Armelles. Magneto-optical effects in interacting localized and propagating surface plasmon modes. *Optics express*, 18(15):15635–15642, 2010.

[105] JF Torrado, E Th Papaioannou, G Ctistis, P Patoka, M Giersig, G Armelles, and A Garcia-Martin. Plasmon induced modification of the transverse magneto-optical response in Fe antidot arrays. *physica status solidi (RRL)-Rapid Research Letters*, 4(10):271–273, 2010.

[106] Ivan S Maksymov. Magneto-plasmonics and resonant interaction of light with dynamic magnetisation in metallic and all-magneto-dielectric nanostructures. *Nanomaterials*, 5(2):577–613, 2015.

[107] VI Belotelov, LE Kreilkamp, IA Akimov, AN Kalish, DA Bykov, S Kasture, VJ Yallapragada, Achanta Venu Gopal, Alexander M Grishin, Sergiy I Khartsev, et al. Plasmon-mediated magneto-optical transparency. *Nature communications*, 4, 2013.

[108] N. Lyndin. MC grating software, 1999.

[109] WH Bragg. The structure of magnetite and the spinels. *Nature*, 95:561, 1915.

[110] William Henry Bragg. XXX. The structure of the spinel group of crystals. *The London, Edinburgh, and Dublin Philosophical Magazine and Journal of Science*, 30(176):305–315, 1915.

[111] Shôji Nishikawa. Structure of some crystals of spinel group. *Tokyo Sugaku-Buturigakkwai Kizi Dai 2 Ki*, 8(7):199–209_1, 1915.

[112] AS Vaingankar, BV Khasbardar, and RN Patil. X-ray spectroscopic study of cobalt ferrite. *Journal of Physics F: Metal Physics*, 10(7):1615, 1980.

[113] Fuchun Zhang, Shusuke Kantake, Yoshitaka Kitamoto, and Masanori Abe. Spin-spray ferrite-plated co ferrite films with high coercivity for perpendicular magnetic recording media. *IEEE transactions on magnetics*, 35(5):2751–2753, 1999.

[114] M Kooti and M Afshari. Magnetic cobalt ferrite nanoparticles as an efficient catalyst for oxidation of alkenes. *Scientia Iranica*, 19(6):1991–1995, 2012.

[115] Dong-Hyun Kim, David E Nikles, Duane T Johnson, and Christopher S Brazel. Heat generation of aqueously dispersed $CoFe_2O_4$ nanoparticles as heating agents for magnetically activated drug delivery and hyperthermia. *Journal of Magnetism and Magnetic Materials*, 320(19):2390–2396, 2008.

[116] J Smit and HPJ Wijn. Ferrites philips technical library. *Eindhoven, The Netherlands*, 278, 1959.

[117] William Fuller Brown Jr. Thermal fluctuations of a single-domain particle. *Physical Review*, 130(5):1677, 1963.

[118] M Kläui, CAF Vaz, H Kronmüller, and SSP Parkin. Handbook of magnetism and advanced magnetic materials. 2007.

[119] Nandiguim Lamai. *Study of magnetic and spectral behavior of Faraday effect in metallic oxides doped with magnetic nanoparticles of cobalt ferrite*. PhD thesis, Université Jean Monnet de Saint Etienne, 2016.

[120] WFJ Fontijn, PJ Van der Zaag, LF Feiner, Ruud Metselaar, and MAC Devillers. A consistent interpretation of the magneto-optical spectra of spinel type ferrites. *Journal of Applied Physics*, 85(8):5100–5105, 1999.

[121] I Torres-Díaz and C Rinaldi. Recent progress in ferrofluids research: novel applications of magnetically controllable and tunable fluids. *Soft matter*, 10(43):8584–8602, 2014.

[122] C Jeffrey Brinker and George W Scherer. *Sol-gel science: the physics and chemistry of sol-gel processing*. Academic press, 2013.

[123] Dominic S Peterson. Sol–gel technique. In *Encyclopedia of Microfluidics and Nanofluidics*, pages 1870–1874. Springer, 2008.

[124] H Henning Winter and Francois Chambon. Analysis of linear viscoelasticity of a crosslinking polymer at the gel point. *Journal of rheology*, 30(2):367–382, 1986.

[125] LE Scriven. Physics and applications of dip coating and spin coating. *MRS Online Proceedings Library Archive*, 121, 1988.

[126] JC Maxwell Garnett. Colours in metal glasses, in metallic films, and in metallic solutions. ii. *Philosophical Transactions of the Royal Society of London. Series A, Containing Papers of a Mathematical or Physical Character*, pages 237–288, 1906.

[127] J Zak, ER Moog, C Liu, and SD Bader. Magneto-optics of multilayers with arbitrary magnetization directions. *Physical Review B*, 43(8):6423, 1991.

[128] J Chandezon, G Raoult, and D Maystre. A new theoretical method for diffraction gratings and its numerical application. *Journal of Optics*, 11(4):235, 1980.

[129] J Chandezon, MT Dupuis, G Cornet, and D Maystre. Multicoated gratings: a differential formalism applicable in the entire optical region. *JOSA*, 72(7):839–846, 1982.

[130] Lifeng Li. Multilayer-coated diffraction gratings: differential method of Chandezon et al. revisited. *JOSA A*, 11(11):2816–2828, 1994.

[131] Lifeng Li, G Granet, JP Plumey, and J Chandezon. Some topics in extending the C-method to multilayer gratings of different profiles. *Pure and Applied Optics: Journal of the European Optical Society Part A*, 5(2):141, 1996.

[132] Lifeng Li. Reformulation of the fourier modal method for surface-relief gratings made with anisotropic materials. *Journal of Modern Optics*, 45(7):1313–1334, 1998.

[133] Evgeni Popov and Michel Nevière. Grating theory: new equations in fourier space leading to fast converging results for tm polarization. *JOSA A*, 17(10):1773–1784, 2000.

[134] Lifeng Li. Fourier modal method for crossed anisotropic gratings with arbitrary permittivity and permeability tensors. *Journal of Optics A: Pure and Applied Optics*, 5(4):345, 2003.

[135] Evgeny Popov and Michel Nevière. Maxwell equations in fourier space: fast-converging formulation for diffraction by arbitrary shaped, periodic, anisotropic media. *JOSA A*, 18(11):2886–2894, 2001.

[136] Hua Xu and Byoung Seung Ham. Investigation of extraordinary optical transmission and faraday effect in one-dimensional metallic-magnetic gratings. *Optics express*, 16(26):21375–21382, 2008.

[137] Y Jourlin, S Tonchev, AV Tishchenko, C Pedri, C Veillas, O Parriaux, A Last, and Y Lacroute. Spatially and polarization resolved plasmon mediated transmission through continuous metal films. *Optics express*, 17(14):12155–12166, 2009.

[138] Dominik Floess, Mario Hentschel, Thomas Weiss, Hanns-Ulrich Habermeier, Jian Jiao, Sergei G Tikhodeev, and Harald Giessen. Plasmonic analog of electromagnetically induced absorption leads to giant thin film faraday rotation of 14°. *Physical Review X*, 7(2):021048, 2017.

[139] Bobin Varghese, E Gamet, Damien Jamon, Sophie Neveu, Loic Berthod, Olga Shavdina, Stephanie Reynaud, Isabelle Verrier, Colette Veillas, and Francois Royer. Nano-composite magnetic material embedded on tio 2 pillars to realize magneto-optical resonant guided mode gratings. In *Integrated Optics: Devices, Materials, and Technologies XX*, volume 9750, page 97500X. International Society for Optics and Photonics, 2016.

LIST OF FIGURES

LIST OF TABLES

GLOSSARY

EOT Extra-ordinary Optical transmission. 34, 51, 137, 140

FP Fabry Perot. 51, 161

FR Faraday rotation. 12, 15, 16, 21–23, 27, 35–45, 52, 89, 91–94, 99, 100, 106, 108–113, 119, 120, 122, 123, 127, 129–131, 134–136, 140, 158–160, 163–167

FWHM Full-Width Half Maximum. 104

LCP Left-Circularly Polarized. 14

LMOKE Longitudinal Magneto-Optical Kerr Effect. 6, 17, 47, 48, 161

MO Magneto-Optical. 5, 9, 39, 40, 48–52, 102, 127, 161

NPs nanoparticles. 57

PMOKE Polar Magneto-Optical Kerr Effect. 17, 45

RCP Right-Circularly Polarized. 14

RCWA Rigorous Coupled Wave Analysis. 58

SPPs Surface Plasmon Polaritons. 50, 51, 161

TE Transverse Electric. 17, 33, 43, 44, 48, 159

TM Transverse Magnetic. 17, 33, 43, 44, 159

TMOKE Transverse Magneto-Optical Kerr Effect. 6, 17, 49–52, 161

Summary

Magneto-optical (MO) devices are the basic elements of optical isolators essential for lasers and LIDAR, and are also employed for aircraft imaging, data storage or sensing. A periodic structuration of the core magnetic material is a way to enhance its MO behavior, and is thus useful to reduce the footprint of integrated devices or to improve the sensitivity of related sensors. However, the processing of efficient magnetic materials on photonic platforms is still challenging, because classical MO materials require an annealing temperature as high as 700°C.

Using a sol-gel process, a silica matrix can be doped by magnetic nanoparticles ($CoFe_2O_4$) to produce a MO material which possesses a full compatibility with photonic substrates. In this work, this composite material was incorporated into an already structured template through a single step deposition at low temperature. The template was a 1-D Si_3N_4 grating on glass. Numerical simulations, based on RCWA methods, have been carried out to identify the suitable values of the grating period and the line-space ratio which produce a guided-mode resonance at 1.55 μm simultaneously for TE and TM polarizations, at normal incidence. MO simulations demonstrated that an enhancement of magneto-optical effects is obtained in transmission or reflection for every orientation of the applied magnetic field (Kerr or Faraday effects). The theoretical figures of merit for these structures were comparable or higher than those, reported in literature, which use classical MO materials. These enhancements were confirmed by experimental realizations and measurements. For instance, a Faraday rotation enhancement of 3.5 times was demonstrated compared to the reference thin-film. The corresponding figure of merit was comparable or higher than those reported in literature proving the high efficiency of our structure. The results of this work are the 1st demonstration of an enhancement of every MO effect with a single device.

Résumé

Les dispositifs magnéto-optiques (MO) sont les éléments de base des isolateurs optiques, éléments essentiels pour les lasers et LIDAR. Ils sont également utilisés pour l'imagerie, le stockage ou les capteurs. Une structuration périodique du matériau magnétique est un moyen pour en améliorer les performances, et ainsi réduire la taille des composants intégrés ou améliorer la sensibilité des capteurs associés. Cependant, la mise en œuvre des matériaux magnéto-optiques habituels au sein des plateformes d'optique intégrée est rendue difficile par la forte température de cristallisation (700°C) qu'ils requièrent.

En utilisant un processus sol-gel basse température, une matrice de silice peut être dopée par des nanoparticules magnétiques ($CoFe_2O_4$) pour produire un matériau qui présente une excellente compatibilité avec les substrats photoniques. Dans ce travail, ce matériau composite a été utilisé pour imprégner un réseau grâce à un dépôt en une seule étape à une température inférieure à 100°C. Il s'agit d'un réseau1D Si_3N_4 sur verre. Des simulations numériques, basées sur les méthodes RCWA, et réalisées à 1,55 μm ont permis de déterminer les paramètres adéquats pour obtenir un réseau résonnant, simultanément pour les polarisations TE et TM, à incidence normale. Les simulations MO ont démontré que ce type de structure permet d'obtenir l'exaltation de tous les effets magnéto-optiques classiques (Kerr et Faraday). Le facteur de mérite théorique obtenu est comparable voir supérieur à ceux rapportés dans la littérature qui utilisent des matériaux MO classiques. Ces améliorations ont été confirmées par des réalisations et caractérisations expérimentales. Par exemple, une augmentation de la rotation de Faraday d'un facteur 3,5 a été obtenue par rapport à un film mince de référence. Le facteur de mérite correspondant était comparable voir supérieur à ceux présentés dans la littérature prouvant la grande efficacité de notre structure. Les résultats de ce travail sont la première démonstration d'une augmentation de tous les effets MO avec un seul dispositif.